The control mechanisms on precipitation over northern Africa during a dust outbreak

Irene Reinares Martinez

Irene Reinares Martinez. The control mechanisms on precipitation over northern Africa during a dust outbreak. Climatology. Université Paul Sabatier - Toulouse III, 2017. English. NNT : 2017TOU30382 . tel-02016584

HAL Id: tel-02016584
https://theses.hal.science/tel-02016584v1

Submitted on 12 Feb 2019

Université Fédérale
Toulouse Midi-Pyrénées

THÈSE

En vue de l'obtention du

DOCTORAT DE L'UNIVERSITÉ DE TOULOUSE

Délivré par :

Université Toulouse 3 Paul Sabatier (UT3 Paul Sabatier)

Présentée et soutenue par :
Irene REINARES MARTÍNEZ
le mardi 21 novembre 2017

Titre :

Les mécanismes de contrôle des précipitations dans le nord de l'Afrique pendant un épisode poussiéreux.

École doctorale et discipline ou spécialité :
ED SDU2E : Océan, Atmosphère, Climat

Unité de recherche :
Laboratoire d'Aérologie (Université Toulouse - CNRS)

Directeur/trice(s) de Thèse :

Jean-Pierre CHABOUREAU

Jury :
Frank ROUX - LA, France - Président du Jury
Andreas FINK - KIT, Allemagne - Rapporteur
Cyrille FLAMANT - LATMOS, France - Rapporteur
Luiz MACHADO - CPTEC-INP, Brésil - Rapporteur
Catherine RIO - CNRM, France - Examinatrice
Jean-Pierre CHABOUREAU - LA, France - Directeur de thèse

The Control Mechanisms on Precipitation over Northern Africa During a Dust Outbreak

---

Author:

Irene REINARES MARTÍNEZ

Supervisor:

Jean-Pierre CHABOUREAU

Remerciements

Je tiens à remercier mon directeur de thèse, Jean-Pierre Chaboureau, qui m'a donné l'opportunité de réaliser cette thèse. Merci pour ta disponibilité et ta réactivité, ainsi que pour m'avoir sensibilisée à toute la rigueur requise dans la production scientifique.

Je remercie Frank Roux pour avoir accepté d'être le président du jury. Merci aux rapporteurs (Cyrille Flamant, Andreas Fink et Luiz Machado) et à l'examinatrice (Catherine Rio) de ma thèse pour le temps consacré à la lecture du manuscrit, vos conseils et vos déplacements pour assister à la soutenance. Merci également aux membres du comité de thèse (Catherine Rio et Romain Roehrig) pour les discussions intéressantes qui ont fait avancer mon travail scientifique.

Un merci à l'ensemble des collègues du laboratoire pour leur aide, les échanges, l'accueil agréable et la bonne humeur. Vous avez créé des bonnes conditions de travail. Dans ce contexte, j'ai beaucoup appris sur la recherche comme voie professionnelle.

Si, bien sûr, le travail derrière un ordinateur reste très confortable, j'ai énormément apprécié les trois semaines passées à Savé lors de la campagne de terrain de DACCIWA. Je remercie Jean-Pierre Chaboureau pour avoir accepté que j'y prenne part. Ce fut une aventure très intense et absolument géniale, qui m'a transmis le goût de la science expérimentale. Une pensée pour l'équipe du LA présente à Savé (Marie Lothon, Claire Delon, Corinne Jambert, Omar Gabella, Cheikh Dione). Merci à Pierre Durand pour tes explications patientes et passionnées, et a Fabienne Lohou pour l'organisation de la campagne à Savé et pour m'avoir donné l'opportunité d'y participer.

Une des meilleures choses de la thèse, est, comme toujours, l'aspect humain. Un merci chaleureux aux collègues avec qui j'ai eu l'opportunité de passer des très bons moments en dehors du laboratoire. Vous êtes devenus des pollègues = potes + collègues.

Finalement, merci à tous mes pollègues, mes amis et ma famille qui ont compris que, vers la fin, la thèse n'était pas si facile. Vous m'avez encouragée et accompagnée. À ceux qui étaient à côté de moi et à ceux qui étaient ailleurs en France, en Espagne, en Allemagne, et encore plus loin.

Abstract

Precipitation in northern Africa occurs mainly during the monsoon season. It arises from the interaction of atmospheric processes across a wide range of scales, making its prediction challenging. The control mechanisms on precipitation are examined during a well-documented case study of dust emission and transport on 9-14 June 2006. The same method for cloud detection and tracking was applied on satellite observations and several numerical simulations (with explicit or parameterized convection) to investigate the precipitating systems. Among the various types of systems identified, mesoscale convective systems (MCSs) yield most of the total precipitation, with an observed contribution of 66%. The greatest precipitation producers are the long-lived MCSs (i.e., that last more than 6 h), at the origin of 55% of precipitation. These MCSs become more organized, i.e., larger, longer-lived and faster, as they propagate westward. The convection-permitting simulations capture the rainfall partition, but do not fully reproduce the organization of the long-lived MCSs. The simulation with parameterized convection fails to correctly represent the rain partition. This shows the added-value provided by the convection-permitting simulations. The radiative effect of dust is then analyzed, by comparing two convection-permitting simulations, with and without dust-radiation interaction. The direct effects are a mid-level warming and a near-surface cooling mainly in the western parts of northern Africa, which tend to stabilize the lower atmosphere. One semi-direct effect is a decrease in precipitation. This rainfall drop is explained by a too low number of long-lived MCSs which, nevertheless, are longer-lived and more efficient in terms of precipitation production. The diminution in the number of long-lived MCSs is due to the stabilization of the atmosphere inhibiting the triggering of convection.

Résumé

Les précipitations en Afrique septentrionale se produisent principalement pendant la saison des moussons. Elles résultent de l'interaction des processus atmosphériques dans une large gamme d'échelles, ce qui rend leur prévision difficile. Les mécanismes de contrôle des précipitations sont examinés au cours d'un épisode bien documentée d'émission et de transport de poussières du 9 au 14 juin 2006. La même méthode pour la détection et le suivi des nuages a été appliquée sur les observations par satellite et plusieurs simulations numériques (avec convection explicite ou paramétrée) pour étudier les systèmes précipitants. Parmi les différents types de systèmes identifiés, les systèmes convectifs de mésoéchelle (MCS) produisent la majeure partie de la précipitation totale, avec une contribution observée de 66%. Les plus grands producteurs de précipitation sont les MCS à longue durée de vie (c'est-à-dire de plus de 6 h), à l'origine de 55% des précipitations. Ces MCS deviennent plus organisés, c'est-à-dire plus grands, plus longs et plus rapides, alors qu'ils propagent vers l'ouest. Les simulations permettant la convection reproduisent la partition de pluie, mais ne reproduisent pas complètement l'organisation des MCS à longue durée de vie. La simulation avec convection paramétrée ne parvient pas à représenter correctement la partition de pluie. Cela montre la valeur ajoutée apportée par les simulations permettant la convection. L'effet radiatif des poussières est ensuite analysé en comparant deux simulations permettant la convection, avec et sans interaction poussière-rayonnement. Les effets directs sont un réchauffement de niveau moyen et un refroidissement à proximité de la surface, principalement dans les parties occidentales de l'Afrique septentrionale, qui tendent à stabiliser l'atmosphère inférieure. Un effet semi-direct est une diminution des précipitations. Cette baisse des pluies s'explique par un nombre trop faible de MCS à longue durée de vie qui,

néanmoins, ont une durée de vie plus longue et sont plus efficaces en termes de production de précipitations. La diminution du nombre de MCS à longue durée de vie est due à la stabilisation de l'atmosphère qui inhibe le déclenchement de la convection.

Table of Contents

Introduction

Precipitation in northern Africa mainly lies on a zonal band centered around 10°N during the boreal summer. This seasonal rainfall arrives with the monsoon and represents the majority of the annual precipitation, up to 70% (CLIVAR, 2015). It presents a marked diurnal variability driven by solar heating. The maximum in precipitation tends to occur in the late afternoon or evening, when many convective systems develop. Most of the precipitation arises from isolated convective systems, such as congestus or cumulonimbus clouds, or from organized mesoscale convective systems (MCSs).

MCSs are large cloud systems that lay over several hundreds of kilometers and consist of both convective and extended stratiform precipitating regions. They can last several days and propagate westward over long distances. MCSs are the prime contributors to precipitation. For example, they bring up to 90% of the precipitation in the Sahel (Mathon et al., 2002). Because of their long lifetime, they also participate to much of the nighttime rainfall (Zhang et al., 2016). Their characteristics and organization are modulated by the large-scale environment, like the African Easterly Jet (AEJ), which controls the low- to mid-level wind shear. Such an environment favors the maintain of MCSs, or the African Easterly Waves with which MCSs tend to propagate.

Global Climate Models (GCMs) with $\sim$100 km grid spacings with parameterized convection struggle to capture realistically the diurnal cycle of precipitation in the tropics, often introducing biases in both the amplitude and phase. For instance, the diurnal cycle simulated over northern Africa by Collier and Bowman (2004) shows an amplitude 84% times larger and the peak was advanced by 3 to 4 hours. In general, convection parameterizations have issues to represent the distribution of precipitation intensities, the diurnal cycle of precipitation, the structure of convective systems and their interaction with larger-scale atmospheric weather systems (e.g., Holloway et al., 2012; Marsham et al., 2013).

Convection-permitting models (CPMs) allow nowadays to perform simulations with convection being explicitly represented over continental-scale domains. They are run at kilometric resolutions resolving a wide range of scales. On the one hand, this is of high importance to capture the interaction of MCSs with synoptic circulations in northern Africa, such as the AEJ or the monsoon flow. On the other hand, the convection-permitting resolution allows to represent the individual updrafts and downdrafts within MCSs as well as the associated cold pools. Due to their finer resolution, convection-permitting simulations provide a more accurate representation of the surface and orography with respect to GCMs. This is advantageous as both the small-scale variability associated to surface processes and the orography act forcing convection.

Dust is another important feature of the northern African weather. Emitted mostly in spring and the beginning of summer, dust can affect the atmosphere in two ways. It interacts with radiation (direct radiative effect of dust), creating local warming or cooling of the air as a response to the absorbing and scattering properties of dust. This can, in turn, induce changes on clouds and precipitation (semi-direct effects). It interacts with clouds too, acting as a precursor for ice crystal formation and modifying the cloud microphysics (indirect effect).

The radiative effect of dust on precipitation is a subject of debate. Disparities arise in the simulated response of rainfall with respect to dust effect over northern Africa. Some GCMs predict an increase in precipitation, others a decrease (e.g., Yoshioka et al., 2007; Lau et al., 2009; Bangalath and Stenchikov, 2015). Both reliable observations to constrain the dust variability in models and an insight on the effect of dust on the atmospheric processes at finer resolutions are fundamental to understand the discrepancies in global tendencies. Indeed, the direct radiative effect of dust and its semi-direct effect on precipitation remains highly unexplored at convective-permitting resolutions.

This thesis is based on the case study of 9-14 June 2006 (Flamant et al., 2009) that occurred during the field campaign of the AMMA (Analyses Multidisciplinaires de la Mousson Africaine) project (Redelsperger et al., 2006). The period chosen was outstanding in terms of dust loads over northern Africa. Dust was emitted in remote eastern sources and then transported westward, where MCSs were observed to propagate. The aim of this work is to analyze the mechanisms that drive precipitation during the selected case study. Special attention is given to the processes leading to the organization of highly precipitating MCSs. Among them, the radiative impact of dust on the African weather and MCS organization is addressed.

To achieve these objectives, several simulations were performed with the Méso-NH model (Lafore et al., 1998) over a large domain covering northern Africa. The model was run at convection-permitting resolution and with parameterized convection. In the first case, the convective circulation can be resolved in more detail. For instance, updrafts of length scale of 1 to 10 km within large convective systems are explicitly resolved. Another simulation to analyze the sensitivity to the dust radiative effect was carried out at convection-permitting resolution. The simulations were evaluated against satellite and ground-based observations.

The manuscript is organized as follows. In chapter 1 an overview of the north African monsoon system is given, with a description of its atmospheric circulations. The processes of moist convection giving rise to precipitation are described, and the properties of MCSs, prime contributors to precipitation during the monsoon season, are detailed. The dust distribution and life cycle is described, as well as its effects on the atmosphere.

In chapter 2 the case study of 9-14 June 2006, object of this thesis, is described. The atmospheric research model Méso-NH is presented as well as the set up for the simulations performed for the case study. An overview of the observational data sets that have been utilized to evaluate those simulations is given. Finally, the method developed in the framework of this thesis to track the MCSs is described.

In chapter 3 the organization of the mesoscale convective systems as they propagate westward in northern Africa, from Ethiopia to the Atlantic coast is studied. The sensitivity to the resolution and representation of the precipitating systems is examined, through the study of the distribution of precipitation and its diurnal cycle. The results are contained in the article *Precipitation and Mesoscale Convective Systems: Explicit versus Parameterized Convection over Northern Africa*, published in *Monthly Weather Review*.

In chapter 4 the radiative effect of dust on the atmosphere is investigated through the comparison of two convection-permitting simulations, one with dust-radiation interaction and the other without it. Particular attention is given to the consequences of considering the direct and semi-direct effect of dust on the organization of MCSs. The results are presented in the article *Precipitation and Mesoscale Convective Systems: Radiative Impact of Dust over Northern Africa*, published in *Monthly Weather Review*.

Lastly, the conclusion and some perspectives for future work are given.

Introduction (en français)

La précipitation en Afrique septentrionale réside principalement dans une bande zonale centrée autour de 10°N pendant l'été boréal. Cette précipitation saisonnière arrive avec la mousson et représente la majorité de la précipitation annuelle, jusqu'à 70% du total (CLIVAR, 2015). Elle présente une variabilité diurne marquée grâce au chauffage solaire. Le maximum de précipitation tend à se produire en fin d'après-midi ou en soirée, lorsque de nombreux systèmes convectifs se développent. La plupart des précipitations proviennent de systèmes convectifs isolés, comme les congustus ou les cumulonimbus, ou des systèmes convectifs de mésoéchelle (MCS, de l'anglais *Mesoscale Convective System*) organisés.

Les MCS sont des grands systèmes nuageux qui s'étendent sur plusieurs centaines de kilomètres et se composent à la fois de régions convectives et de régions précipitantes stratiformes étendues. Ils peuvent durer plusieurs jours et se propager vers l'ouest sur de longues distances. Les MCS sont les principaux contributeurs à la précipitation. Ils apportent ainsi jusqu'à 90% de la précipitation au Sahel (Mathon et al., 2002). du fait de leur longue durée de vie, ils participent également à une grande partie des précipitations nocturnes (Zhang et al., 2016). Leur caractéristique et leur organisation sont modulées par l'environnement de grande échelle, comme le jet d'est africain (AEJ, de l'anglais *African Easterly Jet*) en anglais) qui contrôle le cisaillement du vent des basses couches. Un tel environnement favorise le maintien des MCS ou les ondes d'est africaines avec lesquelles les MCS ont tendance à se propager.

Les modèles climatiques globaux (GCM, de l'anglais *Global Climate Model*) avec des espacements de grille de $\sim$100 km et une convection paramétrée présentent des difficultés pour reproduire de façon réaliste le cycle diurne des précipitations dans les tropiques, introduisant souvent des biais à la fois dans l'amplitude et la phase. Le cycle diurne simulé sur l'Afrique septentrionale par Collier and Bowman (2004) montre ainsi une amplitude en précipitation 84% fois plus grande que celle observée et un maximum en avance de 3 à 4 heures. En général, les paramétrisations de la convection ont des problèmes pour représenter la répartition des intensités de précipitation, le cycle diurne des précipitations, la structure des systèmes convectifs et leur interaction avec des systèmes météorologiques atmosphériques de grande échelle (p. ex., Holloway et al., 2012; Marsham et al., 2013).

Les modèles permettant la convection (CPM, de l'anglais *Convection-Permitting Model*)) permettent aujourd'hui d'effectuer des simulations avec une convection explicitement représentée sur des domaines à l'échelle continentale. Ils sont lancés à des résolutions kilométriques résolvant la dynamique atmosphérique sur une large gamme d'échelles. D'une part, il est très important de reproduire l'interaction des MCS avec les circulations synoptiques en Afrique septentrionale, comme l'AEJ ou le flux de la mousson. D'autre part, la résolution permettant la convection représente explicitement les courants ascendants et descendants dans les MCS ainsi que les poches froides associées. En raison de leur résolution plus fine, les simulations permettant la convection offrent aussi une représentation plus précise de la surface et de l'orographie par rapport aux GCM. Ceci est avantageux car la variabilité de petite échelle associée aux processus de surface et l'orographie agit pour forcer la convection.

Les poussières sont une autre caractéristique importante du climat de l'Afrique septentrionale. Émises principalement au printemps et au début de l'été, elles peuvent affecter l'atmosphère de deux façons. Elles interagissent avec le rayonnement (effet radiatif direct des poussières), créant un réchauffement local ou un refroidissement de l'air en réponse aux propriétés d'absorption et de diffusion des poussières. Cela peut, à son tour, induire des changements sur les nuages et les précipitations (effets semi-directs). Elles interagissent aussi avec les nuages, agissant comme des précurseurs pour la formation de cristaux de glace et en modifient la microphysique (effet indirect).

L'effet radiatif des poussières sur les précipitations fait l'objet d'un débat. Des disparités apparaissent dans la réponse simulée des précipitations par rapport à l'effet des poussières sur l'Afrique septentrionale. Certains GCM prédisent une augmentation des précipitations, d'autres une diminution (p. ex., Yoshioka et al., 2007; Lau et al., 2009; Bangalath and Stenchikov, 2015). Avoir à la fois des observations fiables pour contraindre la variabilité des poussières dans les modèles et une vision de l'effet des poussières sur les processus atmosphériques à des résolutions plus fines est fondamental pour comprendre les écarts dans les tendances globales. En effet, l'effet radiatif direct des poussières et son effet semi-direct sur les précipitations restent largement inexplorés aux résolutions permettant la convection.

Cette thèse est basée sur le cas d'étude du 9 au 14 juin 2006 (Flamant et al., 2009) qui s'est produit pendant la campagne de terrain du projet AMMA (Analyses multidisciplinaires de la Mousson Africaine, Redelsperger et al., 2006). La période choisie était remarquable en termes de poussières sur l'Afrique septentrionale. Les poussières ont été émises depuis des sources orientales éloignées, puis transportées vers l'ouest où la propagation des MCS a été observée. Le but de ce travail est d'analyser les mécanismes qui contrôlent aux précipitations pendant le cas d'étude sélectionné. Une attention particulière est accordée aux processus menant à l'organisation de MCS fortement précipitants. Parmi eux, l'impact radiatif des poussières sur l'atmosphère africaine et l'organisation des MCS sont abordés.

Pour atteindre ces objectifs, plusieurs simulations ont été réalisées avec le modèle Méso-NH (Lafore et al., 1998) sur un vaste domaine couvrant l'Afrique septentrionale. Le modèle a été lancé avec une résolution fine permettant la convection et une résolution grossière avec convection paramétrée. Dans le premier cas, la circulation convective peut être résolue avec plus de détails. Par exemple, les courants ascendants d'une échelle de longueur de 1 à 10 km dans de grands systèmes convectifs sont explicitement résolus. Une autre simulation pour analyser la sensibilité à l'effet radiatif des poussières a été effectuée avec la résolution permettant la convection. Toutes les simulations ont été évaluées par rapport à des observations obtenues par satellite et depuis le sol.

Le manuscrit est organisé comme suit. Dans le chapitre 1, un aperçu du système de mousson de l'Afrique septentrionale est donné, avec une description de ses circulations atmosphériques. Les processus de convection humide donnant lieu à des précipitations sont décrits, et les propriétés des MCS, principaux contributeurs aux précipitations pendant la saison de la mousson, sont détaillées. La distribution de la poussière et le cycle de vie sont décrits, ainsi que ses effets sur l'atmosphère.

Dans le chapitre 2, le cas d'étude du 9-14 juin 2006, objet de cette thèse, est décrit. Le modèle de recherche atmosphérique Méso-NH est présenté ainsi que la mise en place des simulations réalisées pour le cas d'étude. Un aperçu des ensembles de données d'observation qui ont été utilisés pour évaluer ces simulations est donné. Enfin, la méthode développée dans le cadre de cette thèse pour suivre les MCS est décrite.

Dans le chapitre 3, l'organisation des systèmes convectifs de mésoéchelle au fur et à mesure de leur propagation vers l'ouest en Afrique septentrionale, de l'Ethiopie à la côte atlantique, est étudiée. La sensibilité à la résolution et à la représentation des systèmes précipitants est examinée par l'étude de la distribution des précipitations et de leur cycle diurne. Les résultats sont contenus dans l'article *Precipitation and mesoscale convective systems for explicit versus parameterized convection over northern Africa*, publié au *Monthly Weather Review*.

Dans le chapitre 4, l'effet radiatif des poussières sur l'atmosphère est étudié par comparaison entre deux simulations CPM, l'une avec interaction entre poussières et rayonnement et l'autre sans. Une attention particulière est accordée aux conséquences des effets direct et semi-direct des poussières sur l'organisation des MCS. Les résultats sont présentés dans l'article *Precipitation and Mesoscale Convective Systems: Radiative Impact of Dust over Northern Africa*, publié au *Monthly Weather Review*.

Enfin, la conclusion et des perspectives pour des travaux futurs sont données.

Chapter 1

The North African Monsoon System

Contents

Monsoon traditionally refers to seasonal reversing winds accompanied by changes in precipitation, this seasonal variation of precipitation leads to both a rainy and a dry phase. Indeed, the word monsoon derives from the Arabic *mausim* which means season, and according to the glossary of the *American Meteorological Society*, the word was first applied to the winds over the Arabian Sea, which changed from northeasterly to southwesterly every six months. Then, the term was applied to other regions in the world (Fig. 1.1).

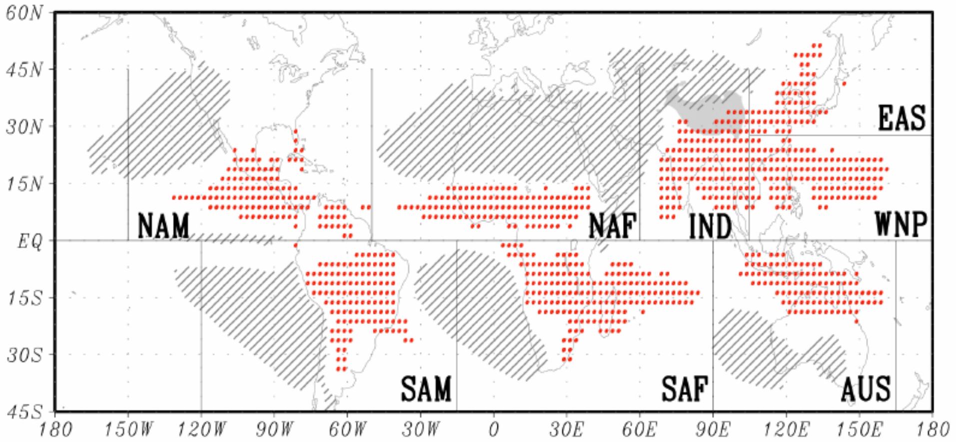

Figure 1.1: Main monsoon systems in the world: North American (NAM), South American (SAM), North African (NAF), South African (SAF), Indian (IND), East Asian (EAS), Western North Pacific (WNP), Australian (AUS). The monsoon domains are defined where the local difference in precipitation rate between boreal summer (May to September) and winter (November to March) exceeds 2.5 mm day^{-1}, and the local summer precipitation represents more than 55% of the annual. Hatched regions correspond to summer precipitation less than 1 mm day^{-1}. Based on rain gauge and satellite data for land and ocean, respectively. From World Climate Research Programme (WCRP).

In this chapter, the main atmospheric circulations at the continental scale during the north African monsoon season are described. An overview of the spatial and diurnal variability of precipitation are presented and the physical processes driving moist convection are explained. A description of the type of precipitating systems with a focus on mesoscale convective systems is given. The characteristics of dust emission and dust effects on the atmosphere, with a special interest on precipitation, are presented. Finally, the objectives of this thesis are detailed.

1.1 Large-scale Atmospheric Circulations

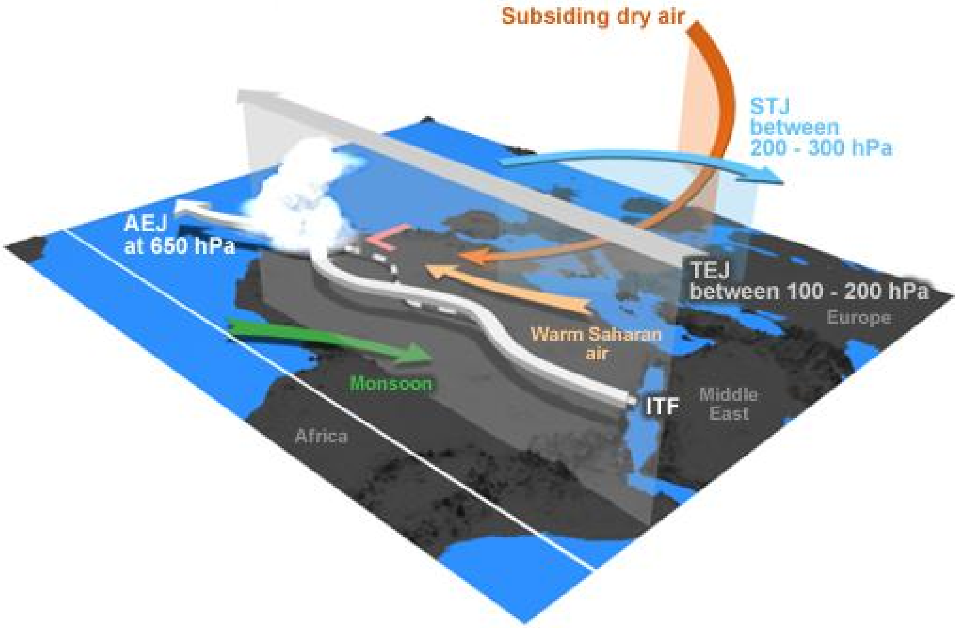

Figure 1.2: The key circulations conforming the North African Monsoon system: the low-level monsoon and warm Saharan flows (Harmattan) converge around the ITF/ITD (Intertropical Front/Discontinuity), the Heat Low (depicted by a L over the Sahara), the middle-level AEJ (African Easterly Jet) and AEWs (African Easterly Waves) and the high-level TEJ (Tropical Easterly Jet) and STJ (Subtropical Jet). Reproduced from the Comet program.

The North African Monsoon is a land-ocean-atmosphere coupled system that presents a wide range of spatial and temporal scales during boreal summer. The main large-scale atmospheric elements interacting over Africa are represented in Fig. 1.2.

During the monsoon season, the southern-hemisphere trade winds reverse and pass through the Equator from the ocean to the continent. A strong meridional surface temperature gradient between land and ocean is established. This is due to the increased solar forcing over the continent, that creates a low pressure region, often enhanced by a sea surface temperature (SST) decrease in the Equatorial Atlantic. The resulting southwesterly **monsoon flow** can reach 1 or 2-

km depth and transports moisture from the ocean to the dry continent, creating favorable conditions for convection there.

When the northern-hemisphere trade winds cross the Sahara towards the south, they take the name of **Harmattan flow**. The Harmattan wind is hot and dry. It can extend up to the 5-km altitude and transport dust loads from the desert. The convergence zone where both the monsoon and Harmattan flows encounter over the continent is called the **Intertropical Discontinuity** (ITD).

To the north of the ITD, the surface of the Sahara warms up during daytime due to intense solar heating. As the temperature of the surface increases, energy is transferred from the surface to the atmosphere in the form of outgoing longwave radiation and sensible heat flux by conduction. Almost no latent heat is released because the soil is very dry. The low levels of the atmosphere warm up there and the pressure diminishes considerably. This is the **Heat Low** region, where dry convection is very intense and helps mix the Saharan boundary layer, that can reach up to 5-km depth (Cuesta et al., 2009). The Heat Low region presents a cyclonic circulation.

The strong meridional temperature gradient over the Sahelian region, which is maximum at the surface and decreases with height, induces a variation of the zonal wind with altitude. This is the thermal wind equilibrium. As temperature increases from the south to the north of the continent, the zonal component of the wind increases with altitude, generating a strong vertical wind shear between the surface and the altitude where the meridional temperature gradient disappears. At that altitude, around 650 hPa, this zonal wind has become maximum with a mean speed of 15 m s^{-1} and located around 12°N in July. It is known as the **African Easterly Jet** (AEJ). It presents a diurnal variability.

To the northern and southern sides of the AEJ synoptic disturbances are observed over Central and West Africa, where the AEJ is the most intense. These perturbations are called **African Easterly Waves** (AEWs). They propagate westward at a mean speed of 8 m s^{-1} and with a wavelength of around 3000 km. They present a frequency of 3-5 days. Their initiation is associated with convection over the Darfur Plateau and the Ethiopian Highlands (Mekonnen et al., 2006).

The AEWs present perturbations both at 850 and 700 hPa, that consist on a single dynamic mode propagating westward simultaneously over the African continent (Pytharoulis and Thorncroft, 1999). AEWs have an amplitude maximum is near 700 hPa, close to the AEJ level, and a low-level vorticity maximum near 850 hPa. In general, the composite AEW has a northeast-southwest oriented axis, the trough (Reed et al., 1977). The trough region presents generally two cyclonic vortices at 850 hPa (Fink and Reiner, 2003). The maximum of 850 hPa vorticity, corresponding to the southern vortex, occurs near the 700 hPa center in the region of moist convection. The secondary peak of 850 hPa vorticity, the northern vortex, is associated with the ITD. Convergence (divergence) at 850 hPa occurs ahead (behind) of the trough. Inversely, divergence (convergence) at 700 and 200 hPa occurs ahead (behind) of the trough (Reed et al., 1977). The AEWs are the most intense near the altitude of the AEJ, to its southern flank. Energy transfers between the jet and the waves allow the growth of the latter. Also to the southern flank of the AEJ, the humidity transported by the monsoon flow over the continent is large, favoring the development of convective systems. The latter appear to propagate within the AEJ and to be modulated by the AEWs (Fig. 1.3). An AEW can be viewed as alterning northerly and southerly wind perturbations at 700 hPa, immersed in the strong zonal AEJ flow. The southerlies transport cooler and moister air whereas dry, hot and dust ladden air masses are transported by the northerlies. The northerlies and the trough regions of the AEW are found to be favorable for convection.

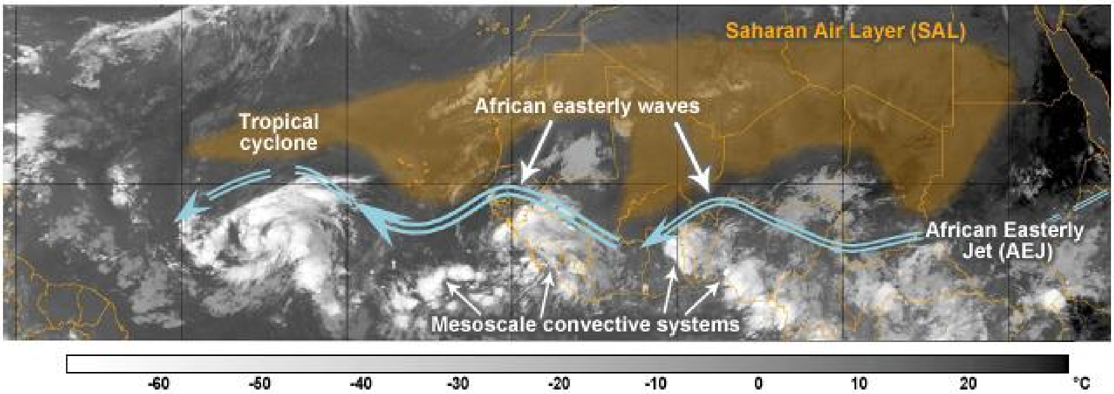

Figure 1.3: Most relevant synoptic and mesoscale systems of the northern African monsoon. Reproduced from the Comet program.

The intense divergence in the higher troposphere due to convection feeds the **Tropical Easterly Jet** (TEJ), located at 200 hPa around 10°N, and extending from the east of the Asian continent to the west coast of Africa.

1.2 Precipitation

1.2.1 Spatial Distribution

Precipitation over northern tropical Africa takes place mostly during the North African monsoon season. Since the development of the monsoon in May over the Guinean Coast, that reaches its maturity in August in the Sahel, to its retreat in October, the monsoon season concentrates more than 70% of the annual precipitation in West Africa (CLIVAR, 2015). Over Ethiopia, the precipitation during the summer contributes to between 50 and 95% of the annual totals (e.g., Segele and Lamb, 2005; Korecha and Barnston, 2007).

The average precipitation in the Earth for June 1998-2011 is presented in Fig. 1.4. Over Africa, most of the precipitation lies between the Equator and the Sahara, from Ethiopia to the Atlantic.

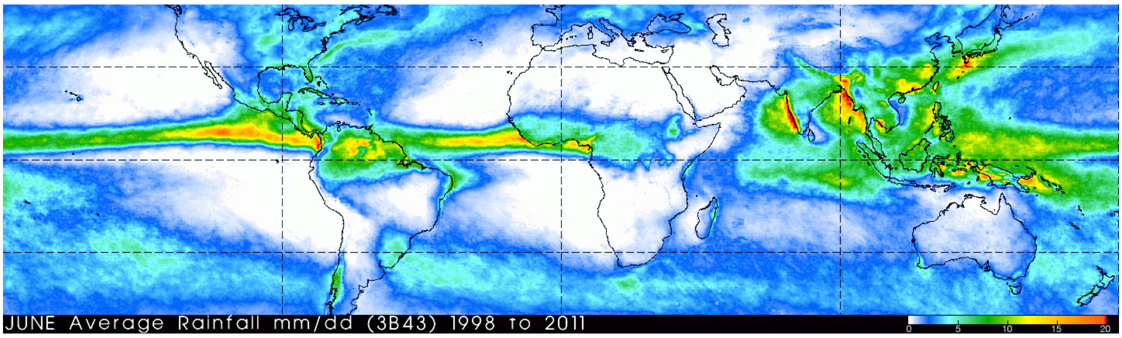

Figure 1.4: Mean rainfall for June 1998-2011, from product 3B43 of the Tropical Rainfall Measuring Mission (TRMM). Reproduced from https://pmm.nasa.gov/trmm/trmm-based-climatology.

The rain belt is colocated with the Intertropical Convergence Zone (ITCZ) over the northern tropical Africa. The beginning of the rainy season corresponds to the ITCZ migration from the Southern Hemisphere in winter to the Northern Hemisphere in summer. Its location is at around 5°N in May-June and 10°N in July-August (Sultan and Janicot, 2000). Sultan and Janicot (2003) established the 14 May as the mean climatological date for the monsoon preonset, when the first increase of precipitation in West Africa occurs. This is called the Guinean regime. Guinean coastal rainfall is mainly controlled by SST in the Atlantic ocean (Nguyen et al., 2011). The monsoon onset is set to the climatological value of 24 June (Sultan and Janicot, 2003). It corresponds to a sudden shift of the ITCZ from 5°N to 10°N and a second increase in precipitation. These dates are consistent with the 11 May and 26 June for the mean Guinean coastal rainfall onset and retrait, respectively, found by Nguyen et al. (2011). From infrared (IR) satellite imagery, the ITCZ manifests as a band of clouds, usually groups of thunderstorms moving westward within the AEJ. Coincident with the southern flank of the AEJ, the ITCZ presents a line of vorticity around the 850 hPa level, enhancing convergence and the development of convection.

AEWs have a major role on precipitation at intraseasonal scale. Maxima in precipitation is observed ahead of the AEW troughs, coincident with low-level convergence (Reed et al., 1977). Northward bursts of the monsoon every 3-5 days can lead to enhanced moisture available for convection (Couvreux et al., 2010) at the synoptic scale. For instance, a rainfall surplus over Algeria was observed to be associated with the northward penetrations of the monsoon flow forced by the south sector of AEWs (Cuesta et al., 2010).

1.2.2 Diurnal Cycle

During the daytime, the solar radiation warms up the Earth surface and oceans, which heat, in turn, the atmosphere through infrared radiation and conduction at the surface. The air masses close to the surface expand and become less dense than the air aloft, which leads to conditionnaly unstable conditions. When convection triggers, it redistributes the excess of energy to higher altitudes through vertical mass transport. In the early morning convection is shallow and in the absence of clouds it is called dry convection. Thermals mix the atmosphere in a layer of around 1-km depth, the atmospheric boundary layer. When water vapor condenses we speak of moist convection. In moist convection, the vapor condensation releases latent heat, resulting in extra warming of the air masses, that will pursue their uplift vertically and can give birth to precipitating clouds if other factors are met. For instance, the mechanical uplifting forced by orography, cold pool or gravity wave is usually required, or at least beneficial, for the formation of precipitating systems. The processes of moist convection will be addressed in section 1.2.3.

Precipitation over tropical Africa exhibits thus a marked diurnal cycle mainly driven by solar heating and yielding the generation of precipitating systems usually in the afternoon. Over eastern Africa, convection is triggered in the afternoon along the western slopes of the Ethiopian Highlands (e.g., Laing et al., 2008, 2012). Over West Africa, precipitation typically shows a single diurnal peak (Zhang et al., 2016). The time distribution of the peak of precipitation varies between land and ocean (Fig. 1.5). Over land, the maximum of precipitation tends to occur between the late afternoon and night, from 16 to 04 LT (local time). Afternoon peaks are generally associated with topographic features such as the Jos Plateau, Cameroon and Ennedi Mountains. Nocturnal peaks are due to precipitating systems downstream of orography, over Niamey and the northeastern part of Benin which is devoid of mountainous regions (e.g., Mathon et al., 2002; Fink et al., 2006; Janiga and Thorncroft, 2014; Zhang et al., 2016). Indeed, the average precipitation diurnal maxima result from the superposition of local maximum, coincident with the triggering of convection, and the delayed arrival of systems propagating from the east. The diurnal peak of oceanic precipitation is attained in night or early morning, between 04 and 10 LT (Fig. 1.5).

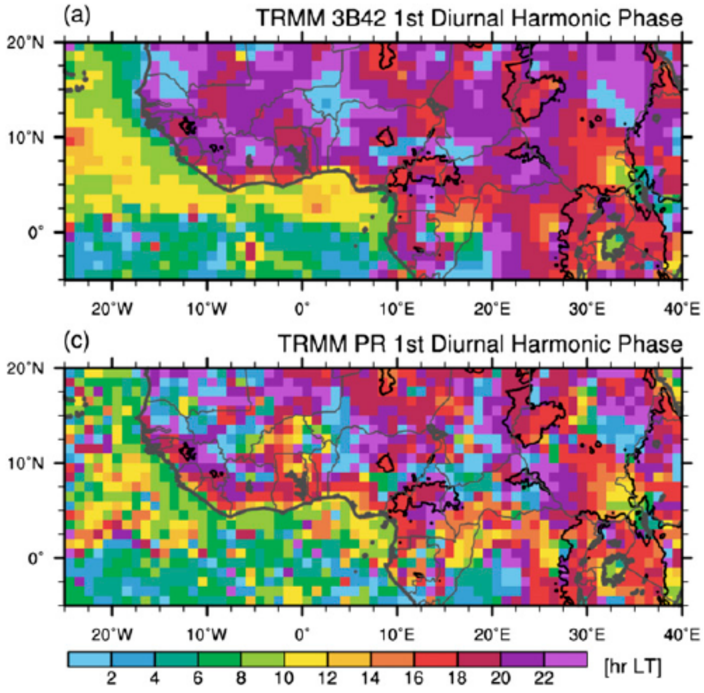

Figure 1.5: Time of the maximum in the diurnal cycle of precipitation for (a) TRMM product 3B42 and (c) TRMM PR (Precipitation Radar) July-September (JAS) 1998-2012. Reproduced from Janiga and Thorncroft (2014).

1.2.3 Precipitating Clouds

Precipitation mainly arises from **moist convective clouds**. Precipitating systems originate as individual convective cells triggered by the development of the boundary layer during daytime. Moist convection is a response to atmospheric instability, which is evaluated with respect to the vertical displacement of moist air parcels. Every air parcel is subject to buoyancy, a force resulting from the density difference between the air parcel and its environment. If a parcel is less dense than the ambient air, it experiences an upward acceleration, it is positive buoyant. If the parcel is denser, it suffers a downward acceleration, it is negatively buoyant. For moist convection to happen, the air parcel needs to ascend further up than the altitude where it becomes saturated. At this level, its water vapor condenses leading to the formation of the first hydrometeors, cloud droplets. A cloud then begins to form.

An emagram like in Fig. 1.6 is very convenient to determine the vertical extent of the cloud and to represent its convective development as an air parcel ascends in the atmosphere.

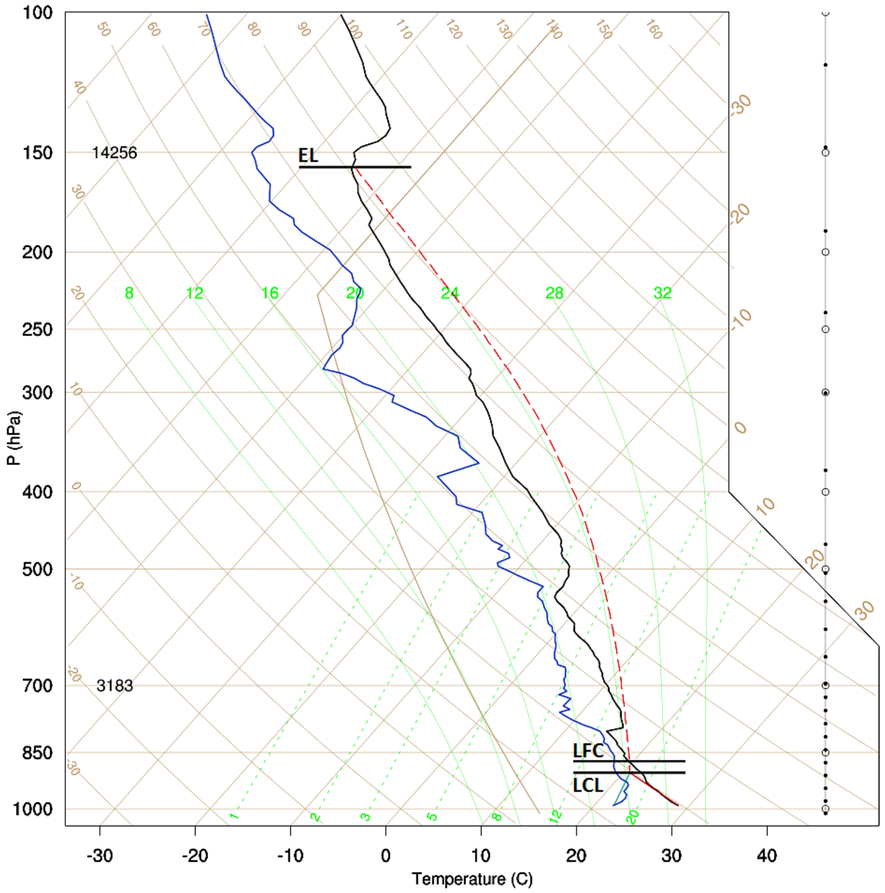

Figure 1.6: Sounding taken at Savé (Benin) at 1800 UTC on 1 July 2016, during the DACCIWA (Dynamics-Aerosols-Chemistry-Cloud Interactions in West Africa) field campaign. The temperature is represented by the black line and the dew point temperature by the dark blue line. The theoretical trajectory of an ascending parcel is indicated by red line. It follows a dry adiabat (solid) up to the LCL and a moist adiabat from the LCL until the EL. The area between the sounding profile and the parcel trajectory below (above) the LFC corresponds to the CIN (CAPE).

When a parcel ascends from the ground, it conserves its potential temperature as long as it is unsaturated, following a dry adiabat. Because pressure decreases with altitude its temperature decreases. The rate of temperature decrease is 9.8 K km^{-1}, the dry adiabatic lapse rate. Given that the air parcel keeps the same water vapor content during its ascent, the saturation is attained when the parcel reaches the dew temperature, at the lifting condensation level (LCL). At this level, water vapor starts to condense. Once the parcel is saturated, it conserves the equivalent potential temperature (in absence of any precipitation) during its upward motion, following a moist adiabat. Then, the temperature changes with altitude at a lower rate than for the unsaturated parcel, because latent heat is released due to the condensation processes, warming even more the air parcel with respect to the environment and further increasing its buoyancy. The moist adiabatic lapse rate is around 6.5 K km^{-1} and varies with the temperature. It can happen that at the LCL the parcel is denser than the environment. It will then experience a downward acceleration unless it has enough kinetic energy to overcome this critical atmospheric layer. The energy that the parcel needs to provide to continue its moist adiabatic ascent is called convective inhibition (CIN) and is defined as:

$$CIN = \int_{z_0}^{z_{LFC}} g \frac{T_{v_{parcel}} - T_{v_{env}}}{T_{v_{parcel}}} dz = \frac{1}{2} w_{min}^2, \tag{1.1}$$

where g is the acceleration due to gravity, $T_{v_{parcel}}$ is the virtual temperature of the ascending air parcel and $T_{v_{env}}$ is the virtual temperature of the environmental sounding. w_{min} is the minimum upward speed required for the parcel to attain the LFC and overcome the inhibition layer. When the atmosphere is dry and stable or in the presence of subsidence the CIN is large. For convection to further develop, the vertical speed of the parcel has to be sufficient to reach the level of free convection (LFC). At this altitude, the parcel becomes less dense than the environment and is accelerated until it reaches the equilibrium level (EL), also referred to as level of neutral buoyancy (LNB). The maximum energy that the air parcel could gain because of buoyancy is called convective available potential energy (CAPE). It is:

$$CAPE = \int_{z_{LFC}}^{z_{EL}} g \frac{T_{v_{parcel}} - T_{v_{env}}}{T_{v_{parcel}}} dz = \frac{1}{2} w_{max}^2, \tag{1.2}$$

where w_{max} is the upward speed that the parcel would reach if all the CAPE is consumed. Moreover, for a given amount of buoyancy produced, the narrower the parcel the larger the upward acceleration. The value of CAPE is a measure of the instability of the atmosphere, which allows to estimate the severity of convection. Deep moist convection occurs when the air parcel succeeds to overcome the CIN and to have access to the CAPE stored above, between the LFC and the EL. If the parcel continues above the EL while rising air slows down, an overshoot will appear at the top of the deep convective cloud. In the convective mechanisms exposed here, mixing of the ascending air parcel with the environment through entrainment and detrainment is neglected. The parcel remains undiluted during its uplift, and thus the conservation of equivalent potential temperature holds (in absence of any precipitation). If mixing was considered, the actual energy gain between the LFC and the EL would diminish because the θ_e of the parcel would be closer to that of the environment. This would prevent the air parcel from reaching w_{max}. For instance, a typical CAPE value of 2000 J kg^{-1} would lead to a w_{max} of around 60 m s^{-1} in the absence of entrainment into the convective clouds. Such value for upward speed is extremely high and has been rarely reported (Wang, 2003).

Convective or cumulus clouds arising from local moist convection follow a three-modal distribution in the tropics (Fig. 1.7).

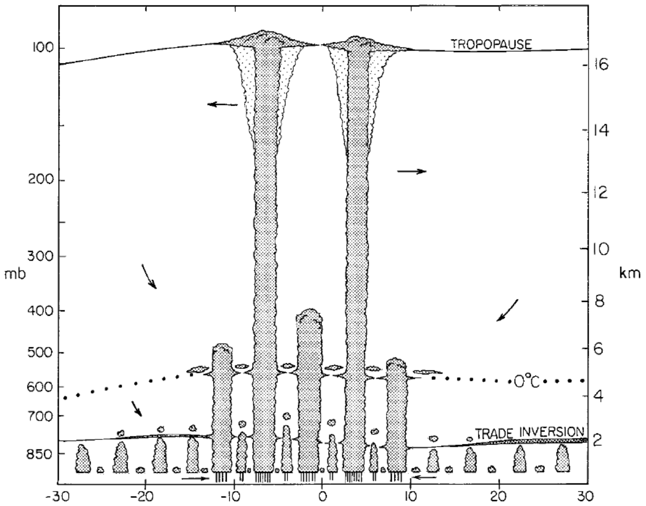

Figure 1.7: Three main types of tropical convective clouds: cumulus humilis, cumulus congestus, cumulonimbus. The three stable layers that limit their vertical development are respectively the trade wind inversion, the freezing level and the tropopause. Overshoots and cirrus anvils from cumulonimbus are visible above and in the vicinity of the tropopause. The location of the cumulonimbus indicates that the greatest convective instability correspondts to the latitudes of the ITCZ (in summer and winter). Reproduced from Johnson et al. (1999).

They are divided into cumulus humilis, cumulus congestus and cumulonimbus, depending on their vertical development, that is given by the instability of the warm moist parcels. The altitude of the cloud top for the cumulus humilis is constraint by the stable layer at the top of the boundary layer. Cumulus humilis are the shallowest, and cloud droplets do not have time to produce enough large rain drops. Cumulus congestus and cumulonibus exhibit a much greater vertical extent, and are precipitating. The top of the cumulus congestus is placed at around 5 to 6 km, the altitude of the freezing level. No solid phase is present, and buoyancy comes from the latent heat release of condensation processes. Precipitation is produced by coalescence of liquid droplets. Cumulonimbus or thunderstorms correspond to deep convection. As they develop above the 0°C isotherm, extra latent heat is released through vapor deposition on ice crystals and the freezing of liquid water. This energy supply is much greater than in congestus, allowing the cumulonimbus to grow past the tropopause, at around 17 km. Well-developed cumulonimbus are characterized by an anvil-like top, caused by wind shear or inversion near the tropopause. The anvil is the visible consequence of divergence close to the tropopause. Cumulonimbus are mixed-phase clouds (with liquid and iced hydrometeors), and capable of producing lightning. The lifetime of an individual cumulonimbus is around 30 to 50 minutes. These isolated convective clouds can evolve, if the environmental conditions are favorable, into mesoscale convective systems (MCSs), a highly organized type of moist convection. These systems present longer lifetime and a huge potential for intense and lasting precipitation.

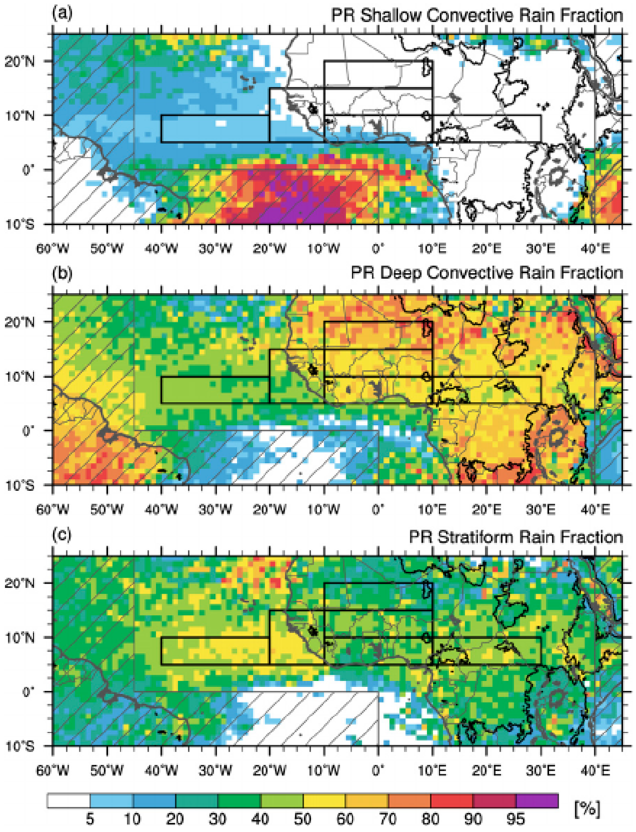

Figure 1.8: Mean fraction of (a) shallow convective, (b) deep convective and (c) stratiform precipitation from the TRMM PR during JAS 1998-2012. Reproduced from Janiga and Thorncroft (2014).

In a general way, precipitation is considered to be of two types, stratiform or convective. These types are defined in terms of their vertical velocity scales. Convective (stratiform) precipitation is a precipitation process in which the vertical air motion is large (small) as compared to the terminal fall velocity of ice crystals and snow (Houze, 1994). Deep convection, which is very frequent in continental Africa, generates between 50 and 70% of precipitation in the ITCZ region (Fig. 1.8b). There, from the Atlantic to Ethiopia, a significant contribution of 30 to 50% to total precipitation is stratiform-like (Fig. 1.8c). Offshore over the ITCZ, the contribution of deep convective and stratiform precipitation decreases and increases, respectively. Note that stratiform precipitation is closely linked to convective processes. Stratiform clouds are primarily associated with massive clouds such as MCSs, that exhibit a mixture of convective and stratiform structures. Note as well that the fraction of rain attributed to deep convection is due to both isolated clouds or MCSs. Finally, the contribution of shallow convective clouds to precipitation is negligible. It only appears over the coastal regions of the Gulf of Guinea (Fig. 1.8a). These clouds do not produce much precipitation because they lack of vertical extent for rain drops growth.

1.2.4 Mesoscale Convective Systems

Moist convection can be organized into large complexes denominated mesoscale convective systems (MCSs). Houze (1994) defines an MCS as a *cloud system that occurs in connection with an ensemble of thunderstorms and produces a contiguous precipitation area* $\sim$*100 km or more in horizontal scale in at least one direction*. In a MCS, this large precipitation is both of convective and stratiform type, which present horizontal scales of about 10 and 100 km, respectively. It is associated with circulations of different scales as well, such as convective updrafts and downdrafts and mesoscale circulations. Mesoscale convective organization can happen in several forms: squall line (Zipser, 1977), mesoscale convective complex (MCC, Maddox (1980)), organized convective system (OCS). Squall lines, which are very typical in West Africa, have been more intensively studied than other types of mesoscale convection.

A squall line is characterized by a front line of convective cells perpendicular to its motion, and a trailing stratiform region (Fig. 1.9).

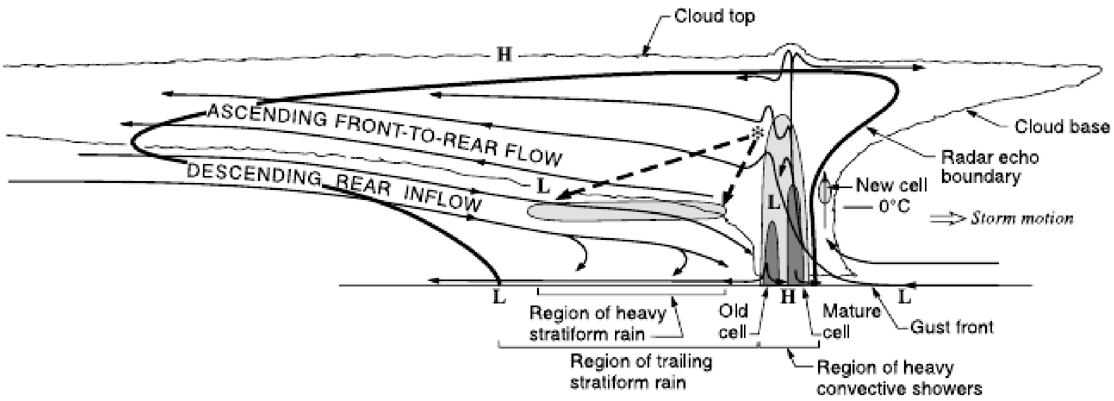

Figure 1.9: Structure of a tropical squall line represented by a cross section parallel to its motion. The squall line is in its maturity stage of its lifecycle (see text for details). It presents convective cells in the front: new developping ones, mature ones with the strongest updrafts generating overshoots at the tropopause and old ones that eventually become embedded in the trailing stratiform region. The large stratiform region presents mesoscale circulations: an ascending flow from the convective parts and a descending inflow fed by the surrounding air. Both the convective and stratiform regions produce precipitation. Reproduced from Houze et al. (1989).

Fast updrafts and downdrafts are located in the convective region, where the convective cells present different stages of development. New shallow cells (cumulus humili and congestus) may appear in the very front of the MCS, followed by older cells, mature ones. The updrafts of a mature cell transport moist air parcels and hydrometeors up to the equilibrium level that corresponds to the cloud top, and sometimes overpass it generating overshoots until their upward velocity is zero. The convective downdrafts contain the negatively buoyant air cooled by evaporation of rain, and when arriving at the surface these cool and dense air masses create cold pools. In their cloud-resolving model study, Diongue et al. (2002) simulated a squall line with an associated temperature drop of 9 K at the surface due to cold pools. Cold pools are found to maintain convection in two ways. On the one hand, they favor the growth of the convective system (Tompkins, 2001), whose updrafts have, in turn, the potential to remain more undiluted, reaching higher altitudes and becoming deeper (Khairoutdinov and Randall, 2006). Thus, cold pools help deepen the front cumuli into strong cumulonimbus. On the other hand, the turbulent density currents in the borders of the cold pools act like a cold front forcing the uplift of warm moist air in the near-surface. This mechanism may trigger new convective cells.

A significant amount of ice hydrometeors are advected from the convective towers to the rear of the MCS, forming the stratiform anvil region. The widespread upward velocity in the stratiform cloud is $\sim$tens cm s^{-1}, and can be due to a small positive buoyancy of the air in the tops of the cumulonimbus. The ice particles here mainly grow by water vapor deposition that will later reach the melting layer below. In the convective region, the dominant mechanisms producing rainfall are snow generation by riming, a process in which supercooled droplets of water collide with the crystal and freeze to it, and coalescence of rain drops. MCSs exhibit also a descending inflow of environmental dry low-θ_e air. Dry air masses are detrimental to the MCS during the developing stages of the convective cells by increasing the CIN that convection is unable to erode. On the contrary, in the mature stage of the MCS, this rear-to-front inflow feeds the dense subsidences and cold pools get intensified. Therefore, dry mid-level environmental air entering the stratiform region has a positive feedback on the strength of the convection if the latter is well established. Many of the properties described before for squall lines apply to all types of MCSs despite the morphological differences among them.

A MCS can last from several hours to 3 or 4 days. During their lifetime, MCSs exhibit three stages of development: initiation, maturity and decay. In the initiation stage, several isolated convective cells merge into a contiguous precipitation area, where most of precipitation is of convective type. In the maturity stage, a large stratiform region is formed from old cells. Those cells weaken and eventually integrate the stratiform part of the MCS, while new cells trigger. When this triggering ceases, the MCS enters the dissipating stage. At that point, the MCS consists only of well-developed or decaying old cells and an extended stratiform cloud deck. Generally, the amount of stratiform rain ranges between 25 to 50% of the total (Houze, 1994). An example is shown in Fig. 1.10.

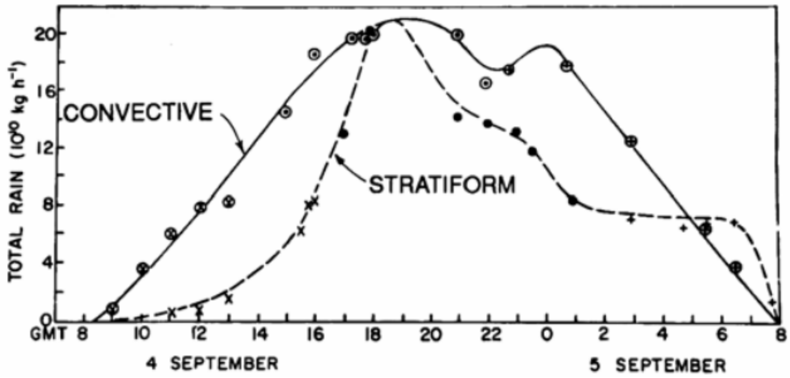

Figure 1.10: Time evolution of convective and stratiform-type radar-retrieved precipitation produced by a squall line observed over the Eastern Atlantic lasting for 48 hours. Over its lifetime, the stratiform rain accounts for 40% of total. Reproduced from Houze (1977).

MCSs propagate westward in the north of Africa at speeds of 10 to 15 m s^{-1}, guided by the AEJ. The vertical wind shear between the southwesterly monsoon flow and the AEJ plays a major role in sustaining the systems. A significant increase of wind speed with altitude will tilt the convective updrafts so that they are not vertically aligned with the downdrafts and associated precipitation. Otherwise, the convective cells tend to dissipate much sooner. The AEJ supplies with the mid-level dry air that feeds both the convective and rear mesoscale downdrafts of the MCS.

The contribution of MCSs to the total precipitation is found to be more than 50% in West Africa, and up to 90% (e.g., Bayo Omotosho, 1985; Le Barbé et al., 2002; Mathon et al., 2002; Fink et al., 2006). MCSs are thus the first precipitation makers. These observation-based estimates of MCSs relative contribution to precipitation vary with the period and regions studied. Interestingly, the part of precipitation due to MCSs increases with latitude. Despite the subtle variations in the definition of MCS, Bayo Omotosho (1985) and Fink et al. (2006) support the idea that the meridional increase in the MCSs contribution to total precipitation from Guinean to Sahelian regions is explained by a higher degree of organization. The degree of organization of the MCSs can be evaluated through their horizontal extension, life duration and propagation speed. An enhanced organization can be explained by a sheared environment inhibiting the convective cells dissipation, or more local reasons like cold pool outflows forcing the triggering of new cells. The degree of organization of MCSs also presents a zonal dependence across the African continent, in relationship with the AEWs. Convection is quite unorganized to the East of Ethiopia, and becomes organized to the west of the Ethiopian Highlands as the lower atmosphere moistens, preceding the AEW initiation (Mekonnen and Rossow, 2011). Inversely, Fink and Reiner (2003) examined the role of AEWs in the genesis of MCSs, and found that their forcing also increases from Guinean to Sahelian regions, and from east to west as AEWs intensify. Furthermore, the largest values of precipitation are usually associated with the northerly phase of AEWs (Reed et al., 1977; Janiga and Thorncroft, 2016).

1.3 Dust

1.3.1 Distribution and Recent Field Campaigns

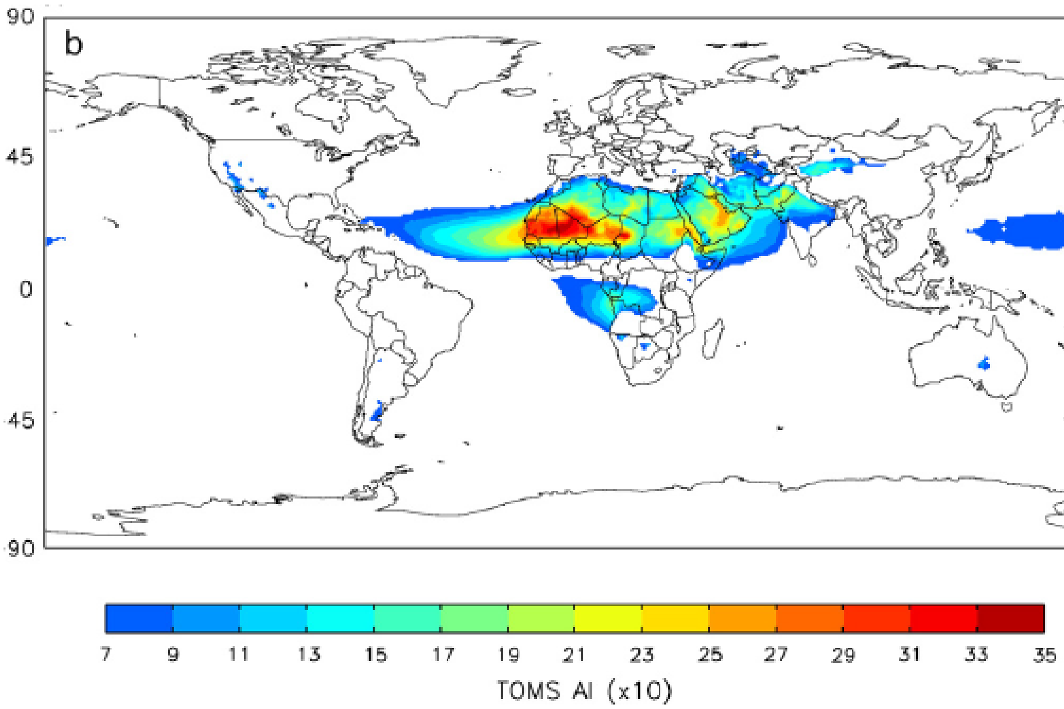

Figure 1.11: May-July mean Aerosol Index (AI) product between 1980 and 1992 from the Total Ozone Mapping Spectrometer (TOMS). Reproduced from Engelstaedter et al. (2006).

Desert aerosols are mostly distributed over the northern hemisphere, over the tropical Atlantic and Africa, over the Middle-East and the northwestern part of China (Fig. 1.11). Desert dust represents the first mass source of aerosols in the world and 50% of dust global emissions come from the northern part of Africa. Moreover, the Saharan sources are considered as the most active ones in the world.

Dust aerosols can vary in size from 1 nm to 100 μm. They are distributed in size following three modes. Fine aerosols of less than 1 μm comprise the Aitken (< 0.1 μm) and accumulation (> 0.1 μm) modes. Those aerosols with diameters larger than 1 μm belong to the coarse mode (Mahowald et al., 2014). The size distribution often follows a log-normal distribution but varies throughout the life cycle of dust particles through aggregation and deposition, downwind from the source regions where dust particles are emitted. By now, models lack ability to capture the evolution of the size distribution, and its detection from satellite retrievals is currently investigated (Mahowald et al., 2014).

Dust and its effects on the atmosphere are an active research field. One of the main challenges comes from the scarcity of observations due to the difficult access to the source regions, which present extreme conditions such as the Sahara desert. For a long time, visibility data were the only available observation to investigate the spatio-temporal variability of dust. Nowadays, radiometers onboard polar-orbiting satellites, such as MODIS (Moderate Resolution Imaging Spectroradiometer), provide us with valuable observations but lack the potential for studying the diurnal cycle of dust as these satellites overpass the Equator twice per day and cannot observe continuously the same Earth's surface area. The Sun photometers from the AErosol RObotic NETwork (AERONET) ground-based stations allow to partially overcome this issue, as they measure optical properties of dust continuously, but during daytime only. Other issues in satellite observation concern the partial screening of dust plumes by clouds at higher levels and the determination of the sources the dust plumes were originated in. The temporal availability of satellite dust products is a major aspect for the identification of dust sources, as the temporal lag between the dust emission and the image retrieved by the satellite induce to errors in the localization of sources (Schepanski et al., 2012). To identify the sources, a technique commonly used is the back-trajectories of dust-laden air parcels (e.g., Flamant et al., 2009; Schepanski et al., 2012).

The increased interest on atmospheric dust has led to several field campaigns to provide one with extra observational data sets, such as BoDEx (Bodélé Dust Experiment, 2005), African Monsoon Multidisciplinary Analysis (AMMA, 2006), Geostationary Earth Radiation Budget Intercomparison of Longwave and Shortwave Radiation (GERBILS, 2007) or Fennec (2011). These projects are mostly focused on the western African sources.

1.3.2 Emission and Transport

Dust undergoes different phases during its life cycle, whose duration depends on both its size and on meteorological and environmental conditions. Once dust is uplifted and injected into the atmosphere, it experiences a vertical mixing and horizontal transport over large distances, specially for the lightest particles. During their transport they will be deposited through dry sedimentation (under conditions for which the gravity force is predominant) or wet deposition (washed out of the atmosphere through rainy processes).

Engelstaedter et al. (2006) distinguish four regions of dust sources in northern Africa: the Bodélé Depression in Chad; West Africa comprising areas in Mauritania, Mali and Algeria; the Libyan desert and the Nubian desert with sources over central Egypt and Sudan. Northern Africa presents a strong annual cycle in terms of dust distribution (Engelstaedter and Washington, 2007), with the lowest dust values in October and November and the maximum values from May to July (Fig. 1.12). The Bodélé Depression is an active source during the whole year, whereas the rest of the sources are active from spring to summer. Both the West African sources and the eastern coast of Sudan show maximum values of dust load in June and July (Engelstaedter et al., 2006).

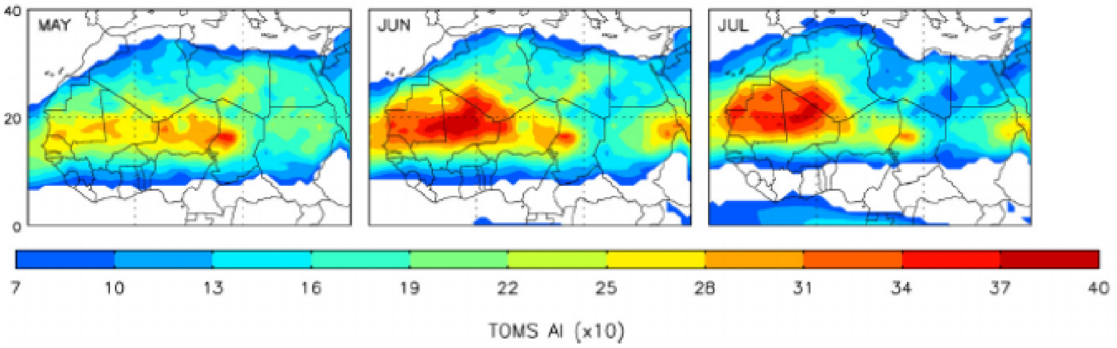

Figure 1.12: Monthly mean May/June/July Aerosol Index (AI) between 1980 and 1992 from TOMS. Reproduced from Engelstaedter et al. (2006).

The dust uplift mechanism is a threshold phenomenon that essentially depends on the wind and soil characteristics: roughness, size and mass of the dust particles, moisture. Once a dust particle is mobilized, its long-term injection into the atmosphere depends on the resulting forces exerted on it. Heavy dust particles will fall to the ground little after being suspended, under the force of gravity, whereas lighter particles can remain suspended longer and be transported far away. Shao (2008) categorizes sizes of dust particles in terms of displacement and uplift properties. The largest particles can only be displaced on the surface. Mean-sized dusts follow a process called saltation, they are uplifted but fall down immediately as if they jumped. When colliding with the surface they break out into smaller particles. This phenomenon is named sandblasting. These fine dusts resulting from sandblasting are injected into the atmosphere, but only those with a diameter smaller than 20 μm remain in suspension long enough to be available for long-range transport. Different-scale meteorological mechanisms are responsible for dust mobilization and uplift in northern Africa. Thus, dust and its radiative effect undergo a diurnal cycle forced by those mechanisms in play (e.g., Chaboureau et al., 2007; Kocha et al., 2013).

During the BoDEx field campaign in February/March 2005, ground-based instruments were deployed in the region of the Bodélé Depression with the aim of studying the dust properties and boundary-layer meteorology, as it is recognized as world's greatest source of dust. The Bodélé Depression is dominated by the northeasterly Harmattan which accelerates due to a channelling effect between the Tibesti and Ennedi Mountains (Washington et al., 2006; Flamant et al., 2009). The observations taken during the campaign show that dust outbreaks in this area are time-correlated with the diurnal cycle of near-surface winds (Fig. 1.13). The near-surface winds peak at 0900 UTC and correspond to the nocturnal Low Level Jet (LLJ), the main driver of dust emission in the Bodélé Depression (Washington et al., 2006).

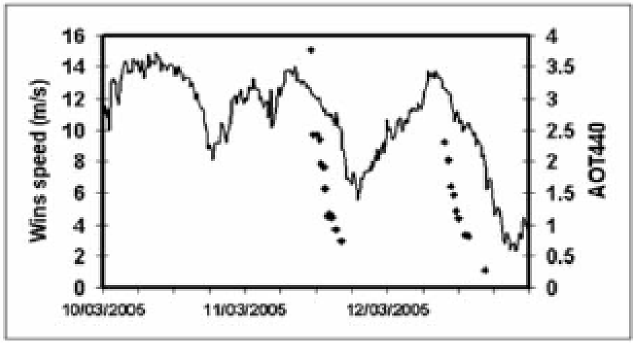

Figure 1.13: Aerosol optical depth at 440 nm (diamonds) and 15-min average of wind speed (lines) during the 10-12 March 2005. Reproduced from Todd et al. (2007).

Over West Africa, LLJs are also key to dust emission in the Saharan and Sahelian sources through similar mechanisms to those described for the Bodélé Depression, but other factors arise as well. Dust mobilization in the ITD region can be due to different-scale meteorological mechanisms. Dust uplift by synoptic dry cyclones generating strong near-surface winds was reported during the AMMA campaign (Bou Karam et al., 2009), as well as by the monsoon flow, especially during the night (e.g., Bou Karam et al., 2008; Marsham et al., 2008). Density currents resulting from moist convection can uplift great quantities of dust. They form a front of dust in the leading edge of the convective system. These convective dust storms are named haboobs, as derived from the Arabic (Sutton, 1925).

The maximum occurrence of aerosols uplifting by haboobs happens in the beggining of the summer, when the ITCZ is over the continent and the soil is still dry and vegetation-free. Haboobs have been observed south of the ITD from *in situ* observations from a flight during AMMA in June 2006 (Flamant et al., 2007) and GERBILS in June 2007 (Marsham et al., 2008). The mesoscale strong winds generated from the outflows of convective storms, even from cumulus congestus, participate significantly to dust mobilization whenever the synoptic-scale winds are weak. Dust uplift by the density currents over the Sahara has been found to be large as the moist convection is enhanced by the Atlas Mountains (Knippertz et al., 2007), and suggests that this mechanism could be important in other mountainous regions such as the Tibesti or Hoggar Mountains. Over Sudan, haboobs are an important contributor to dust production. The rain is characteristic of the Sudan haboobs, but not of those in the dry Nubian desert or South-Egypt sources (Sutton, 1925).

The dust emitted in northern African sources can be injected in the large-scale circulation as the Harmattan flow lifts it above the monsoon flow at the ITD, and is then embedded within the AEJ, allowing its further transport over the Sahelian and West Sudanian regions (Flamant et al., 2009). They are generally transported to the southwest at altitudes between 3 and 5 km. Over the Sahara this layer is commonly denoted Saharan Aerosol Layer (SAL). Moreover, the dust exported from the Sahara in summer is transported over the Atlantic Ocean, even reaching the Americas (Schepanski et al., 2009).

Because of their impact on climate, dust must be incorporated in weather and climate models. For emissions to be realistic in the models a good representation of the wind distribution is needed, as the vertical dust flux in the models is usually parameterized in terms of the saltation and sandblasting processes once the wind speed is greater than the emission threshold. During BoDEx, Todd et al.

(2007) set a value for the erosion wind speed threshold of 10 m s^{-1}. This high value of wind speed threshold is a constraint for coarse-resolution models that reproduce the wind speed distribution poorly, showing too low values and leading to an underestimation of the emissions in the Bodélé Depression. The significant contribution of haboobs to the dust emission in northern Africa remains also underestimated in models with too coarse resolution, wind bursts from moist convection are not well represented. Recent efforts have been made on the parameterization of haboobs (Pantillon et al., 2015). Increasing the resolution of the model can help to estimate the emissions more accurately (Chaboureau et al., 2016). Furthermore, the convection-permitting simulations capture the scavenging of dust by rainy processes, leading to a more realistic dust loading in the atmosphere and a more complete description of the dust life cycle. A main added value of models is to fully describe the diurnal cycle of dust (Kocha et al., 2013), which observations can not provide, and to give an insight on the vertical distribution of dust.

1.3.3 Effects on the Atmosphere

The dust aerosols are considered a main component of the climate of the Earth. They have impacts on the atmosphere through their radiative properties by absorbing or scattering radiation, these are called the **direct effects**; then, in consequence, changing other weather phenomena such as precipitation, the **semi-direct effects**; or by interacting with the cloud microphysics, mainly through nucleation processes, the **indirect effects**.

Direct effects

Dust has an important radiative effect from regional to local scales, that depends on the size distribution of dust particles, as well as their number and mass concentration. Overall, the dust direct radiative effect in northern Africa is atmospheric warming, surface cooling and a small forcing at the top of the atmosphere (Zhao et al., 2011). Dust can also have an important impact on the radiative budget of the atmospheric layer where dust is located and below. The dust heating rates present a vertical variability within a dust plume as a result of the vertical stratification of dust (Tulet et al., 2008; Lemaître et al., 2010), as well as a dependence on the radiation wavelengths. During daytime dust scatters and absorbs radiation both in the visible (shortwave) and infrared (longwave) regions of the electromagnetic spectrum, but in a lesser way for the latter. During an intense dust episode in June 2006, Lemaître et al. (2010) found an average warming of 1.5 to 4 K day^{-1} within the dust plume, the values varying with the altitude between the dusty layers depending on their optical thickness. They find that the longwave radiation contributes to about 10% of the heating rates in the plume, and about 20% near the dust-free surface. During the nighttime, in the absence of solar radiation, values of heating and cooling rates are found to be of the order of 1 K day^{-1} and the dust radiative effect is not negligible anymore. In their modeling case study of the transport of a dust plume in the ITD area in March 2006, Tulet et al. (2008) show a net vertical temperature variation of 9.5 K in the lowest 2 km of the atmosphere between the heated dust layer and the cooled surface, during daytime, when comparing a dust-free simulation with another one that considers the radiative effect of dust.

Semi-direct effects

The semi-direct effects of dust concern the dynamical and thermodynamical response of the atmosphere to the temperature variations generated by the radiative effect of dust. The presence of dust plumes located above the monsoon layer, generating a mid-level heating and near-surface cooling as in Tulet et al. (2008), tends to stabilize the atmosphere.

At the synoptic scale, disturbances of the AEJ are expected with variations of the meridional gradient of temperature through the thermal wind equilibrium, as the dust loading and radiative forcing are much greater over the Sahara than over the Guinean Coast. For instance, taking into account the interannual variations of the aerosol forcing with respect to a fixed climatology was found to be beneficial for the forecast of the AEJ in the ECMWF model (Tompkins et al., 2005). Lavaysse et al. (2011) performed simulations of a case study in July 2006 to investigate the radiative effect of dust on the heat low and the Sahelian convective activity. They showed that the heat low thickens, leading to a stronger meridional temperature gradient that strengthens the AEJ. The latter helps maintaining more intense AEWs. The wind variations also occur at the surface, driven by temperature changes there, which can ultimately affect the dust emission itself. Using the COSMO-ART (COnsortium for Small-scale MOdelling-Aerosols and Reactive Trace gases) model, Stanelle et al. (2010) simulated two dust episodes at 28 km resolution over West and northern Africa in March 2006 from AMMA and in June 2007 from GERBILS. They found that considering the radiative effect of dust has a positive feedback on dust, whose emissions increase around 20% in both case studies.

The thermodynamical changes can affect the convective activity and precipitation as well. Two-day forecasts over West Africa with the Méso-NH model by Chaboureau et al. (2007) show a more realistic convective clouds cover when considering a prognostic dust scheme rather than a climatology. Solmon et al. (2008) have studied the climate impact of the radiative forcing of aerosols on the West African Monsoon and over the precipitation of Sahel during the months of June, July and August of 1996-2006. They used the regional climate model Reg-CM coupled to an aerosol model with a resolution of 60 km. They find a mean reduction of 8% in precipitation over the whole simulation domain. South of 17° N, the reduction is due to a net surface cooling inhibiting the convective activity. Zhao et al. (2011) studied the radiative impact of dust on precipitation from May to September 2006 with the use of the WRF-Chem model at a horizontal resolution of 36 km. They find that the atmospheric stability is increased during the daytime and reduced in the nighttime. This generates an average diminution of the precipitation in the late afternoon and an increase during the night and early morning (Fig. 1.14). Overall, the simulation with radiative effect of dust accounts for around 4% less precipitation than the dust-free simulation.

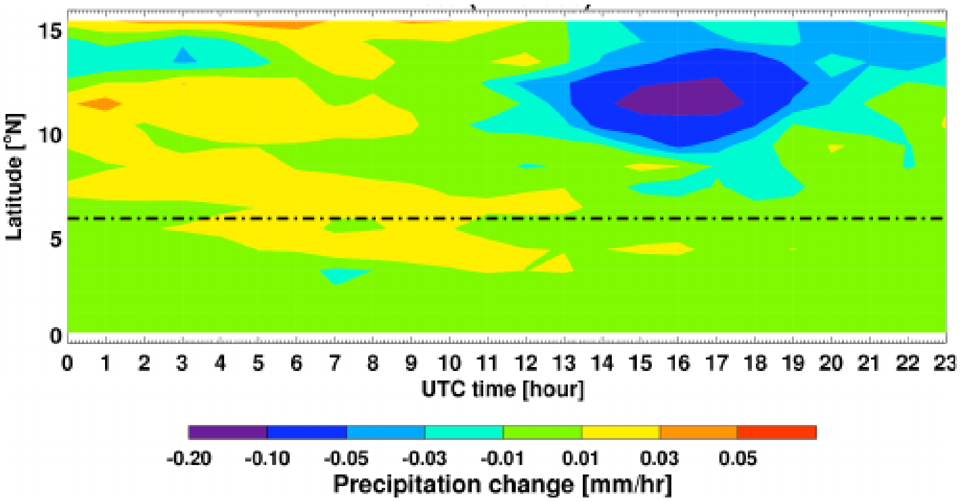

Figure 1.14: Variation of the diurnal cycle of the zonal averaged precipitation between 15°W and 10°E, due to the dust radiative impact, as simulated by the WRF-Chem model during the monsoon season in 2006. Reproduced from Zhao et al. (2011).

Indirect effects

Aerosols have a significant impact on clouds microphysics due to their hygroscopic properties, modulating the cloud albedo (Twomey effect), the outgoing terrestrial radiation and the cloud amount. Nucleation is the first process in the phase transitions between the water phases in the atmosphere. The homogeneous nucleation through spontaneous phase transition rarely takes place in the atmosphere, and aerosols are needed for the formation of clouds through the heterogeneous nucleation. The aerosols can have a role as CCN (Cloud Condensation Nuclei) or as IN (Ice Nuclei), whether they favor the condensation of cloud droplets or the formation of ice crystals. Dust behaves mainly as IN as it is mostly hydrophobic. Without the presence of dust, the cloud droplets freeze at around -40°C. Mineral dust from the Sahara was found to be able to glaciate clouds at temperatures higher than -10°C (Sassen et al., 2003), showing the importance of dust in providing with a substrate for ice initiation. Dust particles have been observed to suppress precipitation by promoting the formation of small cloud droplets that do not reach the size of rain droplets (Rosenfeld et al., 2001; Lohmann and Feichter, 2005). The indirect effects are, however, beyond the scope of this thesis.

1.4 Objectives of the Thesis

The first main objective of this thesis is to investigate the processes controlling precipitation during the dust outbreak of 9-14 June 2006 over northern Africa. Different types of cloud systems contribute to precipitation. They will be examined to understand how each kind of cloud systems contributes to the precipitation variability. Mesoscale convective systems present a high degree of organization involving a variety of spatiotemporal scales and contribute the most to precipitation in northern Africa. A relevant aim of the thesis, related to the first objective, is thus to determine the main drivers of the mesoscale convective organization. The effect that the representation of deep convection, whether explicitly allowed or parameterized, in the Méso-NH model has on the simulated precipitation and its variability is investigated. Particularly, the question of the role of the type of convection representation in capturing the organization of MCSs more realistically will be examined.

The second main objective concerns the investigation of the radiative effect of dust on the atmosphere, notably on precipitation. The reasons leading to the precipitation modulation will be studied. This impact is expected not to be negligible as a consequence of the important dust concentrations observed during the period. The impact of dust on the variation of the rainfall potential per type of precipitating system will be addressed, as well as its impact on the MCSs.

Chapter 2

A Dust Outbreak over Northern Africa

Contents

2.1 The 9-14 June 2006 AMMA Case Study

The dust outbreak that occurred from 9 to 14 June 2006 was investigated during the Special Observing Period 1, dedicated to the onset phase of the monsoon, of the AMMA project (Redelsperger et al., 2006). The field campaign took place on 2006, embedded within the Enhanced Observing Period that lasted from 2005 to 2007.

The onset of the West African monsoon is characterized by a shift of the ITCZ from 5°N to 10°N and is highly controlled by the SST in the Gulf of Guinea. There, the upper layer of the ocean was 2°C warmer in June 2006 than in 2005 or 2007 (Lebel et al., 2010). As a consequence, the convective activity was weaker than usual until 3 July, when the ITCZ was located at 10°-12°N, ten days later than the mean onset date (Janicot et al., 2008). Further, the monsoon winds were weaker and the AEJ stronger in June 2006 than the climatological mean. The AEWs propagate along the southern and northern parts of the AEJ axis. Between June and September 2006, the longest period of wave activity was between mid-August and mid-September. In June, the altitudes of the southern waves between 5° and 15°N were near the AEJ level and are associated with convection (Janicot et al., 2008). During the 6-day period, several precipitating systems were observed and two AEWs propagated westward (with 2-3 days interval) over northern Africa, as shown in the Hovmöller diagram in Fig. 2.1. Some precipitating systems propagated together with the AEWs. June 2006 was also characterized by lower aerosol optical depths (AODs) than usual. Given that large AODs are mostly due to mineral dust at this time of the year, this AOD decrease is explained by the reported inhibited convective activity as convective systems contribute to dust emissions over the vegetation-free and dry pre-monsoon soils.

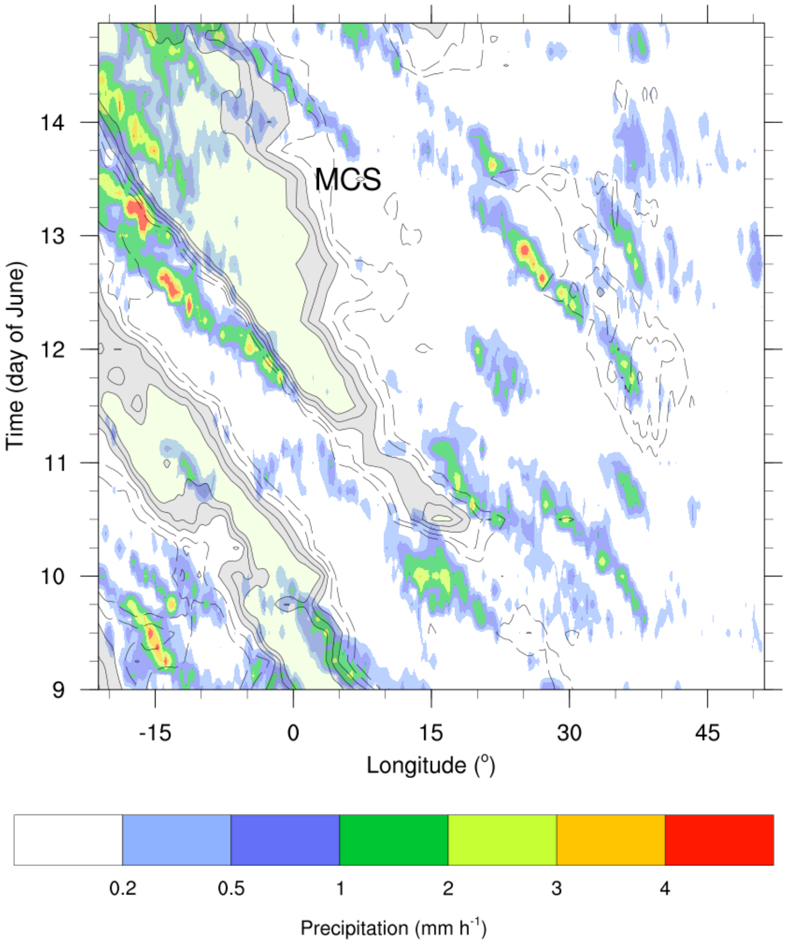

Figure 2.1: Hovmöller diagram of precipitation from TRMM (Tropical Rainfall Measuring Mission) product 3B42 and meridional wind speed by the ECMWF (European Centre for Medium-Range Weather Forecasts) analysis at 3.8 km-altitude, from 21°W to 51°E and averaged between 5° to 15°N. Solid (dashed) lines represent southerly (northerly) winds. The diagram shows two AEWs propagating to the west as well as the MCS passing over Benin in the night of 14 June 2006.

On 13 and 14 June intense aircraft operations took place over Benin and Niger. During these two days, two French aircraft (the Falcon 20 and ATR-42) flew between Niamey and Cotonou (at 8000 and 700 m above mean sea level, respectively). Dropsondes were launched and the lidar LEANDRE 2 (Lidar Embarqué pour l'étude de l'Atmosphere : Nuages, Dynamique, Rayonnement et cycle de l'Eau) was onboard Falcon 20 to assess the vertical structure of the atmosphere. Prior to these days, strong mineral dust emissions occurred in the regions of Bodélé (Chad) and Sudan mostly from 10 to 11 June, due to enhanced LLJs over the dust sources (Flamant et al., 2009). The dust load was advected westward mainly within the AEJ, after being lifted to the altitude of the AEJ by the Darfur Plateau and the Ennedi Mountain and by the encounter of the monsoon flow over the ITD. AOD retrievals from MODIS during 13 and 14 June (Fig. 2.2) show the largest AOD values of around 2 over the Sahelian band and over the Sahara west of the Hoggar Mountains. The AODs are lower than 1 over the source regions that were active the previous days. Dust aerosols even reached the Guinean Coast on 13 and 14 June, where values greater than 0.6 were observed. The decrease in AOD between the two days over northern Benin is further discussed by Flamant et al. (2009) and related to a propagating MCS that originated over the Jos Plateau in the evening of the 13 June and passed through Benin during the night. From Fig. 2.1, this MCS seems to propagate within the northerly part of an AEW at the beginning and within the ridge of the wave between 0° and 5°W.

Other studies were dedicated to this outstanding 6-day period because of the heavy loading in dust and the availability of airborne and spaceborne observations. The heating rates due to the observed dust plumes were computed by Lemaître et al. (2010) from retrievals of LEANDRE2 and CALIOP (Cloud-Aerosol Lidar with Orthogonal Polarization) onboard CALIPSO (Cloud Aerosol Lidar and

Infrared Pathfinder Satellite Observations). They analyzed the vertical variability of radiative heating profiles within the plume, and found differences in the warming/cooling rates with latitude. The highest rates were found over southern Benin, where cumulus clouds at the top of the monsoon layer are common, and over northern Benin and Niger over the dry Sahel. In another study, Crumeyrolle et al. (2011) proposed a new parameterization of dust size distribution based on airborne measurements during 13 and 14 June, and found that dust is more concentrated in the boundary layer over warmer surfaces in relationship with the type of surface cover.

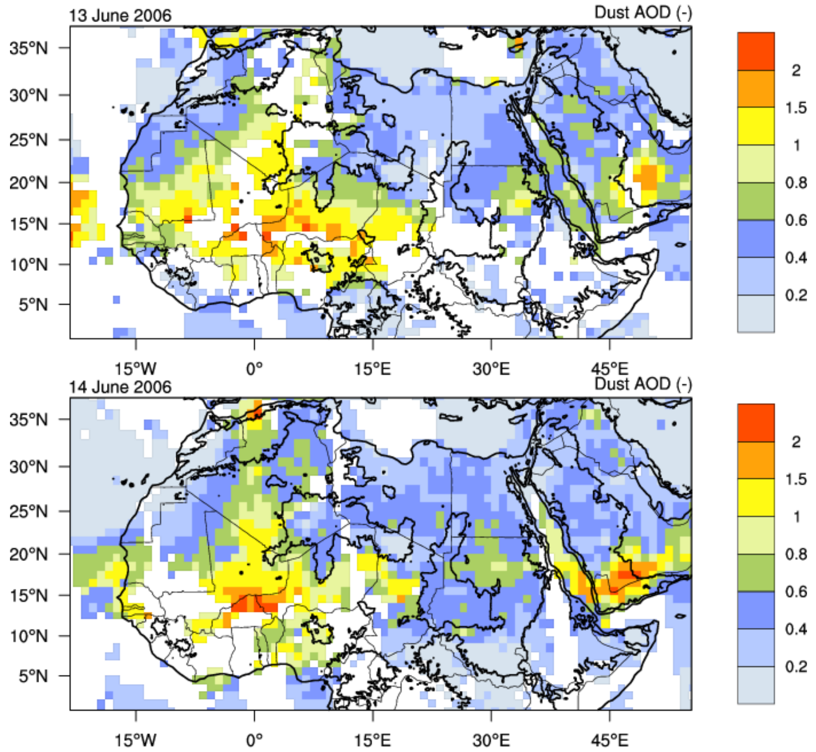

Figure 2.2: Aerosol Optical Depths (AODs) as observed by MODIS at 1330 UTC on 13 and 14 June 2006. AODs greater than 0.6 are observed over the Guinean Coast. Over northern Benin, the AOD values decrease between 13 and 14 June. In white, unavailable data.

2.2 Simulations with the Méso-NH Model

The Méso-NH model (Lafore et al., 1998) is the French non-hydrostatic atmospheric research model. Three simulations were performed with Méso-NH version 5-1-3 to examine the controls on precipitation processes during the case study of 9-14 June 2006 in Northern Africa. The simulation called HiRes is presented first, and the other two simulations (LowRes and HiNod) are described afterwards.

2.2.1 The HiRes simulation

2.2.1.1 Preparation of the simulation

Prior to running a simulation with Méso-NH, the initial and boundary conditions must be prepared. The current study being a real case, these conditions are given by the large-scale meteorological analysis of the European Centre for Medium-Range Weather Forecasts (ECMWF). We used an initial file on 9 June at 0000 UTC, and coupling files every 6 hours to prescribe lateral boundary conditions to the model. A physiographic file was produced first, where we chose a Mercator projection as the domain is close to the Equator, a horizontal resolution of 2.5 km and a domain of 1536×3072 grid points in the horizontal. This makes a total surface of approximately 29,5 million km^2 (3840 km in latitude and 7680 km in longitude). The physiographic file contains the type surface coverage through the global ECOCLIMAP database (Masson et al., 2003) necessary for the integration of the model. The surface cover type is extremely important. It is the type of landscape that is present at a certain location: sea, river, forest, town, grassland, crops, desert... The default data file contains 250 cover types. The soil type is defined by its sand and clay fractions from the FAO database. Coastlines and topography are obtained from the data base GTOPO30 whose resolution is

30 arc second (approximately 1 km). Surface data are then interpolated over the grid mesh. Given that many meteorological phenomena can be induced by topography, it means there is a need to use realistic and high-resolution fields in numerical models to represent this surface feature. The land-water mask, the soil-vegetation characteristics, and the urbanized area locations are required for the computation of surface fluxes of heat, moisture, and momentum. The most important fields deduced from the cover types are four covers: sea, inland water, town/artificial surfaces, natural/cultivated landscape. The grid mesh is partitioned into these surface features, and during a Méso-NH run, a particular surface scheme will be used for each of them. Then, the physiographic data together with information on the vertical grid and the interpolated meteorological fields from ECMWF analysis are used to start the simulation or for the boundary conditions. In the vertical, we use the Gal-Chen and Sommerville coordinate, which follows the orography. The top model level coincides with the height of the model, set here to 30 km. The vertical spacing varies, it is the strechest close to the surface. From the surface to 600-m altitude, the depth of the levels increases from 60 m to almost 100 m. Between 600 and 7000 m altitude, the depths increase from 100 m to 600 m. The rest of the levels up to the top are 600-m deep. To avoid spurious effects, a top layer is set a few kilometers lower than 30 km that serves to dampen the gravity waves originated during the simulation.

2.2.1.2 Dynamics

The dynamics of Méso-NH describe the evolution of an adiabatic laminar fluid. The two main hypothesis are non-hydrostatism and anelasticity. As the non-hydrostatic effects are not negligible at horizontal scales smaller than $\sim$10 km, the model can simulate dynamical processes within a wide range of horizontal lengths. Particularly, convective motions are explicitly allowed if the grid spacing is lower than 5 km. The vertical speed is prognostic, in contrast to hydrostatic models such as GCMs. The anelasticity in the model implies that acoustic waves are filtered out, they are too fast to be interesting for meteorology. Thus, the pressure is a diagnostic variable in Méso-NH.

In HiRes, the time step is 10 seconds. At each time step, prognostic variables are computed. Those are the three components of wind, the potential temperature (θ), the turbulence kinetic energy (TKE), the mixing ratio of water vapor and hydrometeors and the mixing ratio of passive and chemical tracers. The advection scheme employed for wind velocities is a third-order finite difference scheme based on the first Weighted Essentially Non Oscillating (WENO) scheme by Liu et al. (1994). WENO3 is an efficient advection scheme as it allows to use long time steps in the simulation but has the disadvantage of being too diffusive in the shortest wavelengths of the kinetic energy spectrum. For the scalar variables like θ, water mixing ratios and TKE, the advection scheme used is the Piecewise Parabolic Method (PPM). The volume where the simulation is performed is discretized into a C-grid of Arakawa. The scalar variables evolution is calculated on the center of each parallelepiped, the mass point. The evolution of wind components is calculated on the faces of the parallelepiped, the flux points. For instance, the wind component u is computed on the center of the face perpendicular to the x axis.

Heat exchanges, water phase transitions, subgrid processes or surface interactions are not taken into account in the dynamical core of Méso-NH and need to be parameterized.

2.2.1.3 Parameterizations

The **surface** scheme is used to simulate the physical processes related to the surface-atmosphere interaction. These processes are modeled by SURFEX, an externalized scheme that exchanges data with Méso-NH. SURFEX proposes four schemes, one for each type of surface: sea, nature, town and inland water.

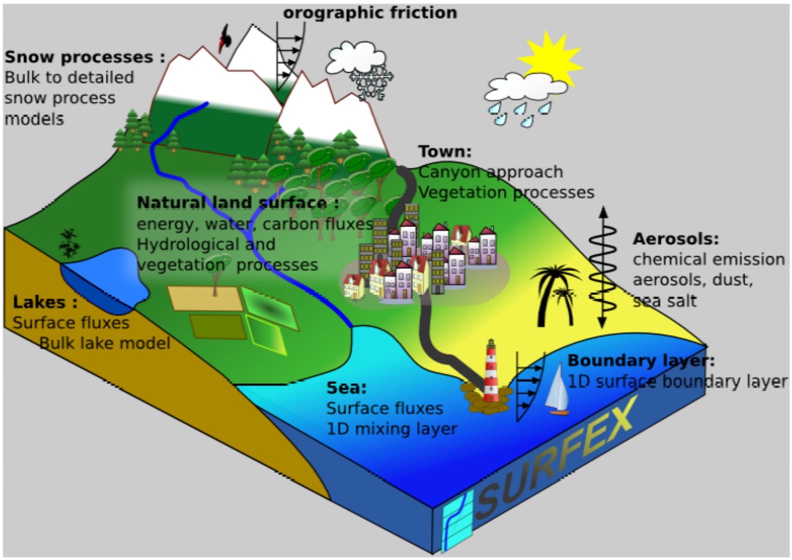

Figure 2.3: Partition of surface fluxes depending on the subgrid surface type: sea, nature, town and inland water. Reproduced from Masson et al. (2013).

The ISBA (Interaction between Soil Biosphere and Atmosphere, Noilhan and Planton, 1989) scheme is used for natural soils. Each time step, ISBA input data are the air temperature, humidity, horizontal wind speed, pressure, precipitation, radiation and concentrations of dust. It then returns to Méso-NH the momentum, moisture and heat fluxes, dust fluxes, the surface temperature, albedo and emissivity. These variables will be used by the turbulent and radiation schemes. The SURFEX fluxes are the average of the fluxes for each of the different surface types in the grid box, calculated by the corresponding surface scheme and weighted by its fraction in the grid box (Fig. 2.3). The hydrology is represented by 3 soil layers whose water content evolution is calculated by ISBA from the evaporation and precipitation.

A **turbulence** scheme serves to parameterize the energy transfers from unresolved to resolved scales. The scheme of Cuxart et al. (2000) is used in Méso-NH at any resolution. It is a 1.5-order closure scheme, meaning that the TKE is prognostic and the mixing length is diagnostic. In a Large-Eddy Simulation (LES), the scheme is 3-dimensional as the subgrid eddies are supposed isotropic. In HiRes, with a horizontal resolution of 2.5 km, all the eddies are subgrid and the turbulence scheme is 1-dimensional, meaning that only the vertical turbulent fluxes are taken into account, which is beneficial in terms of computer demand. The scheme by Bougeault and Lacarrère (1989) is used to parameterize the mixing length that represents the size of the most energetic eddies.

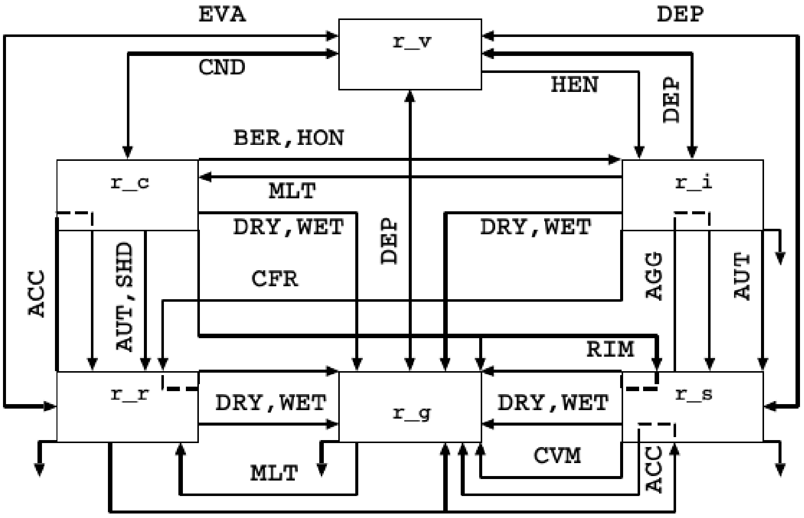

Figure 2.4: Microphysical processes represented by the ICE3 scheme. Conversion processes: EVA rain evaporation and condensation, DEP deposition and sublimation, CND cloud water condensation and evaporation, HEN heterogeneous nucleation, BER Bergeron effect, HON homogeneous nucleation, MLT melting, DRY graupel dry growth, WET graupel wet growth, ACC accretion, AUT autoconversion, SHD water loss from the surface of the graupel, CFR rain freezing by contact, AGG aggregation, RIM riming, CVM conversion of snow into graupel. Reproduced from Pinty and Jabouille (1998).

A **shallow convection** scheme is needed to represent the dry thermals and shallow cumuli within the boundary layer (BL) for horizonal resolutions coarser than 500 m to 1 km. We use the Eddy-Diffussivity Kain-Fritsch (EDKF) scheme (Pergaud et al., 2009). The computation of turbulent fluxes in the BL is made up from an eddy-diffussivity term for local mixing and a mass flux term for large eddies or plumes.

A **cloud microphysical** scheme has to describe the main processes involving water vapor and hydrometeors (liquid and solid precipitating and non-precipitating water particles). These processes are the formation, growth, decay and sedimentation of hydrometeors. A microphysical scheme is necessary in weather prediction as it allows to quantify precipitation rates at the surface. It is also needed to represent the cloud-radiation interactions. From a global perspective, a poor representation of cloud microphysics can lead to a wrong estimation of the Earth's energy budget. The absorption and release of latent heat through the water phase transitions affect the cloud dynamics. In the tropics, these diabatic processes are of utter importance, because of their strong impact at the global scale. Two assumptions are made in the microphysical schemes proposed in Méso-NH, which are usually common to other models. A bulk approach is implemented to categorize the hydrometeors. Up to 6 types of hydrometeors are possible in Méso-NH depending on the scheme: cloud droplets, raindrops, cloud ice, graupel, snow and hail. The second assumption is the saturation adjustment. A thermodynamic equilibrium is imposed, meaning that after each time step neither supersaturation nor undersaturation is allowed. If the air is supersaturated, water vapor will condense or be deposit to reach saturation. If the air is undersaturated, some hydrometeors will evaporate or sublimate.

We chose the ICE3 scheme (Pinty and Jabouille, 1998), as clouds are considered in its mixed phase state and the presence of both liquid and solid hydrometeors is concieved. This is practical for the current study as in the African domain deep convective systems developing above the 0°C isotherm are very common. In ICE3 there are represented two types of liquid hydrometeors, cloud droplets and raindrops, and three types of solid hydrometeors: cloud ice or ice crystals, graupel and snow (Fig. 2.4). Among these hydrometeor species cloud droplets and cloud ice do not precipitate and the others do. ICE3 is a one-moment scheme as only the mixing ratios of the water species are prognostic. The concentrations are diagnostic and obtained from the mixing ratios. For each water species, the size distribution can be obtained from generalized gamma laws with two tuning parameters. The mass-size and the fall speed-size relationships can be determined, each involves two coefficients that can be adjusted from ground or *in situ* measurements.

The prognostic microphysical scheme assures that after each time step the adjustment to saturation is satisfied, affecting the liquid and ice cloud amounts. This leads to a “all or nothing” method in the definition of the cloud fraction within a grid cell, that can be fully cloudy or clear sky. To avoid this crude approximation in the case of unresolved clouds a **sub-grid cloud scheme** can be implemented. We used a statistical cloud scheme by Chaboureau and Bechtold (2005). It takes into account the sub-grid variability of cloud content to which turbulence and convection contribute. This parameterization proved to decrease the bias between observed and simulated brightness temperature (BT) in the thermal infrared during a case study over southern Brazil, as radiation at this wavelength is highly interactive with cloud ice. It better captured precipitation intensities as well.

The **aerosols** processes need to be parameterized in Méso-NH. The emission processes are described in the Dust Emission And Deposition (DEAD) scheme (Zender et al., 2003). This scheme is coupled with SURFEX (Grini et al., 2006), allowing the exchange of data between Méso-NH and the DEAD scheme. Méso-NH provides DEAD with wind speed at 10-m height, soil moisture and two roughness lengths, one that corresponds to a perfectly erodible soil, and the other that corresponds to non-erodible surfaces. These input data are evaluated by ISBA. DEAD provides Méso-NH with the dust flux computed every time step. Dust is mobilized following Marticorena and Bergametti (1995) from a combination of saltation and sandblasting processes (Fig. 2.5).

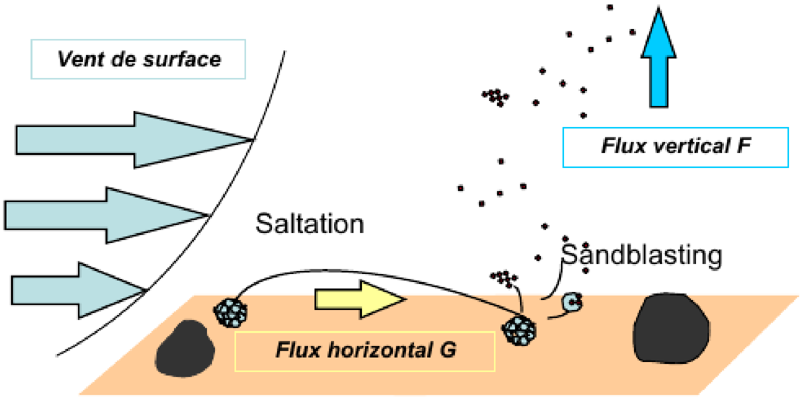

Figure 2.5: Saltation and sandblasting are the two main processes leading to dust emission in favorable surface wind speed conditions. Reproduced from Laurent (2005).

From those input data, a horizontal flux of dust particles can be computed. The vertical flux of dust aerosols that will be injected into the atmosphere is calculated as the ratio of the horizontal flux and a sandblasting efficiency coefficient, that depends on the content of clay in the soil. The dust aerosols that reach the atmosphere are ready to be transported. The life cycle of dust once in the atmosphere is simulated in the ORganic and Inorganic Log-normal Aerosols Model (ORILAM) scheme (Tulet et al., 2005). ORILAM considers three dust modes, with a log-normal size distribution. The size distributions have median diameters of 0.078, 0.64 and 5.0 μm and standard deviations of 1.75, 1.76 and 1.70, respectively, as defined by Crumeyrolle et al. (2011). The scheme simulates the time and space evolution of the distribution. Three moments of the distribution can be computed, although in HiRes only one moment is explicit. Dust in the atmosphere can undergo dry sedimentation and wet deposition that return it to the surface. Sedimentation processes are due to the gravity force and large particles have larger sedimentation velocity. The wet deposition or scavenging by precipitating systems assumes dust to be soluble by a factor of 0.3 in precipitable water.

Radiative transfer in the atmosphere is represented in the simulation through the **radiation** scheme of the ECMWF operational model, which is coupled with Méso-NH. The code computes the net total radiative heat flux in each atmospheric column and provides the user with the potential temperature tendency. The flux is calculated as a sum of upward and downward fluxes, comprising the solar or shortwave radiation and the atmospheric or longwave radiation. The solar radiation can be reflected, scattered and absorbed by the gases, aerosols and clouds. All these processes are represented in the scheme by Fouquart and Bonnel (1986) that we used here, that considers 6 spectral bands. The longwave radiation is emitted by the Earth's surface and clouds, both grey bodies, at a frequency close to the infrared spectrum. The Rapid Radiative Transfer Model (RRTM) by Mlawer et al. (1997) is used here for longwave radiation, and accounts for 16 spectral bands. Dust aerosols both scatter and absorb solar radiation, and they absorb and re-emit terrestrial radiation. The radiation scheme in the shortwave region is affected by dust and clouds. The refractive indexes of mineral dust were taken from Tulet et al. (2008), i.e. 1.448-0.00292i at 532 nm, 1.44023-0.00116i at 730 and 820 nm and 1.41163-0.00106i at 1064 nm. For the absorption and re-emission of longwave radiation by dust, only a constant fraction of the 550-nm AOD (Aerosol Optical Depth) is considered. The longwave effect of dust is much smaller than the shortwave effect, but it is not negligible during nighttime in the absence of solar radiation.

As the radiation scheme is very time-expensive it is usually not called at each time step. But a too coarse time step for the radiation scheme would not be appropriate as, for instance, the cloud fraction varies quickly and has a large effect on radiation. Thus, while the Δt of the simulation was set to 10 s, the radiation scheme is refreshed every 15 minutes.

2.2.2 The LowRes simulation

The LowRes simulation was performed in order to analyze the effects of the resolution and representation of convection on precipitation. An horizontal resolution of 20 km was chosen which led to a broader time step of 60 s. Otherwise, the dynamics were unchanged and all the physical paremeterizations are the same than in HiRes. As a result of the change in grid spacing deep convection however needs to be parameterized in LowRes. The convective parameterization accounts for the subgrid release of latent heat and mass transport due to deep convective clouds, which affect the dynamics and thermodynamics of the atmosphere.

We used here the convective scheme by Bechtold et al. (2001). The latter calculates tendencies for temperature and moisture consistent with the effects of deep convection under larger-scale conditions that allow the development and maintenance of convection. Based on the Kain-Fritsch mass flux scheme (Kain and Fritsch, 1989), the parameterization brings the atmosphere to an adjusted state through mass exchange between the cloud and the environment. This exchange occurs through entrainment and detrainment, where the cloud is described as a one-dimensional convective plume consisting of an updraft and a downdraft.

The main levels of the cloud model are shown in Fig. 2.6. They are: DPL departure level, LCL lifting condensation level, LFC level of free convection, ETL equilibrium temperature level, CTL cloud-top level, LFS level of free sink, DDL downdraft detrainment level, DBL downdraft base level. Both the DPL and DBL are not necessarily equal to the surface level. From the surface, a mixed air parcel consisting of a 60-hPa deep layer is lifted without entrainment to its LCL where the stability of the parcel is evaluated. If the air parcel is stable with respect to moist convection, a new air parcel will be lifted from the next higher 60-hPa mixed layer, the new DPL. An updraft is generated at the DPL where it entrains environmental air and then it ascends up to the LCL. The updraft mass flux, the updraft values of the conserved variables, of precipitation and vertical velocity w^u are computed at each vertical level of the grid. The CTL is defined as the level where $(w^u)^2$ becomes negative, and the mass flux decreases linearly between the ETL and the CTL. The melting and evaporation of precipitation is at the origin of the downdraft, that extends from the LFS to the DBL. Downdraught detrainment is allowed only in the 60-hPa DDL-DBL. Finally, within an adjustment period τ all the CAPE must be consumed in a grid cell.

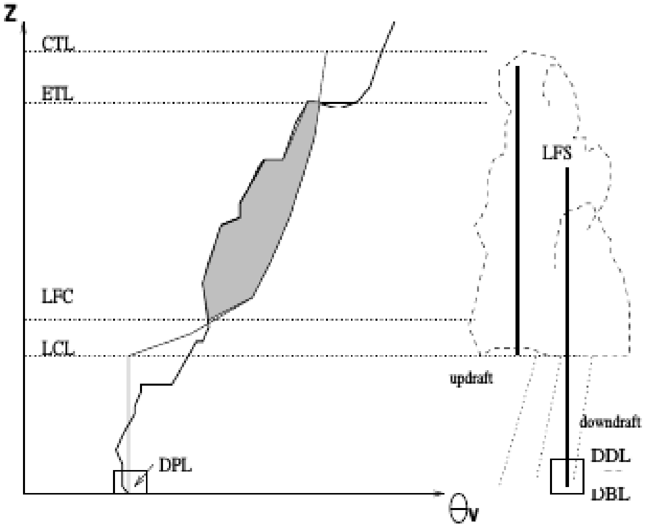

Figure 2.6: Environmental (thick solid line) and parcel sounding (thin solid line) of θ_v in a deep convective cloud. The convective available energy (CAPE) corresponds to the shaded area. The different key cloud levels are: DPL departure level, LCL lifting condensation level, LFC level of free convection, ETL equilibrium temperature level, CTL cloud-top level, LFS level of free sink, DDL downdraft detrainment level, DBL downdraft base level. The updraft and downdraft regions are illustrated by the vertical solid lines. Reproduced from Bechtold et al. (2001).

2.2.3 The HiNod simulation

The HiNod simulation is run with the aim of studying the sensitivity of the atmosphere to the radiative effect of dust. HiNod was performed with the same configuration and parameterizations than HiRes. The dust emissions are simulated in HiNod as well as their transport, except that the radiative feedback of the dust on the temperature field is turned off in both the shortwave and longwave regions of the spectrum.

2.3 Observations

To assess clouds, precipitation and dust in the simulations, products derived from satellite observations and measurements from AERONET ground-based Sun photometers are employed.

Clouds are usually assessed from satellite-derived brightness temperatures (BTs). The BT is the temperature that a black body would have to replicate the radiance of an object (grey body) at a given wavelength. The upward radiation from the top of the atmosphere is received by the satellite-onboard radiometers, then BT is derived from the measured radiance of objects such as clouds. The observational BT product is made from merged infrared (IR) BT data from all available gesostationary satellites into a global (in longitude) data set, with 60°S - 60°N coverage (Janowiak et al., 2001). The data were taken from a single IR channel for each of the five different available satellites, between 10.7 and 11.5 μm. Over Africa, the BT data in June 2006 was obtained from the 10.8 μm channel of the Spinning Enhanced Visible and InfraRed Imager (SEVIRI) radiometer aboard the Meteosat Second Generation (MSG) platform. In the IR channel, the satellite senses the thermal radiation emitted by the earth's surface or clouds. In presence of opaque clouds, these channels are mainly sensitive to the temperature at the cloud top. The merged product, from the Climate Prediction Center (CPC), has a resolution of $\sim$4 km and 30-min in space and time, respectively. It is advantageous for cloud monitoring because it provides a high-resolution sampling, both during day and night. The product is used to assess the synthetic BTs at 10.8 μm that are obtained for the three simulations, from the Radiative Transfer for Tiros Operational Vertical Sounder (RTTOV), code version 8.7 (Saunders et al., 2005).

The very sparse rain gauge network in Africa makes precipitation estimates from satellite retrievals highly valuable there. The Tropical Rainfall Measuring Mission (TRMM) product 3B42 (Huffman et al., 2007) version 7 (V7) is used in this thesis to evaluate the simulated precipitation. This product primarily relies on passive microwave data from a variety of satellites and IR data collected from geostationary satellites. For the 9-14 June 2006 period examined here, the product 3B42 took advantage of the merged IR data described for the simulated BT evaluation. A limitation of IR-based precipitation estimates is that BT mainly corresponds to cloud top heights, but not necessarily to rainfall. Arkin and Meisner (1987) showed that the precipitation estimates from IR data are acceptable at temporal and spatial scales larger than 1 day and $2.5^\circ\times2.5^\circ$, respectively. These conditions are satisfied in our case study. The product 3B42 V7 provides hourly precipitation rates, and covers 50°S - 50°N with horizontal and temporal resolutions of $0.25^\circ\times0.25^\circ$ and 3 hours, respectively. Such a temporal sampling is convenient for the analysis of the diurnal cycle of precipitation at regional and global scales, which makes the TRMM product 3B42 widely employed (e.g., Collier and Bowman, 2004; Sato et al., 2009; Zhang et al., 2016).

For the dust assessment we use the aerosol optical depth (AOD) and backscatter coefficient from satellite retrievals, and the AOD and Ångström coefficient from AERONET. The AOD is provided by the Deep Blue collection, from retrievals of the Moderate Resolution Imaging Spectroradiometer (MODIS) (Hsu et al., 2004) onboard Aqua spacecraft. Aqua passes from south to north across the Equator at around 1330 local time. The AOD is based on observations in the visible range of the radiation spectrum, from wavelengths between 412 and 670 nm, and from the ultraviolet. The main asset of the Deep Blue algorithm is that it estimates AOD over bright surfaces, notably deserts, where dust emission and concentration are large. The daily MODIS AODs used for assessment here are provided on a $1^\circ \times 1^\circ$ regular latitude-longitude grid, although they are computed from rough AOD at 10-km spatial resolution.

While MODIS allows a high spatial coverage, AERONET Sun photometers (Holben et al., 1998) provide retrievals of AOD and other aerosol properties with an excellent time resolution of 15 minutes during daytime. We used here the AOD product at 440 nm, and the the Ångström coefficient obtained from 440 and 870 nm wavelengths from the four stations of Cinzana, Ouagadougou, Banizoumbou and Tamanrasset. The AERONET measurements allow the aerosol characterization and also serve for satellite products validation. AODs derived from AERONET Sun photometers are more accurate than from MODIS, as the photometers measure directly the radiation attenuation by the atmospheric aerosols, whereas the space-borne radiometer receives as well a signal from the surface. Unfortunately, the AERONET coverage in northern Africa, and particularly the Sahara desert remains sparse during the period of study. The use of both MODIS Deep Blue and AERONET for dust assessment is convenient, as they offer the regional distribution of AOD in northern Africa with satisfactory measurements over bright arid regions, and a high-frequency local measurements during daytime, respectively. Note, however, that both AOD products are designed to sample all types of aerosols, in contrast with the AOD computed in the Méso-NH model, which is due exclusively to dust.

To further assess the distribution of dust in the vertical, backscatter coefficients at 532 nm from CALIOP onboard CALIPSO are employed (Winker et al., 2009). The lidar provides observations during both day and night. It presents a very high sampling resolution, 30 and 335 m in the vertical and in the horizontal, respectively, but a poor temporal sampling of the same areas, with an overpass every 16 days and a very narrow swath. The CALIOP-derived product used here was released on 13 June 2006, and only comparisons after that day are possible. The simulated backscatter coefficients to be directly compared against the observed signal are computed in HiRes with a lidar simulator integrated in the model (Chaboureau et al., 2011). This virtual lidar takes into account all the scattering particles of the model, such as cloud droplets, ice crystals and aerosols.

2.4 MCS tracking

The most frequently employed automatic method for the detection of convective systems is based on satellite-derived IR images. IR imagery is advantageous in that daytime and nighttime coverage is available allowing the full tracking of the cloud systems. Two criteria are generally applied on the images: a threshold on BT and a threshold on the minimum surface occupied by the system. BTs are usually used to indicate the height of the clouds coldest tops. But low BT values do not necessarily correspond to deep convective clouds but rather cold high cirrus clouds (Duvel, 1989). The use of IR images from geostationary satellites is very practical as they allow a high temporal resolution sampling.

Once the convective systems have been detected, a tracking technique through geographical overlapping of the convective systems has been extensively used (e.g., Maddox, 1980; Mathon et al., 2002; Fink et al., 2006). For instance, Mathon et al. (2002) define MCSs from a BT threshold of 233 K and a surface larger than 5000 km^{-1}. The method relies on the hypothesis that the convective systems observed in a sequence of IR images propagate sufficiently slow to have the certainty that the systems detected in two successive images that overlap each other are the same system.

Approach used in this work

The cloud systems are detected from BT from the CPC merged IR dataset (Janowiak et al., 2001) and the three Méso-NH simulations, by applying a threshold on BT at 20 km for all the data sets, observed and simulated, despite their original horizontal resolution. This common mesh of 20 km is imposed for the cloud identification because a sensitivity of the cloud size distribution to the resolution of the data sets is revealed. Two cloud categories are established: Deep Convective Clouds (DCCs) and Cirrus Anvil Clouds (CACs). For the MSG data set, DCCs are identified from BT lower than 230 K. This threshold corresponds to an altitude of around 12 km. Thus, DCCs that present cloud-top temperatures lower than 230 K have a vertical extent of more than 12 km. CACs are identified from grid points whose BT ranges between 230 and 260 K. These thresholds are common to other studies (e.g., Duvel, 1989; Söhne et al., 2008). In the simulations, low BT values are generally more frequent than for MSG. Therefore, to ensure that each cloud category is equally represented in terms of total cloud cover among the data sets, the thresholds vary for the simulations. The BT thresholds are 243 and 266 K for HiRes and HiNod, and 246 and 264 K for LowRes (Fig. 2.7).

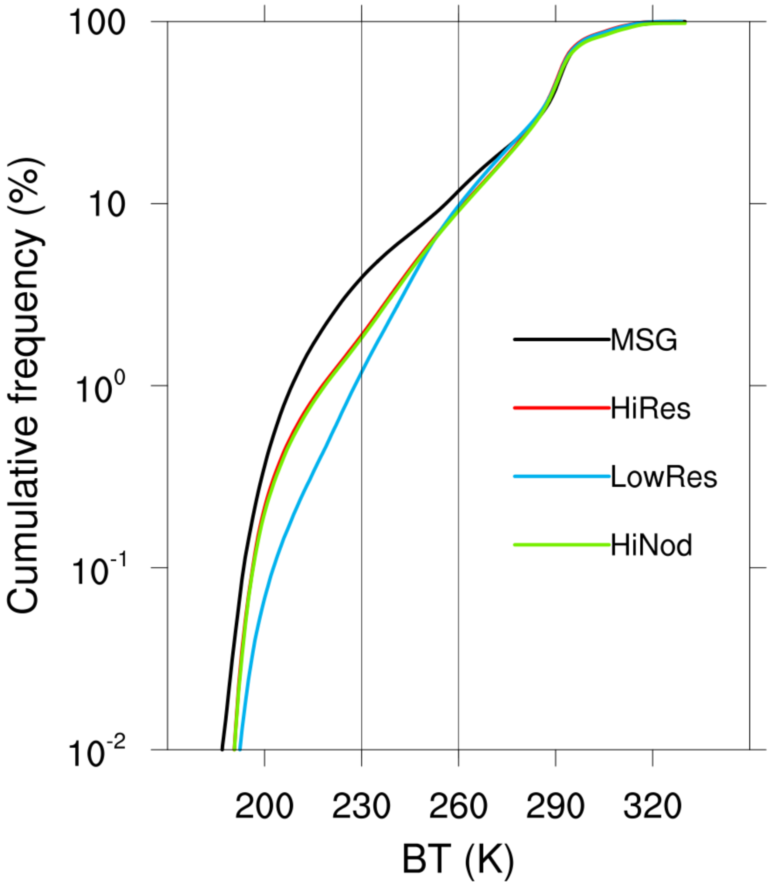

Figure 2.7: Cumulative distribution function of BT on a 20-km grid mesh for MSG and the three simulations.

A clustering algorithm is then applied to the grid points identified as DCC or CAC. For each cloud category, a cluster is built from contiguous grid points that share one face in the horizontal. Until now, no threshold has been imposed on the size of the clusters. DCCs and CACs can be single grid points with the minimum possible surface of 20×20 km^2.

Once DCC and CAC clusters have been identified, the second step is to associate precipitation to each cloud cluster. For the observational cloud clusters, precipitation comes from TRMM product 3B42 for hourly rain rates at the ground. The product has temporal and horizontal resolutions of 3 h and 0.25°, respectively. The TRMM grid was then adapted to the common 20-km mesh of the BT data, and three-hourly accumulated precipitation was computed and attributed to the MSG clusters. For the simulated clusters, we associate the precipitation accumulated between 2 outputs, i.e., during 3 hours of simulation. Note that the precipitation associated with a cloud cluster from MSG at 03 UTC corresponds to the accumulated precipitation during one hour and a half before and later. Whereas in the case of the simulations, it corresponds to the accumulated precipitation during the previous three hours.

The daily amounts of precipitation of less than 0.2 mm are excluded from all the precipitation data sets for being considered a trace (WMO, 2014), meaning that the value of 0.2 mm day^{-1} lies within the error associated with the instruments precision. The part of total precipitation considered after discarding those trace values is still comprised between 99.4% and 99.7% for TRMM and the simulations.

The tracking, based on geographical overlapping, is done at 3-h resolution as imposed by the TRMM data. Machado et al. (1998) suggest to apply the tracking exclusively to cloud clusters whose surface is larger than 10000 km^2 if the satellite images are only available every 3 h. Otherwise, they consider the tracking not to be satisfactory. Because the temporal resolution of our data sets is 3 h, this consideration is followed and the tracking is applied to DCC clusters that have an effective diameter larger than 120 km, that corresponds to the diameter of a circle whose surface is 10000 km^2. These DCCs satisfying the condition of the effective diameter are called MCSs, the others small DCCs. Thus, the tracking is performed on MCSs. Short-lived MCSs are MCSs with a lifetime of less than 6 h, and long-lived MCSs are those whose lifetime is at least 6 h. Note that the 3-h resolution does not allow a full description of the lifecycle of a MCS, and the triggering and lysis of the MCS may not be detected. The surface overlapping ratio required is set to 20%. This means that between two successive BT images, if a MCS cluster at $t{+}3h$ is covering at least 20% of the surface occupied by a MCS cluster at t, they are the same MCS. It could happen that the MCS cluster at $t{+}3h$ satisfies this rule with several clusters at t (merging). It will then be associated with the cluster at t with which the overlapping area is the largest. Finally, if this value of maximum overlapping area is shared with several clusters, the choice of the MCS at t is random. The case of a single MCS cluster at t splitting into more than one MCS cluster is equally treated. More sophisticated tracking algorithms may alleviate the artificial merging and splitting of the MCS (Fiolleau and Roca, 2013), but the aim here is to employ a method easy to implement and convenient to be used in the same manner on both the observations and simulations.

Furthermore, vertical profiles of thermodynamic and dynamic variables are also attributed to MCSs, to characterize them during their lifecycle. For the observational data set, the profiles were computed from the European Center for Medium-Range Weather Forecasts (ECMWF) analysis at 00, 06, 12 and 18 UTC; and from the 3-h forecasts at 03, 09, 15 and 21 UTC. The profiles are calculated on the volume yielded by the cluster envelope when projected on the vertical.

An example of the tracking technique applied on a 24-h duration MCS propagating from northwest Nigeria to Ivory Coast between the 13 and 14 June 2006 is shown in Fig. 2.8. This long-lived MCS is the one examined in Flamant et al. (2009). The 3-h effective diameter ranges between 250 and 450 km and its mean 3-h accumulated precipitation (from TRMM) takes values between 400 and 800 mm h^{-1} (Fig. 2.9). The vertical profile of the horizontal wind speed (from ECMWF) is computed in the volume associated with the individual clusters during the MCS lifetime. The largest wind speeds, larger than 12 m s^{-1}, are found at mid-level altitudes.

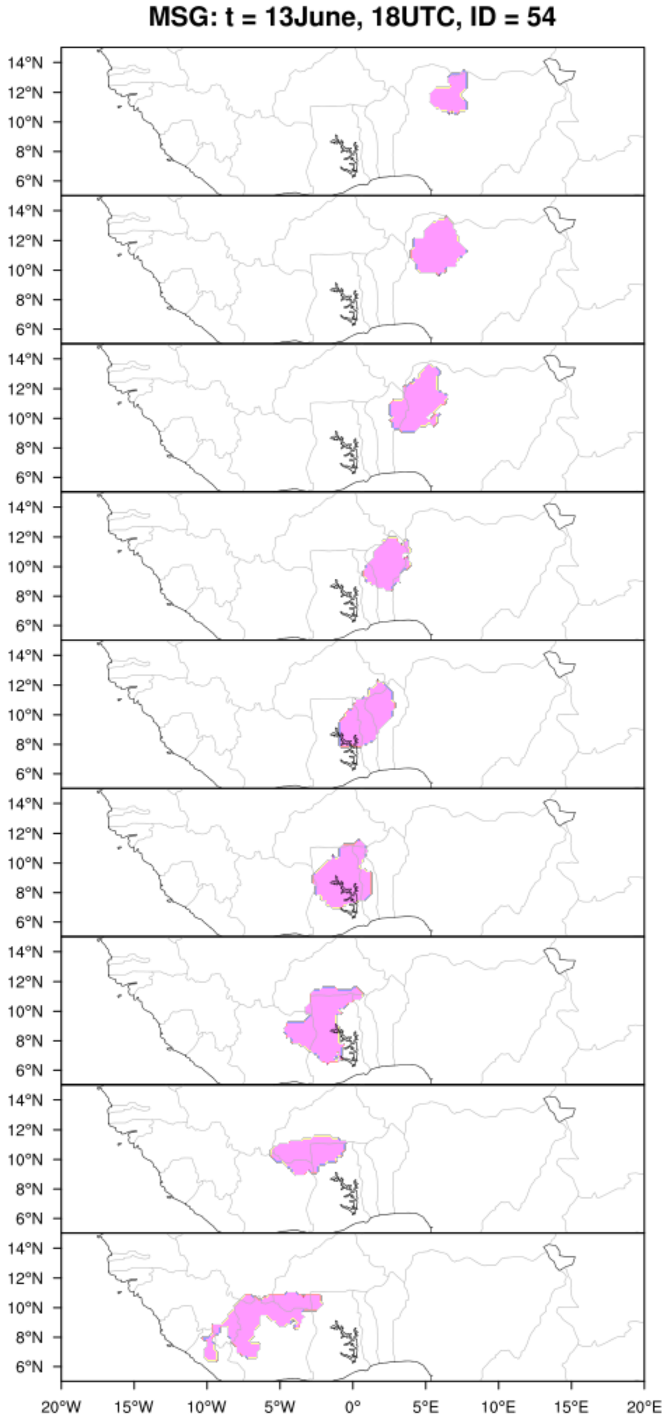

Figure 2.8: Successsion of the images corresponding to the clusters of the MCS from MSG (DCC with an effective diameter larger than 120 km) every 3 hours between 13 June at 18 UTC and the next day at 18 UTC. The trace of the MCS precipitation is visible in the Hovmöller diagram in Fig. 2.1.

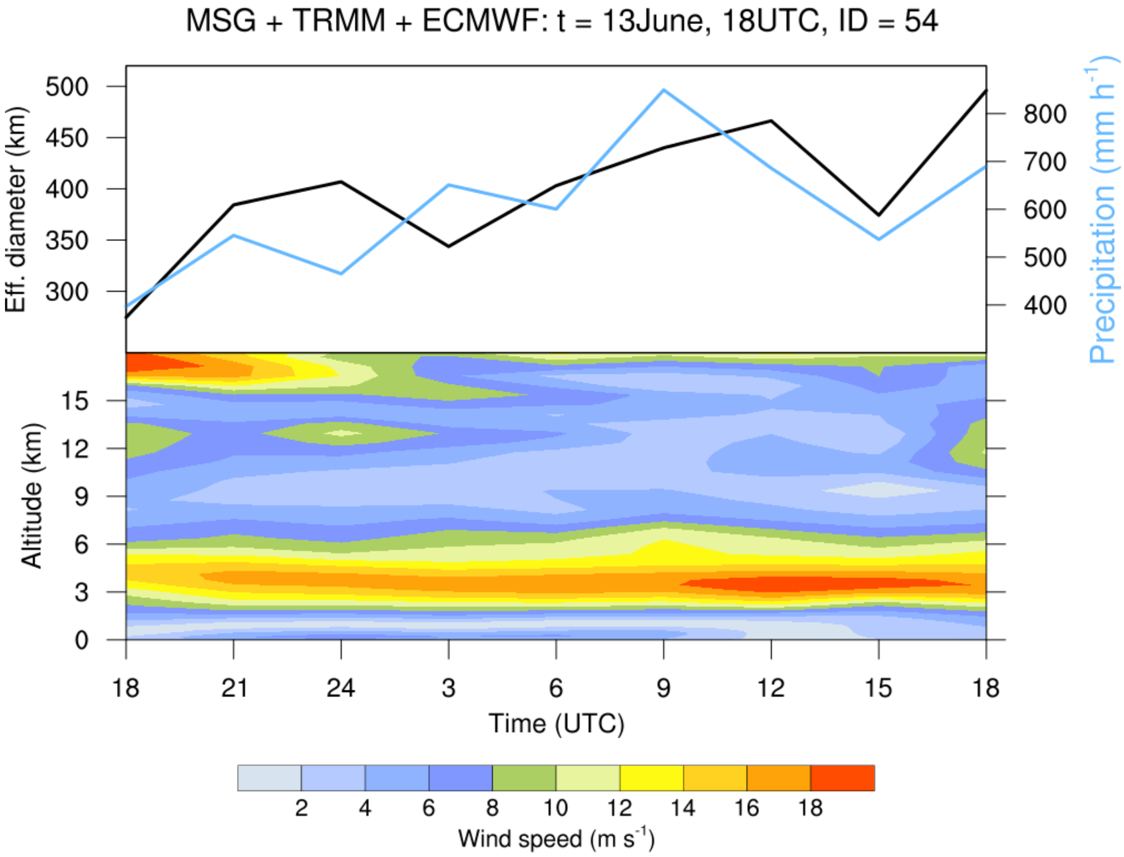

Figure 2.9: Time evolution of the effective diameter and mean accumulated precipitation (top), and of the vertical profile of the mean horizontal wind speed within the cluster (bottom) for the long-lived MCS in Fig. 2.8

Chapter 3

The Westward Increase of Deep Convection Organization in Northern Africa

Contents

3.1 Introduction

In this chapter, the precipitating systems controlling the distribution of precipitation and its variability over northern Africa are investigated during the dust outbreak of 9-14 June 2006. Satellite observations and two Méso-NH simulations, one convection-permitting and the other with parameterized convection, are employed to examine the cloud systems contributing to precipitation. In particular, the sensitivity of the precipitating systems to the resolution and the representation of convection in the model is addressed. The same methodology is applied to both the observations and simulations. The cloud systems are identified as deep convective clouds (DCCs), cirrus anvil clouds (CACs) or other clouds from their brightness temperature (BT), and each of them is attributed precipitation. Different BT thresholds are established for each cloud category. Mesoscale convective systems (MCSs), i.e., DCCs with an effective diameter larger than 120 km are tracked. Long-lived MCSs, i.e., those with a lifetime of at least 6 hours, are characterized in terms of their size, lifetime, speed and thermodynamic variables, with the aim of analyzing the degree of organization of the long-lived MCSs. The latter are analyzed in three sub-regions, which are characterized by distinct environmental conditions. From east to west, they are: Ethiopia (ETH), Central Africa (CAF) and southern West Africa (SWA).

Precipitation is observed along a zonal band from 0° to 15°N. DCCs generate 71% of total precipitation. Among them, long-lived MCSs are the greatest precipitation makers, responsible for 55% of precipitation. They contribute the most to the diurnal cycle of precipitation, that peaks at 2100 LST. The long-lived MCSs are the largest, longest-lived and fastest in SWA, indicating that their degree of organization is higher there than in CAF or ETH. These MCSs become more organized as they propagate westward, guided by the African easterly jet (AEJ).

Indeed, the AEJ and the monsoon flow, which strengthen from ETH to SWA, are some essential ingredients for the long-lived MCSs organization. So are the wind shear and the low-level moisture that increase from east to west. The conditional instability is also the largest over SWA. The convection-permitting simulations achieves to distribute precipitation correctly among the different types of precipitating systems. Long-lived MCSs produce 50% of total precipitation and contribute the most to its diurnal cycle, as observed, but lack precipitation over SWA. This is explained because the simulated long-lived MCSs are smaller and shorter-lived than observed, despite the westward increase in both the wind shear and the conditional instability. The long-lived MCSs over SWA wrongly propagate with a slight northward component, which contrasts with the observed southwestward propagation. The poor representation of the degree of organization and propagation of the long-lived MCSs over SWA needs further investigation. The simulation with parameterized convection fails to distribute precipitation correctly. This shows the added value provided by the convection-permitting resolution in realistically representing the precipitating systems.

These results are presented in the article reproduced in section 4.2, published in *Monthly Weather Review*.

3.2 Article

Precipitation and Mesoscale Convective Systems: Explicit versus Parameterized Convection over Northern Africa

IRENE REINARES MARTÍNEZ AND JEAN-PIERRE CHABOUREAU

Laboratoire d'Aérologie, Université de Toulouse, CNRS, UPS, Toulouse, France

(Manuscript received 13 July 2017, in final form 9 January 2018)

ABSTRACT

Precipitating systems are analyzed during a dust event from 9 to 14 June 2006 over northern Africa. A common analysis is applied to satellite observations and two Meso-NH simulations: one convection permitting (grid spacing $\Delta x = 2.5\,\mathrm{km}$) and the other with parameterized convection ($\Delta x = 20\,\mathrm{km}$). The precipitating systems are identified as cloud objects and classified as deep convective clouds (DCCs) or other clouds according to their infrared signature. Large DCCs [hereafter named mesoscale convective systems (MCSs)] are tracked, characterized in terms of precipitation and thermodynamic profiles, and analyzed in southern West Africa (SWA), central Africa, and Ethiopia. Precipitation is mostly observed along 0°–15°N, with 71% of the total precipitation produced by all DCCs and 55% by long-lived MCSs. It shows a marked diurnal cycle with a peak in the evening, mainly due to long-lived MCSs, which are characterized by an increase in size, zonal speed, and duration from east to west, with the largest, fastest, and longest-lived ones found over SWA. This is due to an enhanced African easterly jet (AEJ) and monsoon flow leading to stronger shear and greater conditional instability. The simulation with parameterized convection fails to distribute precipitation correctly. The convection-permitting simulation captures most of the observed precipitation features, but lacks the increase in organization of the long-lived MCSs over SWA. Excess moisture in a too zonal AEJ flow suggests that the long-lived MCSs in SWA are poorly located with respect to African easterly waves. The convection-permitting model improves the representation of precipitation but without fully resolving the long-lived MCSs.

1. Introduction

Precipitation over northern tropical Africa occurs mainly during the monsoon season. The summer rainfall can account for up to 95% of the total annual amount (e.g., in the Ethiopian Highlands; Segele and Lamb 2005). Most of the precipitation arises from moist convective instability (Bayo Omotosho 1985; Janiga and Thorncroft 2014), in the form of local thunderstorms or more organized systems such as mesoscale convective systems (MCSs). Precipitating systems start as individual convective cells triggered by the daytime boundary layer development, convergence lines, or other processes, preferentially in the lee of high terrain (Laing et al. 2008; Söhne et al. 2008). Their further growth into MCS is favored by midlevel dry air and the vertical wind shear associated with the African easterly jet (AEJ) (Laing et al. 2008; Janiga and Thorncroft 2014), a seasonal midlevel jet that results from the meridional temperature gradient between the Gulf of Guinea and the Sahara. Precipitation is significantly modulated by African easterly waves (AEWs) (Mathon et al. 2002; Fink and Reiner 2003; Laing et al. 2008), synoptic-scale disturbances of the AEJ having periods of 3–5 days and wavelengths of 2000–3000 km, with which the MCSs interact.

Precipitation over tropical Africa exhibits a marked diurnal cycle. In the first order, this is driven by solar heating. The morning increase of surface heat fluxes leads to the convective growth of the boundary layer, the moisture content of which is enriched by the monsoon flow. This leads to the generation of precipitating systems, usually in the afternoon, which is often followed by a westward propagation, primarily driven by the AEJ (Zhang et al. 2016). Over eastern Africa, convection is most commonly triggered in the afternoon along the western slopes of the Ethiopian Highlands (Laing et al. 2008). Over West Africa, most regions show a single diurnal peak of precipitation (Zhang et al. 2016). Afternoon peaks are generally associated with topographic features such as the Jos Plateau, and nocturnal peaks are due to precipitating systems downstream of high terrain

---

Corresponding author: Dr. Irene Reinares Martínez, irene.reinares@aero.obs-mip.fr

DOI: 10.1175/MWR-D-17-0202.1

(e.g., over Niamey and the northeastern part of Benin; e.g., Janiga and Thorncroft 2014; Zhang et al. 2016).

The contribution of MCSs to the total rainfall has been attributed to specific areas so far. Over southwest Niger, in the semiarid Niamey area (13°N, 2°E), their contribution has been estimated to be 90% (Mathon et al. 2002). Over Benin, in the semihumid Parakou area (9°N, 2°E), MCSs contribute to 50% (Fink et al. 2006). Over Nigeria, their contribution varies from 70% at 12°N down to 20% along the Guinean coast (Bayo Omotosho 1985). This southward decrease in contribution to precipitation has been explained by a decrease in the organization of MCSs (e.g., Bayo Omotosho 1985; Fink et al. 2006). The contribution of MCSs to rainfall over other regions, particularly over eastern tropical Africa, remains unknown, as does their contribution to the diurnal cycle of precipitation.

The aim of this paper is to examine the precipitating systems over northern Africa, particularly the characteristics and organization of MCSs. A combined analysis of MCSs and their dynamical and thermodynamical properties is attempted. It is impossible to guarantee the consistency between the cloud systems identified from satellite observations and the properties matched to them, taken from the European Centre for Medium-Range Weather Forecasts (ECMWF) operational analyses (which do not provide us with hydrometeor contents). Therefore, two simulations were run with the nonhydrostatic mesoscale atmospheric Meso-NH model (Lafore et al. 1998): one convection-permitting and the other with parameterized convection and different horizontal resolution. The difference in the simulation setup was not motivated by the desire to separate the effect of resolution and the effect of the representation of convection. The intention was rather to contrast two simulations: one typical of regional climate models and the other representative of convection-permitting models.

A rain-attribution methodology that associates rainfall with MCSs has been applied here to both satellite observations and simulations in the same way. In addition, profiles of thermodynamic quantities are determined for each MCS. The objectives are threefold: first, to give a comprehensive view of the sources of precipitation over northern tropical Africa; second, to show the performance of the Meso-NH model for each simulation, assessing, in particular, the ability of the simulations to reproduce the mechanisms controlling rain; and third, to analyze the properties of the MCSs and their degree of organization.

Rain has commonly been attributed to MCS by combining infrared imagery and rainfall information from rain gauges (e.g., Mathon et al. 2002; Fink et al. 2006) or from satellite observations, (e.g., Futyan and Del Genio 2007; Goyens et al. 2012). In the present study, deep convective clouds (DCCs) are identified by individual pixels with infrared brightness temperatures (BTs) lower than an arbitrary threshold. Contiguous DCCs are then clustered. Depending on their size, some DCC clusters are categorized as MCSs (and tracked in time) or as other convective systems. Rainfall information from satellite retrievals is matched with the DCC clusters, which enables the contribution of MCSs to precipitation to be estimated.

Our methodology is applied to the period from 9 to 14 June 2006, during a well-documented, intense dust outbreak (Flamant et al. 2009; Lemaître et al. 2010; Crumeyrolle et al. 2011). As shown in the following, the case of this relatively short, rainy period was selected because of the presence of propagating MCSs. Moreover, the presence of dust may modulate the AEJ through its direct radiative effect (e.g., Tompkins et al. 2005; Chaboureau et al. 2007). The radiative impact of dust on the MCS distribution over northern tropical Africa is, as yet, unstudied; however, it will be the subject of a companion paper. Here, our focus is on the characteristics of the precipitation distribution.

The article is structured as follows. The model and data, and the rain-attribution approach are described in sections 2 and 3, respectively. The overall distribution of clouds and precipitation and the diurnal cycle of precipitation are presented in section 4, where we show that MCSs contribute the most to precipitation. The propagation properties of MCSs and the environmental conditions in which they propagate are examined in section 5. The conclusions and some suggestions for further work are given in section 6.

2. Model and data

Two simulations are run using the anelastic, nonhydrostatic regional model Meso-NH (Lafore et al. 1998), version 5-1-3, over a domain of 3840 × 7680 km^2 (Fig. 1). Such a large domain over northern Africa allows both the AEWs propagation and the dust emissions in Chad and Sudan (Flamant et al. 2009) to be fully described. A regional run with a 20-km horizontal grid spacing (hereafter LowRes) is compared with a cloud-resolving run with a 2.5-km horizontal grid spacing (hereafter HiRes). Both runs use 72 vertical levels up to a height of 30 km, with vertical grid spacing between 60 and 600 m. HiRes uses about a third of a billion grid points, which is made possible by the large parallel computing capability of Meso-NH (Pantillon et al. 2011). The two simulations are run for the 6-day period from 0000 UTC 9 June to 0000 UTC 15 June 2006. The initial and boundary conditions are provided by the

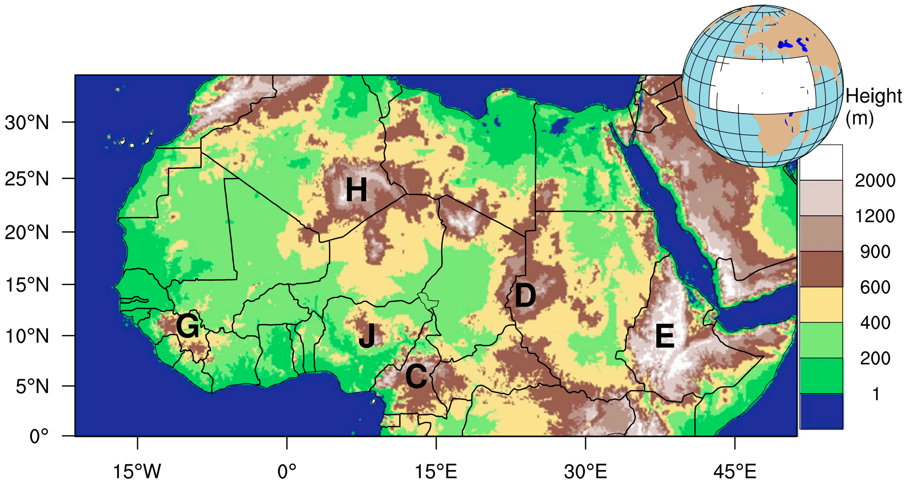

FIG. 1. Domain of simulation and analysis, with altitude color shaded. Topographic features are the Guinea Highlands (G), the Hoggar Mountains (H), the Jos Plateau (J), the Cameroon Highlands (C), the Darfur Plateau (D), and the Ethiopian Highlands (E).

ECMWF operational analysis. Model variables are output every 3 h.

Both runs use the Surface Externalisée (SURFEX) scheme for surface fluxes (Masson et al. 2013), a 1.5-order closure scheme for turbulence (Cuxart et al. 2000), and a parameterization of dry thermals and shallow cumuli (Pergaud et al. 2009). They further include a microphysical scheme for mixed-phase clouds (Pinty and Jabouille 1998), a subgrid statistical cloud scheme (Chaboureau and Bechtold 2005), and a dust prognostic scheme (Grini et al. 2006) to allow online interaction with radiation (the indirect effects of dust, i.e., the role of dust as cloud condensation nuclei or ice nuclei, are not considered here). The radiative scheme employed is the Rapid Radiative Transfer Model (Mlawer et al. 1997) for longwave radiation and the two-stream scheme (Fouquart and Bonnel 1986) for shortwave radiation. A subgrid deep convection scheme (Bechtold et al. 2001) is activated for LowRes while no deep convection parameterization is used for HiRes.

The capability of the Meso-NH simulations to capture the atmospheric dynamics is assessed by examining their kinetic energy spectrum following Skamarock (2004). Spectra of vertical velocities for HiRes and LowRes are computed at the end of the simulation (0000 UTC 15 June 2006), across the full domain and averaged between 3 and 9 km of altitude (Fig. 2). For the large scales, with wavelengths longer than 500 km corresponding to synoptic motions, both spectra show a wavenumber dependence of κ^{-3}, while they exhibit a $\kappa^{-5/3}$ dependence in the mesoscale. They both depart from the observational slope, but at different wavelengths: 200 km for LowRes against 20 km for HiRes. This is due to too large a removal of energy, which produces an energy removal grid-scale dependency. Each wavelength thus defines the effective resolution of each simulation (Skamarock 2004). This shows the added value offered by HiRes in resolving kinetic energy at convective scales.

Cloud systems are defined in terms of BT at 10.8 μm and 3-hourly accumulated precipitation is associated with them. From the model outputs, synthetic BTs corresponding to the Meteosat Second Generation (MSG)

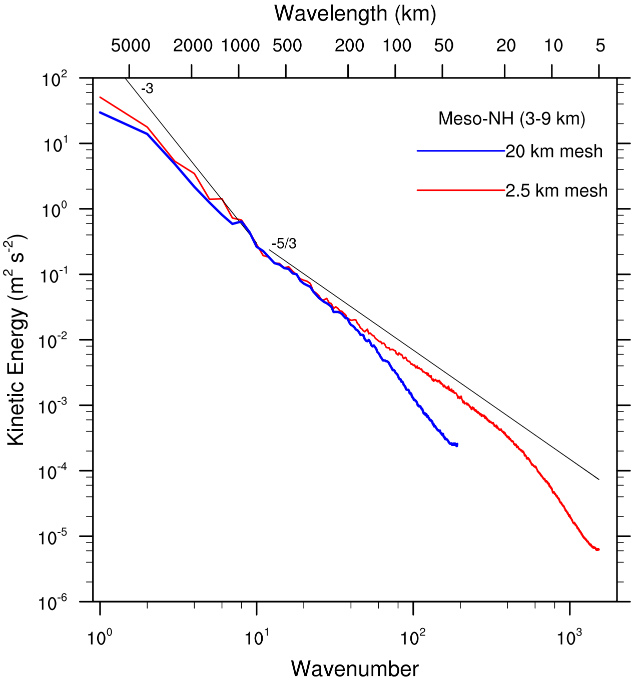

FIG. 2. Kinetic energy spectra of vertical velocities for HiRes ($\Delta x = 2.5$ km) and LowRes ($\Delta x = 20$ km) at 0000 UTC 15 Jun 2006, between 3 and 9 km of altitude. The theoretical power laws at −3 and −5/3 are shown with black lines.

observations are computed offline using the Radiative Transfer for the Television and Infrared Observation Satellite (TIROS) Operational Vertical Sounder (RTTOV) code, version 8.7 (Saunders et al. 2005), as previously used by Chaboureau et al. (2008). Two observation datasets are used to assess the simulations: the globally merged 4-km-resolution BT data (Janowiak et al. 2001), merged from all available geostationary satellites and provided by the Climate Prediction Center, and the 3-hourly product 3B42, version 7 (Huffman et al. 2007), from the Tropical Rainfall Measuring Mission (TRMM) available in 0.25° spatial resolution. The gridded BT data eases the comparison with the model outputs while the temporal sampling of the TRMM 3B42 product is convenient for the analysis of the diurnal cycle of precipitation, a feature that results in the TRMM 3B42 product being widely employed (e.g., Janiga and Thorncroft 2014; Zhang et al. 2016).

3. Rain-attribution approach

Clouds and their associated precipitation are analyzed in a grid mesh of 20 km for all the datasets. Such a common grid mesh is necessary to analyze the observation datasets, which have a different resolution (4 km for MSG against 0.25° for TRMM). The sensitivity of the cloud size distribution to the resolution further requires the same grid mesh to be used. We then define two cloud categories. Following many others (e.g., Mathon et al. 2002; Tian et al. 2004; Laing et al. 2008; Söhne et al. 2008), DCCs are diagnosed for BT less than 230 K while cirrus anvil clouds (CACs) are identified for BTs ranging between 230 and 260 K. Because the simulated BTs are biased toward higher values (mostly because of model errors in the location and height of cloud cover; Fig. 3a), we use different BT thresholds for the simulations. They are defined in such a way that each cloud category is equally represented over the 6-day period whatever the dataset. In other words, the thresholds are adjusted so that the number of DCCs and CACs is the same in both the observations and the simulations. This leads to the thresholds of 243 and 266 K for HiRes and 246 and 264 K for LowRes. From Fig. 3a, it can be noted that the simulated BTs corresponding to the DCC category are generally higher than observed. This is more pronounced for LowRes. It suggests that DCCs may be shallower for LowRes with respect to HiRes, and may present a lower content of iced hydrometeors. This could eventually lead to a reduction of precipitation.

The 3-hourly accumulated precipitation is attributed to each 20-km grid point. Note that daily amounts of precipitation of less than 0.2 mm are considered as traces (WMO 2014) and are excluded from the analysis. Figure 3b shows that they are very frequent (52% for TRMM, 56% for HiRes, and 36% for LowRes). Ruling out these grid points with trace values nevertheless allows us to consider 99.5% of the total precipitation whatever the dataset. The frequency of grid points in the range between 0.2 and 10 mm day^{-1} is approximately 40% for TRMM and HiRes, and 57% for LowRes. The production of many cells with low intensity rainfall is a well-known failure of parameterized convection. Grid points with precipitation in this range produce 48% of total precipitation for TRMM and about 10% more for the simulations. Precipitation rates between 10 and 50 mm day^{-1} represent 5%, 7%, and 8% for HiRes, LowRes, and TRMM, respectively. In TRMM, this represents 51% of total precipitation, approximately 12% greater than in the simulations. Precipitation rates over 50 mm day^{-1} are more frequent for HiRes (0.08%) than for TRMM (0.03%) or LowRes (0.05%) and they produce more precipitation for HiRes (2%) than for TRMM (0.5%) or LowRes (1%). Still, the precipitation rates shown in Fig. 3b present a lower cutoff for HiRes as a consequence of precipitation being regridded to a 20-km resolution. Regridding precipitation acts to smooth the extreme values, which also explains the less frequent precipitation rates over 50 mm day^{-1} found for TRMM compared to LowRes.

DCC and CAC grid points are then aggregated into clusters. We define clusters as contiguous grid points of the same cloud category. Grid points are considered contiguous only if they share a common face. Each DCC cluster is further associated with 3-hourly accumulated precipitation and vertical profiles of thermodynamic variables. For the observed clusters, the precipitation is obtained from TRMM while the vertical profiles are taken from the ECMWF analysis at 0000, 0600, 1200, and 1800 UTC and from the ECMWF 3-h forecasts at 0300, 0900, 1500, and 2100 UTC. For the simulated clusters, the precipitation and profiles are taken from the model outputs. The profiles associated with each DCC cluster are computed in the volume generated when the envelope of the cluster is projected into the vertical. They are calculated both at the time of the detection and 6 h before at the same location. This allows us to analyze the properties of the DCC clusters and of their environmental conditions prior to their detection, respectively. An example of the rain-attribution method applied to the observation is shown at 2100 UTC 11 June (Fig. 4). This time is selected because DCCs of different sizes are located all over northern tropical Africa (Fig. 4a). The 3-hourly accumulated precipitation is attributed to all of them (Fig. 4b).

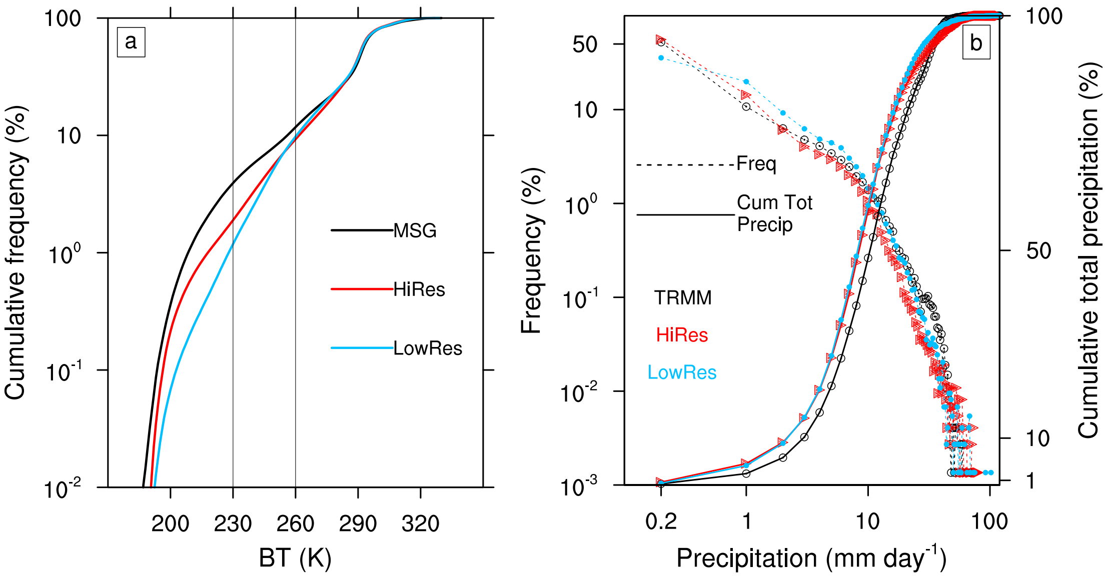

FIG. 3. (a) Cumulative distribution function of brightness temperature at 3-h resolution on a 20-km grid for MSG, HiRes, and LowRes. (b) Distribution function of total accumulated precipitation over the 6-day period by class of 1 mm day^{-1} on a 20-km grid for TRMM, HiRes, and LowRes.

Finally, a tracking method is used to follow DCCs and their characteristics over time. Geographical overlapping between successive BT images has been extensively used (e.g., Machado et al. 1998; Mathon et al. 2002; Fink et al. 2006), with different surface overlapping ratios. After testing several overlapping ratios in the range between 5% and 35%, we set the ratio to 20%. This produces the most realistic trajectories (i.e., trajectories that match results found in the literature in terms of number, propagation speed, and duration of the tracked cloud systems) (e.g., Machado et al. 1998; Goyens et al. 2012). Machado et al. (1998) suggest considering only clusters larger than 10 000 km^2 when the temporal resolution of the satellite images is greater than 3 h. Because the tracking is done on a 3-hourly basis, it is applied only to clusters with an effective diameter larger than 120 km, equivalent to an area of 11 300 km^2. The effective diameter is defined as the diameter of a circle having an area equal to that of the DCC. In the following, DCCs that satisfy this threshold on the effective diameter are called MCSs, and the rest small DCCs. Then, MCSs are divided into two categories according to their lifetime. Long-lived MCSs last at least 6 h and short-lived MCSs last less than 6 h. Three subregions (Fig. 4a) are considered to cover most of the continental tropical band within the domain while contrasting in the atmospheric conditions in which MCSs developed, as will be shown later: southern West Africa (SWA), central Africa (CAF), and Ethiopia (ETH).

4. Overview of clouds and precipitation

a. Distribution

The spatial distribution of DCCs and precipitation is shown in Fig. 5. DCCs are observed south of 15°N in a zonal band that extends from the Atlantic Ocean to 40°E, the monsoon trough. DCCs are also visible over Algeria, near the foothills of the Hoggar Mountains (Fig. 5a). They are the most frequent over the eastern Atlantic and the Ethiopian Highlands. Precipitation is also observed over the zonal band but not over Algeria (Fig. 5d). Accumulated rainfall values are highest over the eastern Atlantic and the Ethiopian Highlands, consistent with the locations found for the highest frequencies of DCCs. Over the continent, precipitation is mainly found south of the intertropical discontinuity (ITD) defined as the continental boundary that separates the northeasterly dry, warm harmattan flow and the southwesterly cold, moist monsoon flow. Most of the continental precipitation occurs inside the three subregions previously defined (Fig. 5d). In SWA, the precipitation presents the greatest values west of the Jos Plateau, over the center of Benin and over the flatter regions around the border of Ivory Coast, Ghana, and Burkina Faso. In CAF, the precipitation is maximum around the northern border of Democratic Republic of Congo, the southwestern region of central Africa and in southern Chad. In ETH, precipitation is mostly distributed over the Ethiopian Highlands, where the maximum values appear on the western slopes.

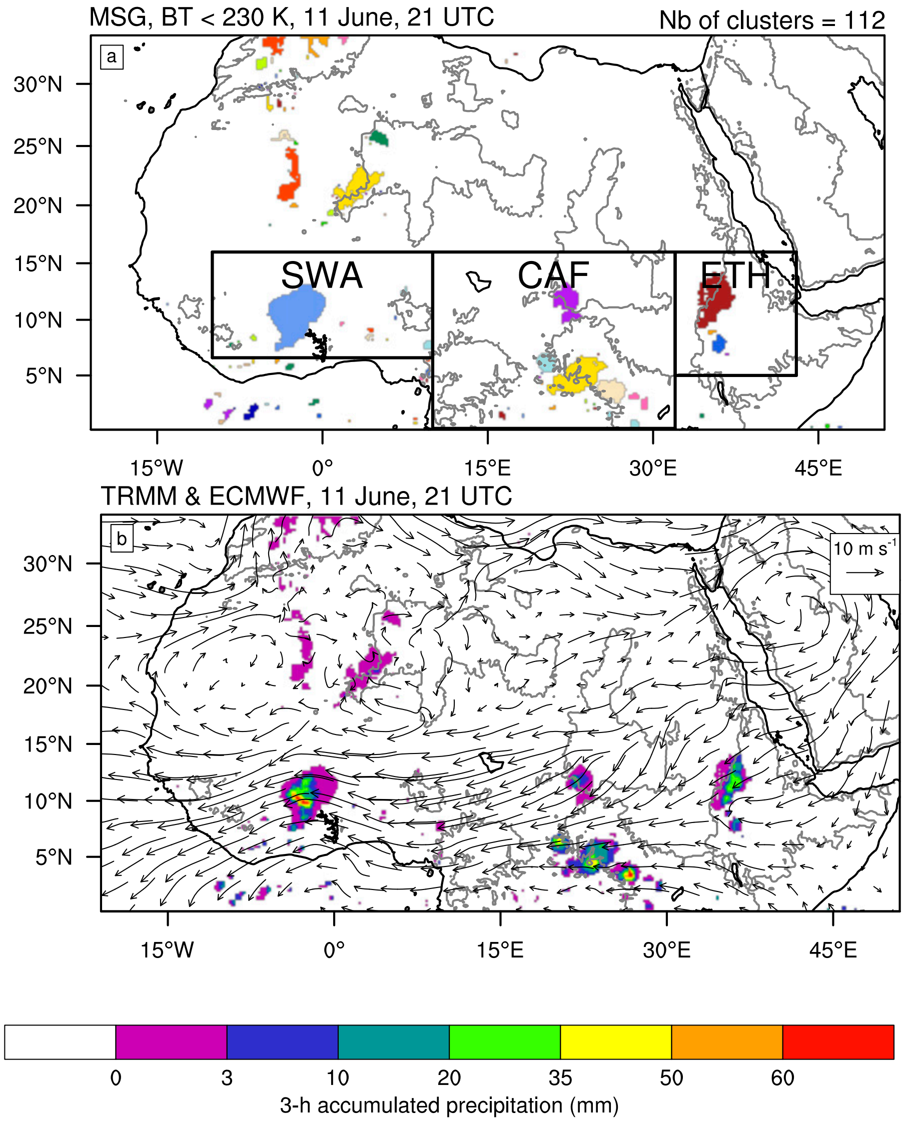

FIG. 4. (a) Example of the identification of DCC clusters at 2100 UTC 11 Jun 2006. A color is assigned to each cluster. (b) The attribution of 3-h accumulated precipitation from TRMM product 3B42 to each cluster in (a). The solid gray lines represent the orography at 600-m altitude. In (a), the black squares delimit three subregions: southern West Africa (SWA), central Africa (CAF), and Ethiopia (ETH).

In both simulations, the zonal patterns of DCCs and precipitation are reproduced well. DCCs are, however, missing over the Gulf of Guinea close to the southern limit of the simulation domain. The development of clouds is inhibited there by the strong southwesterly monsoon inflow. DCCs are overestimated over the Gulf of Guinea along almost all of the coast. DCCs and precipitation show a reduced extension over the eastern Atlantic, with DCCs being too frequent and precipitation too weak. This is more marked in HiRes than in LowRes. Moreover, in the HiRes simulation, precipitation exceeds 40 mm day^{-1} over the coast of Sierra Leone and Liberia, whereas, for TRMM, we find lower values, of up to 30 mm day^{-1}. Finally, simulated DCCs are more frequent over the Ethiopian Highlands and much more widespread over Algeria than observed. Furthermore, LowRes produces more precipitation over Algeria than TRMM and HiRes.

The total precipitation caused by different cloud categories is computed by associating 3-hourly accumulated precipitation with the clusters of different cloud categories (Fig. 6). In the observations, 71% of total precipitation comes from DCCs and 19% is due to CACs. The remaining precipitation (10%) is attributed to clouds other than DCCs or CACs. Long-lived MCSs account for 55% of precipitation, short-lived MCSs for

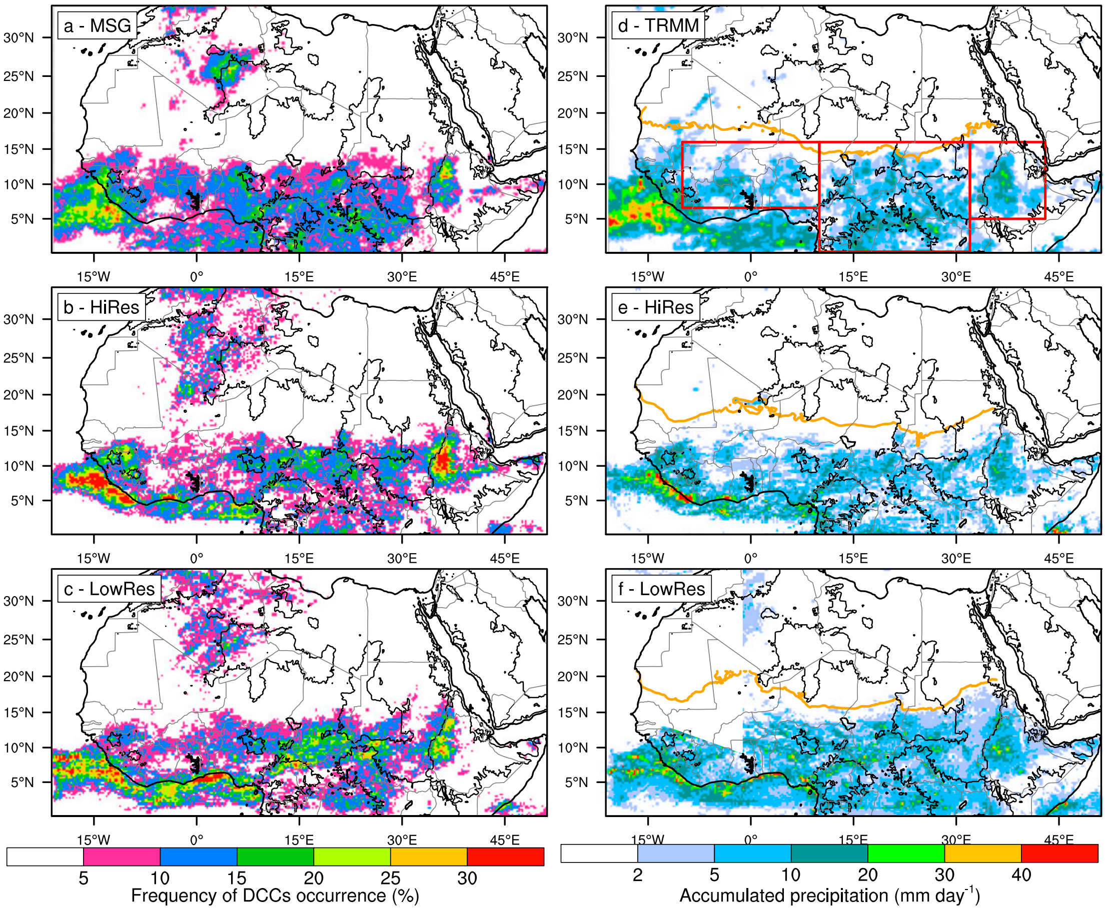

FIG. 5. (left) Frequency of occurrence of DCCs during 9–14 Jun 2006 for (a) MSG, (b) HiRes, and (c) LowRes. (right) Mean total accumulated precipitation during the same period for (d) TRMM, (e) HiRes, and (f) LowRes. The solid black lines show the orography at 600-m altitude. In (d), the red squares delimit the subregions as in Fig. 4a. The orange lines in (d)–(f) show the ITD defined as where the average water vapor mixing ratio at 2 m equals 10 g kg^{-1} (Chaboureau et al. 2016).

11% and the remaining 5% comes from small DCCs. Therefore, MCSs produce 66% of total precipitation, which is in the range of contributions found for different regions in West Africa (e.g., Mathon et al. 2002; Fink et al. 2006; Bayo Omotosho 1985). HiRes reproduces this distribution well, with 66% of precipitation coming from DCCs, 17% from CACs, and 17% from other clouds. Long-lived MCSs produce 50% of precipitation, short-lived MCSs contribute to 10%, and small DCCs to 6%. Thus, long-lived MCSs in HiRes are the first contributors to precipitation as observed. LowRes is not able to reproduce this feature as long-lived MCSs produce only 29% of precipitation, a contribution similar to that of CACs (24%) and other clouds (33%). In fact, clouds other than DCCs are the main contributors to precipitation. In LowRes, for which deep convection is parameterized, 70% of the total precipitation is produced by the parameterization while the DCCs only produce 43% of precipitation. One reason is that the parameterization inhibits the vertical development of the DCCs, which present too low a hydrometeor content. This was previously pointed out from Fig. 3a.

The observed MCSs cover a surface of almost 11 million km^2 over the 6 days and they produce 66% of total precipitation (Fig. 6). In the simulations, the MCSs cover about the same surface area (98% of what is observed) but contribute less to total precipitation. In fact, HiRes produces 6% less precipitation. This means that precipitation caused by MCSs in HiRes is less intense than observed, with less precipitation produced per unit area. In LowRes this is more pronounced, with 30% less precipitation.

b. *Diurnal cycle of precipitation*

The diurnal cycle of precipitation is examined in Fig. 7. Over land, the observed diurnal cycle has an amplitude of 0.37 mm day^{-1} and a maximum value of 0.56 mm day^{-1} at 2100 LST (Fig. 7a). For HiRes the

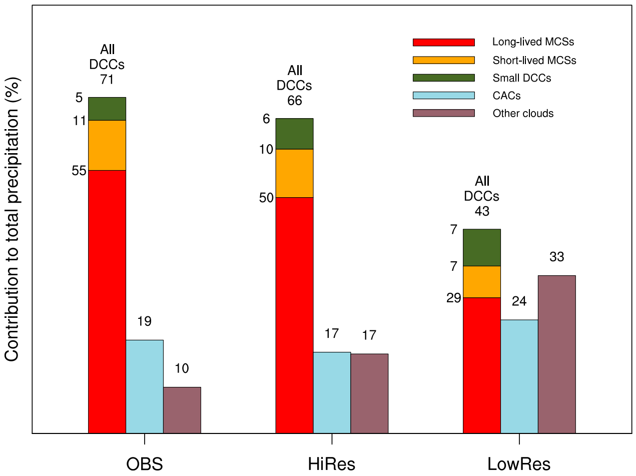

FIG. 6. Contribution of all the DCCs (long- and short-lived MCSs and small DCCs), CACs, and other clouds to total precipitation over the whole domain for the observations and the simulations.

observed amplitude, the maximum rainfall rate, and the time of peak precipitation are well reproduced (0.34 mm day^{-1}, 0.55 mm day^{-1}, and 2100 LST, respectively). However, HiRes lacks precipitation between 0000 and 0900 LST, up to 0.2 mm day^{-1}. LowRes also shows a diurnal cycle with similar amplitude and maximum values (0.38 and 0.60 mm day^{-1}) but it peaks earlier, at 1500 LST, a common feature of parameterized convection in the tropics. Over the ocean (Fig. 7b), the diurnal cycle is less pronounced than over land, with amplitudes of 0.12, 0.10, and 0.08 mm day^{-1} for the observations, HiRes, and LowRes, respectively. This result can be explained by the fact that the ocean has a greater thermal inertia than the land. The maxima over the ocean occur at 0900 LST and the simulations lack precipitation (as shown previously in the southern limit of the simulation domain).

Because continental precipitation explains the diurnal cycle of total precipitation at first order, the diurnal cycle over land is further analyzed by partitioning it according to the different cloud categories (Figs. 7c,d). For the observations, long-lived MCSs show the largest values for precipitation, larger than 0.1 mm day^{-1}. This is expected as the observed long-lived MCSs contribute the most to the total precipitation (55%). They present the highest values of precipitation between 1800 and 0300 LST, over the same time range as for the precipitation over land. Thus, long-lived MCSs over land explain most of the diurnal cycle of precipitation. Clouds other than DCCs are the second greatest contributors to the diurnal cycle, with values between 0.06 and 0.2 mm day^{-1}. This is also expected as these clouds are the second contributors to the total precipitation (29%). Their peak at 1800 LST suggests that these clouds are sensitive to the diurnal cycle of surface fluxes over land. Short-lived MCSs are the third contributors to the total precipitation, with a diurnal variation of approximately 0.05 mm day^{-1}. Precipitation resulting from short-lived MCSs shows two peaks, around 0600 and 2100 LST. Last, small DCCs present fairly constant precipitation with respect to time, of around 0.02 mm day^{-1}.

HiRes reproduces the distribution of total precipitation among cloud categories well, as seen in Fig. 6, but it underestimates the contribution of long-lived MCSs between 0000 and 1200 LST by almost 0.2 mm day^{-1}. It also overestimates the contribution of clouds other than DCCs by about the same amount at 1200 and at 0000 LST. HiRes lacks precipitation for short-lived MCSs between 0300 and 0600 LST, of about 0.05 mm day^{-1}, because precipitation from short-lived MCSs is single peaked for HiRes. In summary, the success of HiRes in capturing the total precipitation over land between 1200 and 2100 LST comes partly from compensating errors between the different contributors. The lack of nocturnal precipitation over land after midnight in HiRes is due to long-lived and short-lived MCSs, and clouds other than DCCs.

For LowRes, the main contribution to the diurnal cycle of precipitation comes from clouds other than DCCs, with values ranging between 0.1 and 0.4 mm day^{-1}. This is expected as these clouds contribute to 57% of the total precipitation. The peak in precipitation at 1500 LST resulting from these clouds mainly explains the early peak in total precipitation over land. This peak is mainly controlled by the precipitation produced by the convective parameterization, which is also maximum at 1500 LST (not shown). The second contributor is long-lived MCSs, with values in their diurnal cycle of between approximately 0.1 and 0.2 mm day^{-1}. LowRes underestimates the contribution of long-lived MCSs by at least a factor of 2. It is, however, able to reproduce the phase of the diurnal cycle correctly. Another drawback concerns the double peaks in precipitation missed for the short-lived MCSs, as pointed out for HiRes, and the overestimation of afternoon precipitation for small DCCs.

The differences in the diurnal cycle of precipitation resulting from long-lived MCSs are further analyzed by subregion (Fig. 8). For HiRes (Figs. 8a–d), continental long-lived MCSs lack precipitation after midnight, while producing an excess of precipitation in the afternoon. This can be explained by a compensating effect between an excess of precipitation over ETH between 1500 and 2100 LST and a systematic deficit in precipitation over SWA and CAF. For LowRes (Figs. 8e–h), the deficit in precipitation caused by long-lived MCSs also comes mostly from SWA and CAF. Precipitation is best captured over ETH in both simulations, which can be explained by the strong orographic enhancement of precipitation there.

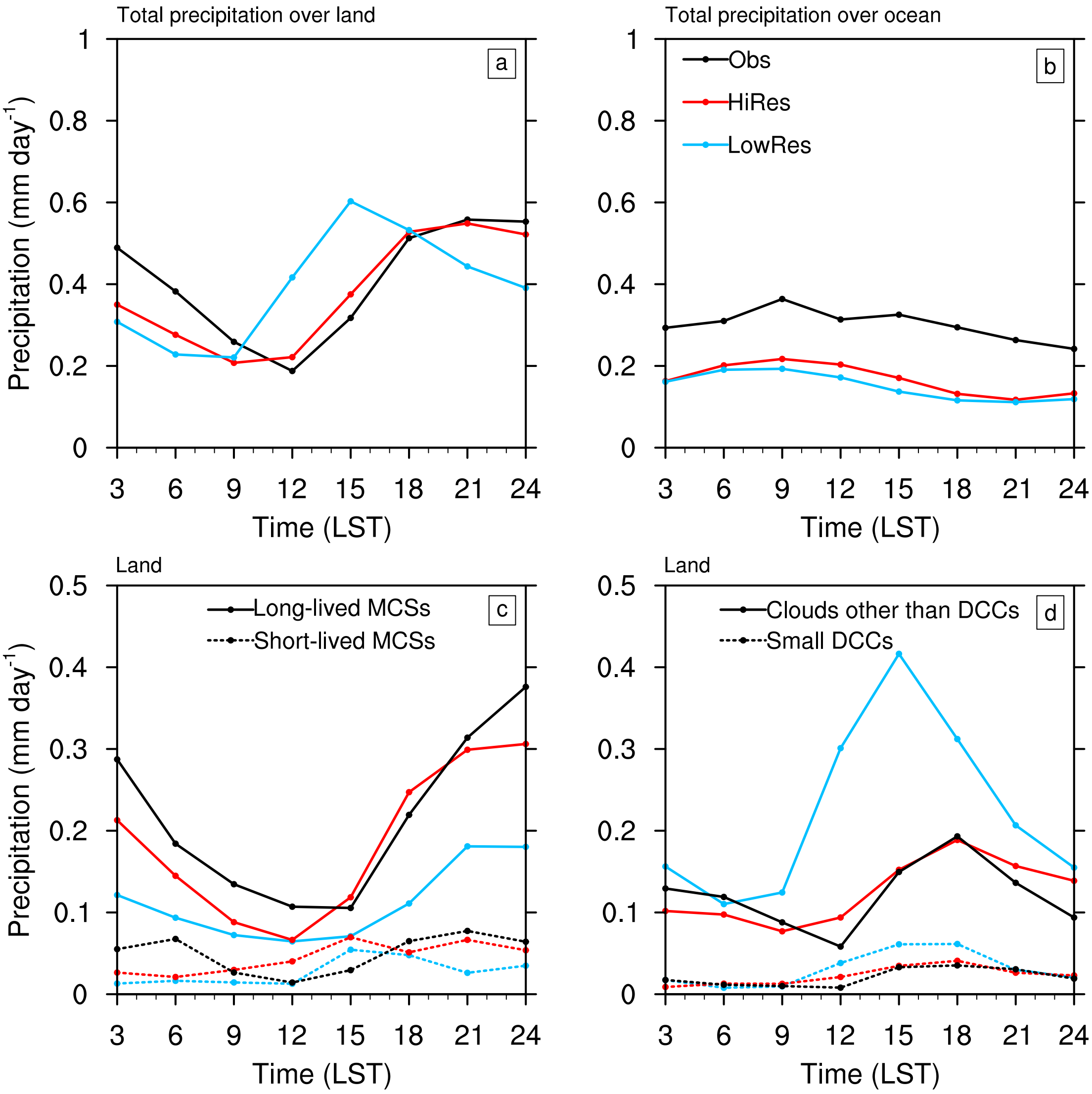

FIG. 7. Diurnal cycle of (a) precipitation over land, (b) precipitation over ocean, (c) precipitation over land due to long-lived MCSs and short-lived MCSs, and (d) precipitation over land due to clouds other than DCCs (e.g., CACs and other clouds), and small DCCs for the observations and both simulations.

5. Characteristics of long-lived MCSs by subregion

a. *Size and propagation*

Because long-lived MCSs account for most of the observed precipitation, it is essential to describe such systems and to evaluate the capability of the simulations to statistically reproduce the characteristics of their population. The trajectories of long-lived MCSs are depicted in Fig. 9. Their number decreases with the duration whatever the dataset, as found by others (e.g., Fink et al. 2006; Laing et al. 2008). In the regions where long-lived MCSs form and grow, favorable conditions provide them with energy that will eventually decay unless the long-lived MCSs are enhanced during their propagation. Laing et al. (2008) argue that an approximately exponential decay of the number of MCSs over their lifetime is expected. Among the 62 observed trajectories, which have an average lifetime of 11.3 h, the majority start over the continent. The observed long-lived MCSs are first detected over the Ethiopian Highlands, near the borders of the Darfur Plateau and the Cameroon Highlands in CAF, the borders of the Jos Plateau in SWA, and to the west of SWA, close to the Guinea Highlands. Over the ocean, long-lived MCSs are first detected mostly on the Gulf of Guinea. The long-lived MCSs propagate principally from east to west, within the AEJ. For the simulations, they are more numerous and shorter lived than observed (84 with an average duration of 10.7 h for HiRes and 104 with a duration of 10.4 h for LowRes). Their first detections are spatially distributed in a similar way to observations for both simulations.

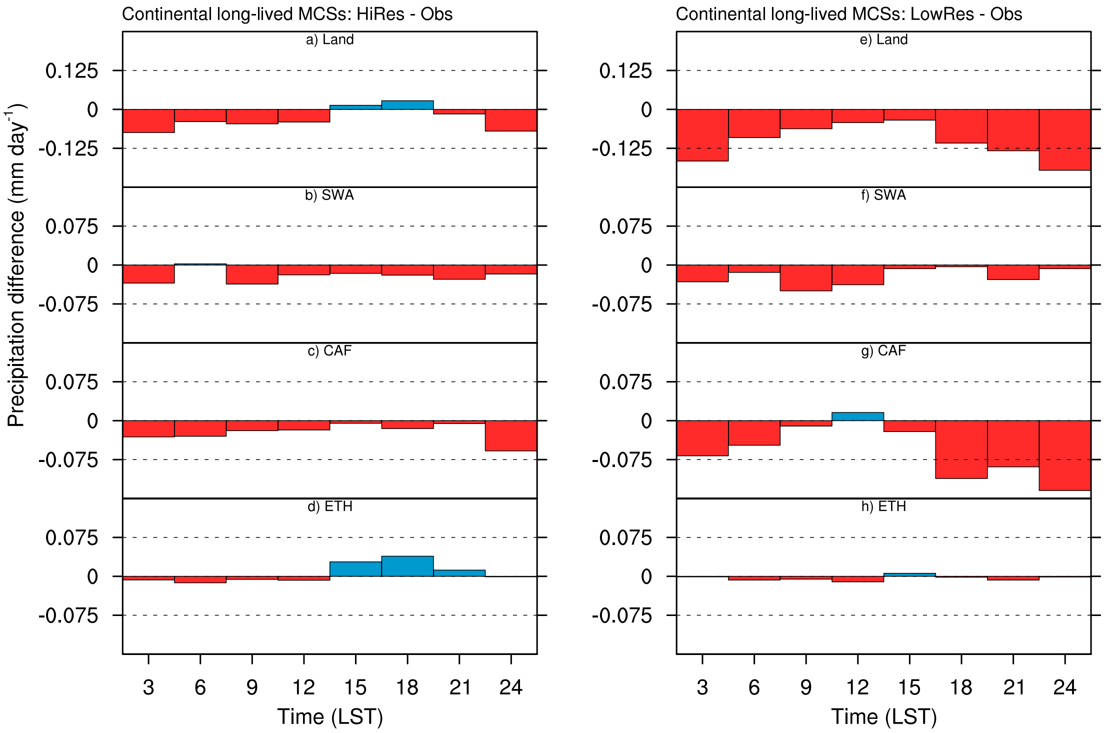

FIG. 8. Differences in the diurnal cycle of precipitation due to long-lived MCSs between (left) HiRes and the observations and (right) between LowRes and the observations for (a),(e) land; (b),(f) SWA; (c),(g) CAF; and (d),(h) ETH.

The propagation characteristics of long-lived MCSs by subregion are shown in Fig. 10. A trajectory is associated with the subregion where the long-lived MCS spends most of its lifetime (i.e., where the majority of the MCS track points shown in Fig. 10 lie). Zonal and meridional speeds are computed for each MCS, using their locations between their first and last detections. Observed long-lived MCSs are first detected mostly over CAF. Their effective diameter increases from east to west, from 300 km over ETH to 600 km over SWA. Their duration is about 10 h over ETH and CAF and 20 h over SWA. They have an average zonal speed of $-8.5\,\mathrm{m\,s^{-1}}$ in ETH, $-10.1\,\mathrm{m\,s^{-1}}$ in CAF, and $-17.8\,\mathrm{m\,s^{-1}}$ in SWA. Their meridional speeds are lower in absolute value; they are 2.1, 2.5, and $-1.5\,\mathrm{m\,s^{-1}}$ for ETH, CAF, and SWA, respectively. Thus, while the observed long-lived MCSs mainly propagate westward, they present a northward component in ETH and CAF, and a southward component in SWA. The long-lived MCSs over SWA are the most organized. They are the largest, fastest, and longest-lived MCSs of all the subregions.

Both simulations overestimate the number of long-lived MCSs over the three subregions, the number is 44% greater for HiRes and 93% greater for LowRes. The 44% excess for HiRes is close to the 53% overestimate of MCS tracks found in a 6-day convection-permitting simulation over West Africa (Beucher et al. 2014). For HiRes, many of the too numerous long-lived MCSs over ETH are simulated in the afternoon (not shown), which may explain the excess of afternoon precipitation (Fig. 8d). The increase in effective diameter of long-lived MCSs from east to west is not reproduced by the simulations. The effective diameter remains the same in the three subregions. It is, therefore, well captured over ETH but too low over CAF and strongly underestimated over SWA. The duration of long-lived MCSs is correctly simulated in CAF and ETH, but too low over SWA. In both simulations, the long-lived MCSs propagate westward, and are the fastest over SWA. For HiRes, the zonal speed over SWA is, however, about one-third lower than observed (-11.5 vs $-17.8\,\mathrm{m\,s^{-1}}$). For LowRes, the long-lived MCSs are too slow in all the three subregions. LowRes simulates the observed northward propagation of long-lived MCSs in CAF and ETH and the southward propagation in SWA, but long-lived MCSs for HiRes are too westward directed.

In summary, the long-lived MCSs are observed to increase their size, lifetime, and propagation speed from ETH to SWA. In a general way, the main propagation characteristics of long-lived MCSs, such as their number, diameter, lifetime, and propagation speed are better

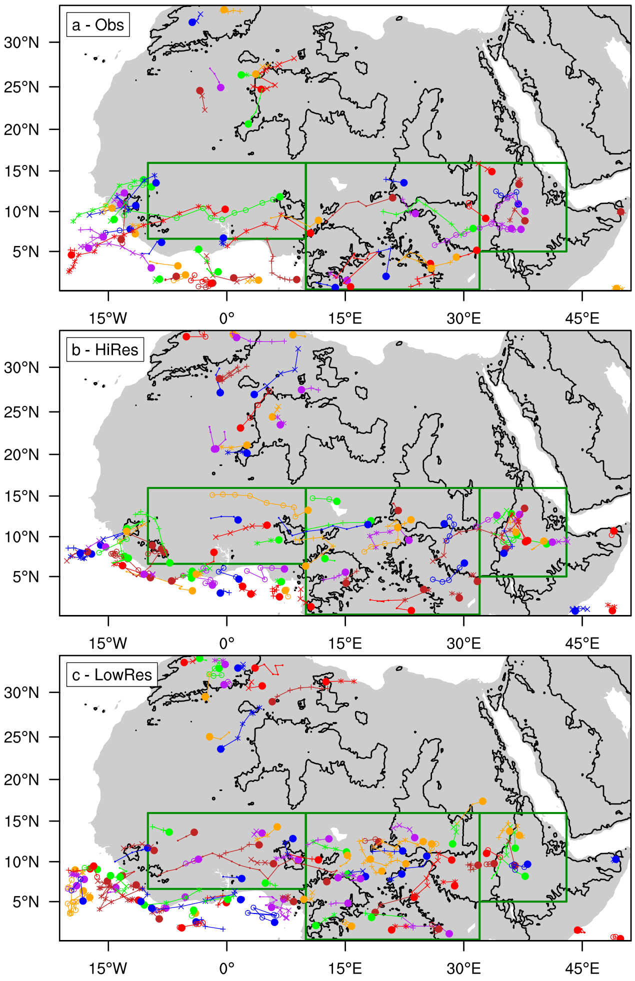

FIG. 9. Tracked trajectories of long-lived MCSs (duration of at least 6 h) for (a) the observations, (b) HiRes, and (c) LowRes. The dots represent the first detection of each MCS. The changing colors among trajectories have no significance. The solid black lines show the orography at 600-m altitude.

captured by HiRes than by LowRes. Nevertheless, HiRes presents strong biases over SWA, notably as the long-lived MCSs show a weak degree of organization and an incorrect meridional propagation.

b. Environmental conditions

To understand why the long-lived MCSs differ with the subregion, we examine the environmental conditions in which these MCSs develop (Fig. 11). In the observations, near-surface moisture is maximum over SWA, with a value of water vapor mixing ratio of 16 g kg^{-1}, and the low- to midlevel atmosphere presents the strongest vertical gradient of equivalent potential temperature θ_e. In other words, the conditional instability is the greatest there. This can lead to convection being more intense over SWA when triggered. The speed of the AEJ, located at around 4-km altitude with an easterly direction, increases from east to west. Its maximum ranges from 8 m s^{-1} over ETH, to 10 m s^{-1} over CAF, and to 16 m s^{-1} over SWA, where the AEJ is the strongest, in agreement with the zonal propagation speed of long-lived MCSs (Fig. 10). Between 0.8- and 2-km altitude, the wind direction changes abruptly. Below 2 km the average southwesterly flow corresponds to the monsoon flow. Note that the variability in the wind direction among the individual profiles is much greater in the lower atmosphere than aloft. This is mostly due to the diurnal variability associated with solar heating, which affects the boundary layer circulation. In mountainous areas like ETH, the orography can also play a partial role, as the slope breeze modulates the monsoon flow. Thus, a strong vertical shear is found between the low-level southerly and the midlevel easterly flows, with the largest values over SWA.

HiRes reproduces the observed profiles of water vapor mixing ratio over CAF and SWA very well, but overestimates the water vapor mixing ratio above 2-km altitude over SWA. For example, at 2.8-km altitude, HiRes shows a value of 7.7 g kg^{-1} compared to 6.5 g kg^{-1} for the observations. LowRes shows a persistent increase in water vapor mixing ratio at the low level and a deficit at the midlevel, in all the three subregions. This is consistent with insufficient injection of moisture through convective updrafts. The increase in both the convective instability and AEJ speed from ETH to SWA is captured by the simulations. The mean monsoon flow is generally overestimated for LowRes, and also for HiRes over SWA. The poor reproduction of the propagation of the long-lived MCSs by HiRes over SWA may be due to differences between the observations and HiRes in the wind at altitudes around 3 km, the steering level for MCS propagation. Indeed, its mean direction is 77° for the observations and 84° for HiRes. Moreover, the meridional wind at 3-km altitude for HiRes shows the greatest variability in intensity over SWA. For some individual profiles, it is southerly, indicating that moist air is advected northward to SWA (not shown).

c. Properties of long-lived MCSs

To examine the convective response to the larger-scale environmental forcing, average profiles of the long-lived MCSs are shown in Fig. 12. Each MCS is associated with the subregion where it spends most of its lifetime. For both simulations, liquid hydrometeors appear mostly up to the freezing level, around 4 km, with a drastic reduction above. A small amount of supercooled water is present up to 9 km, before the cloud droplets freeze completely. The solid hydrometeor content increases above 4 km, reaching a maximum around 9 km, and is nonzero up to 17 km, approximately the height of the tropopause. The release of latent heat through the

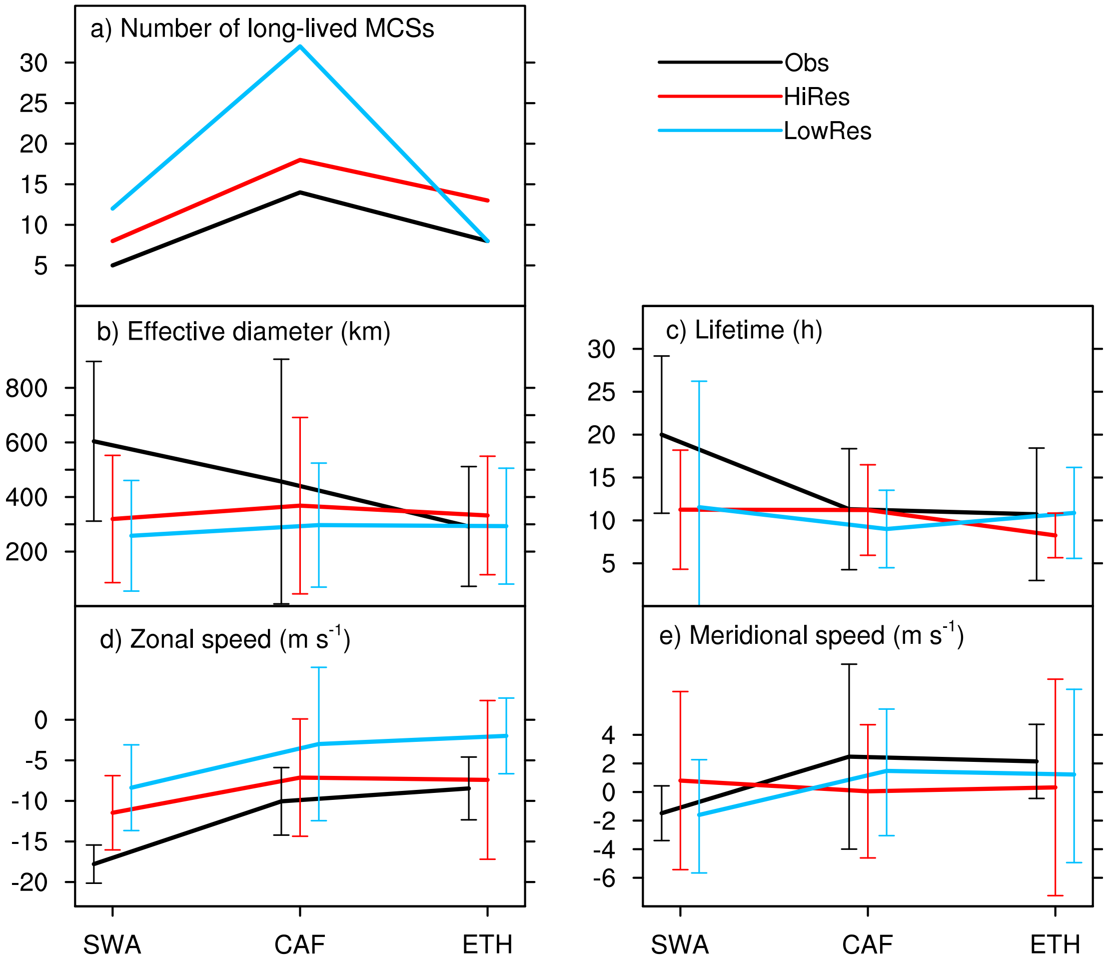

FIG. 10. Characteristics of long-lived MCSs by subregion (SWA, CAF, and ETH) for the observations and the simulations: (a) number of first detections, (b) effective diameter, (c) duration, (d) zonal speed, and (e) meridional speed. In (b)–(e), the solid lines represent the mean values and the error bars represent the standard deviation.

freezing of liquid particles and the deposition of water vapor accelerates the air parcels, which show the greatest upward velocities between altitudes of 6–9 km. Over SWA and CAF, both the hydrometeor loading and upward velocities are larger than over ETH, as there is more convective instability. Over SWA and CAF the freezing level and maximum upward speeds are reported to be 1 km higher than over ETH. The updrafts and downdrafts are stronger for HiRes than for LowRes, an effect of the fully explicit representation of convection and the horizontal resolution. The cold, dry subsiding air is diagnosed by a decrease in θ_e in the lower 3 km between the conditions before and at the time of convection, which has the effect of stabilizing the atmosphere. The reduction of θ_e, which is a signature of cold pools, increases from ETH to SWA. This drop is greater for HiRes than LowRes whatever the subregion. The most intense cold pools are found over SWA for HiRes, where, in the lowest 500 m, there is an average decrease of θ_e of up to 10 K. However, the presence of a layer of insufficiently dry air at 3-km altitude, which feeds the cold pools, could result in the pools not being intense enough. The too slow propagation of the long-lived MCSs over SWA in HiRes and their reduced duration could be a consequence of simulating cold pools that are too weak.

6. Conclusions

This study examines continental precipitating systems over northern Africa from 9 to 14 June 2006. A common method is applied to the observations and to two simulations (convection permitting and with parameterized convection), for which MCSs are tracked and their properties analyzed in detail over southern West Africa (SWA), central Africa (CAF), and Ethiopia (ETH).

The analysis of the observations shows that continental precipitation is distributed over a zonal band south of the ITD, from the Ethiopian Highlands to the Atlantic. The highest precipitation rates and the maximum of DCCs

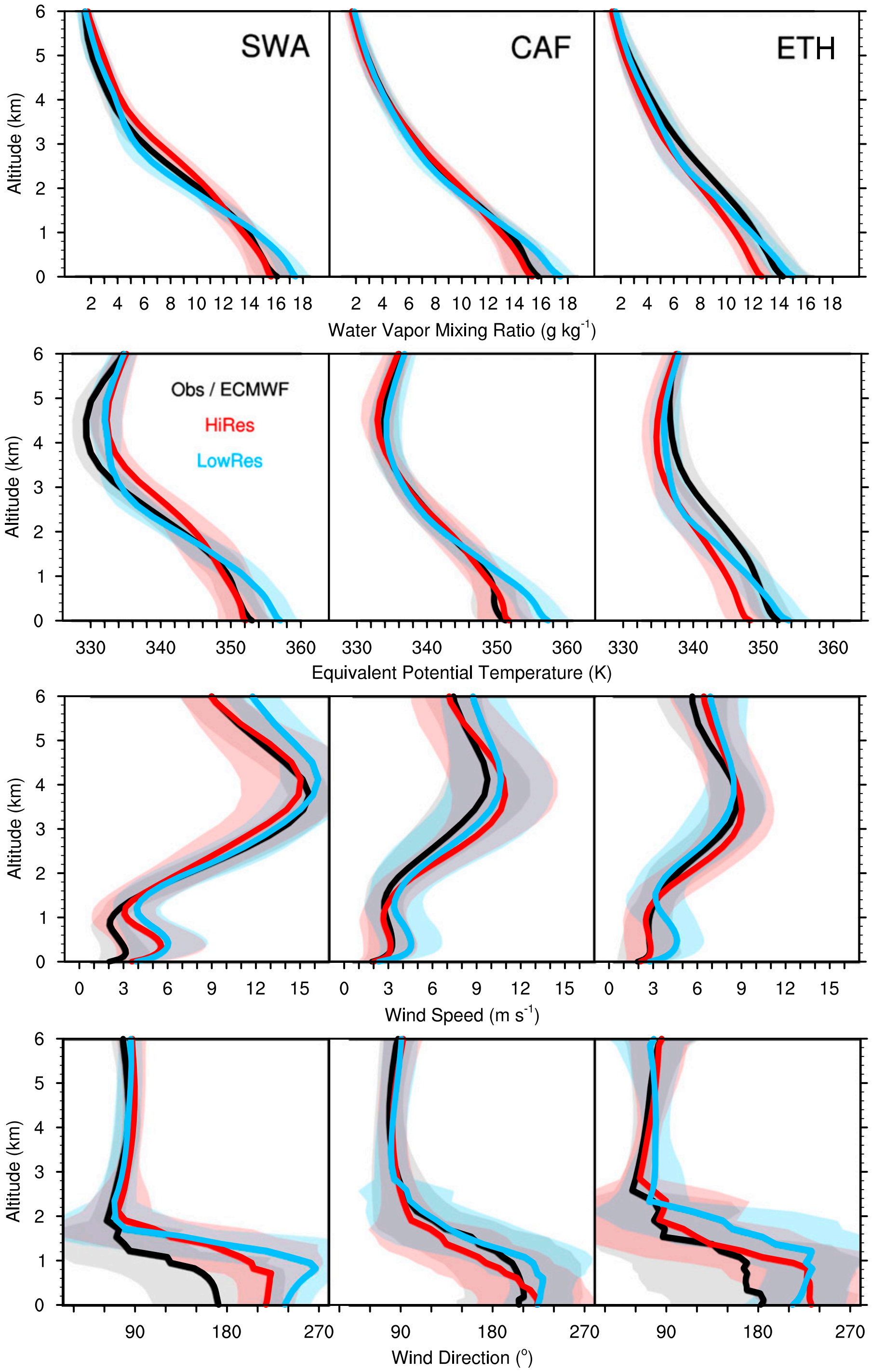

FIG. 11. Mean vertical profiles of (from top to bottom) water vapor mixing ratio, equivalent potential temperature, wind speed, and wind direction for long-lived MCSs for each subregion: (left) SWA, (middle) CAF, and (right) ETH. The subregions are shown in Fig. 4a. The profiles are computed 6 h before the long-lived MCSs detection. The shaded contours show the standard deviation for each dataset.

occur off the Atlantic coast, as has also been obtained with TRMM climatology (Janiga and Thorncroft 2014). The total precipitation and its diurnal cycle are partitioned by type of precipitating system here. The observed MCSs produce 66% of the total precipitation over the whole analysis domain. The rest of the precipitation during the 6-day period comes from CACs, isolated convective cells, or other clouds. The long-lived MCSs

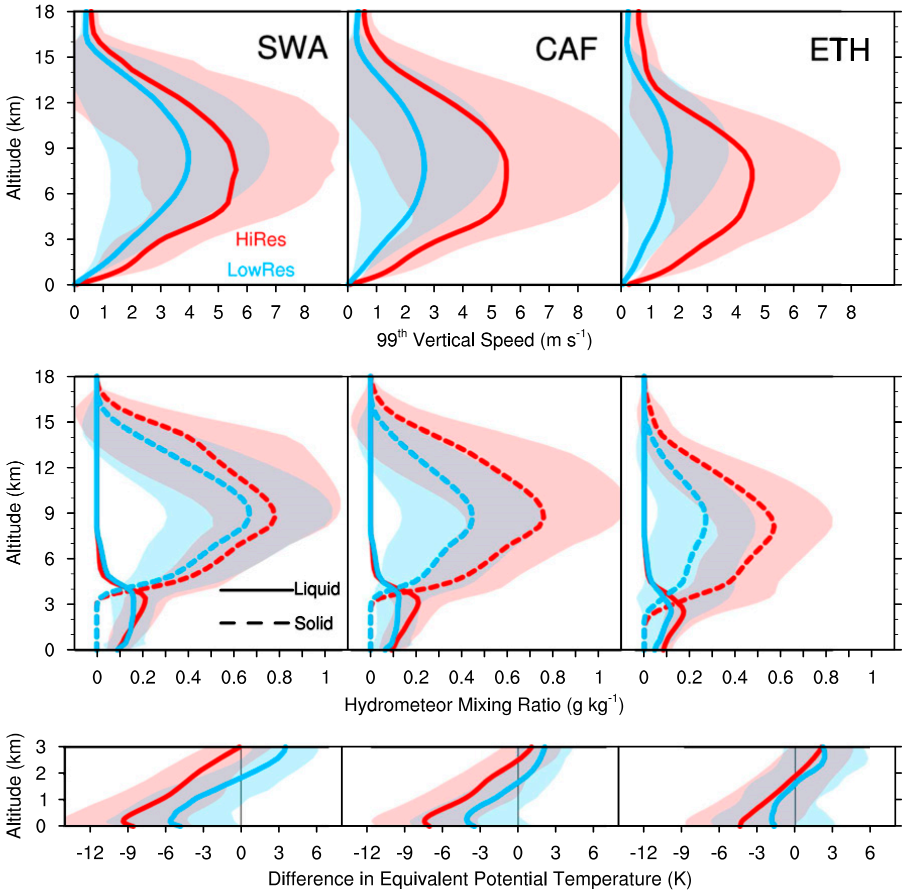

FIG. 12. Mean vertical profiles of (from top to bottom) 99th percentile of the vertical wind speed, mean hydrometeor mixing ratio (liquid and solid) for long-lived MCSs, and difference of mean equivalent temperature inside the long-lived MCSs and at the same location 6 h before, for (left) SWA, (middle) CAF, and (right) ETH. The shaded contours show the standard deviation for each dataset.

produce 55% of total precipitation. They mainly explain the diurnal cycle of continental precipitation, which peaks in the evening. Furthermore, they are the first contributor to nocturnal precipitation, as well-developed MCSs can sustain themselves for several hours when surface fluxes are strongly reduced. Overall, the number of long-lived MCSs decreases with increasing lifetime. The number, effective diameter, and propagative properties of the long-lived MCSs have been further analyzed by subregion. The westward long-lived MCSs present a southward component over SWA. They are the largest, fastest, and longest-lived when compared to CAF and ETH. The AEJ increases in strength from ETH to SWA, in turn increasing the vertical shear, a key mechanism in the organization of convection. SWA also presents the greatest conditional instability. To the authors' knowledge, this is the first time that the partition of total precipitation and its diurnal cycle by type of precipitating system over eastern Africa have been investigated together with the environmental conditions of the long-lived MCSs.

The convection-permitting simulation mimics the zonal distribution of continental precipitation well. It succeeds correctly partitioning precipitation among the different types of precipitating systems, with 50% of the total precipitation due to long-lived MCSs. The long-lived MCSs are also the main contributors to nocturnal precipitation over land. The latter is, however, underestimated. The lack of nighttime continental precipitation results from a systematic deficit in precipitation over SWA and CAF, which is compensated by an excess over ETH during the afternoon and early evening. This precipitation surplus over ETH comes from the afternoon triggering of too many long-lived MCSs. Over SWA, the deficit in precipitation is due to the reduced effective diameter and lifetime of the long-lived MCSs, which are one-third and half of what is observed, respectively. As SWA presents the greatest conditional instability, the long-lived MCSs are the most vigorous, with greater upward velocities and hydrometeor loading than over CAF or ETH. The strong AEJ and shear, well reproduced over SWA, appear not to be sufficient to sustain long-lived MCSs that are as large, fast and long as observed. We suggest that the reported wet bias around 3-km altitude over SWA would lead to the lack of organization of the long-lived MCSs. This wet bias may be explained by an incorrect location of the long-lived MCSs with respect to the AEWs. This would, in turn, cause the erroneous propagation of the long-lived MCSs, whose propagation direction presents a northward meridional component.

The simulation with parameterized convection fails to reproduce both the partition of precipitation and its diurnal cycle. Clouds other than DCCs are the first contributors to precipitation and the diurnal cycle peaks at 1500 LST, too early in the afternoon. This is due to the deep convection parameterization, which produces 70% of the total precipitation of the simulation, but the cloud content generated by the parameterization is not high enough to simulate the BT correctly (i.e., to simulate BT low enough to be included in the DCC category). A consequence is that the DCC contribution to the total precipitation, and its diurnal cycle, is too low. The remaining 30% of precipitation results from the explicit upward transport of humidity and its microphysical transformations. It shows a fairly negligible diurnal variability but still contributes to the increase in total precipitation during the evening and the night. The too early precipitation peak nevertheless represents an improvement with respect to the diurnal cycle of precipitation in global circulation models (Guichard et al. 2004). The simulation with parameterized convection is able to simulate long-lived MCSs, which are not generally produced by other models with convective parameterization, but they only contribute to one-third of precipitation and are too small, and have too low a zonal speed and too short a lifetime. They also present much lower vertical speeds and hydrometeor contents than in the convection-permitting simulation.

This study shows that the long-lived MCSs are the main contributors to precipitation over northern Africa from 9 to 14 June 2006. The convection-permitting simulation is successful in reproducing the precipitation partition, whereas the simulation with parameterized convection fails. This result highlights the added value gained by representing the convection explicitly. This study also shows that the convection is more organized over West Africa than over eastern Africa. The convection-permitting simulation fails to represent the zonal increase in organization and shows too many tracks of long-lived MCSs, a drawback also seen over West Africa with the convection-permitting Applications of Research to Operations at Mesoscale (AROME) model (Beucher et al. 2014). We suggest that this is the consequence of a wet anomaly around 3-km altitude. It is also possible that the lack of precipitation from the less-organized, long-lived MCSs prevents the drying of the atmosphere there. The excessive number of MCSs in convection-permitting simulations has been identified in other areas [i.e., over Brazil (Machado and Chaboureau 2015) and the southern United Kingdom (Hanley et al. 2015)]. These studies pointed out the sensitivity of MCS organization to the subgrid turbulence scheme. Finally, the conclusions drawn from this study are based on a specific 6-day case over a region that experiences very large seasonal changes as well as significant intraseasonal variability. It would be worthwhile to repeat the assessment made here for other cases or over longer periods in order to disentangle the role of the environment from the effect of some systematic model errors.

Acknowledgments. The research leading to these results has received funding from the European Union Seventh Framework Program (FP7/2007-2013) under Grant 603502 (EU project DACCIWA: Dynamics-aerosol-chemistry-cloud interactions in West Africa). Computer resources were allocated by GENCI through Project 90569. We thank the anonymous reviewers for their comments, which helped to improve the overall quality of the paper.

REFERENCES

Bayo Omotosho, J., 1985: The separate contributions of line squalls, thunderstorms and the monsoon to the total rainfall in Nigeria. *J. Climatol.*, **5**, 543–552, https://doi.org/10.1002/joc.3370050507.

Bechtold, P., E. Bazile, F. Guichard, P. Mascart, and E. Richard, 2001: A mass-flux convection scheme for regional and global models. *Quart. J. Roy. Meteor. Soc.*, **127**, 869–886, https://doi.org/10.1002/qj.49712757309.

Beucher, F., J.-P. Lafore, F. Karbou, and R. Roca, 2014: High-resolution prediction of a major convective period over West Africa. *Quart. J. Roy. Meteor. Soc.*, **140**, 1409–1425, https://doi.org/10.1002/qj.2225.

Chaboureau, J.-P., and P. Bechtold, 2005: Statistical representation of clouds in a regional model and the impact on the diurnal cycle of convection during Tropical Convection, Cirrus and Nitrogen Oxides (TROCCINOX). *J. Geophys. Res.*, **110**, D17103, https://doi.org/10.1029/2004JD005645.

——, P. Tulet, and C. Mari, 2007: Diurnal cycle of dust and cirrus over West Africa as seen from Meteosat Second Generation satellite and a regional forecast model. *Geophys. Res. Lett.*, **34**, L02822, https://doi.org/10.1029/2006GL027771.

——, and Coauthors, 2008: A midlatitude precipitating cloud database validated with satellite observations. *J. Appl. Meteor. Climatol.*, **47**, 1337–1353, https://doi.org/10.1175/2007JAMC1731.1.

——, and Coauthors, 2016: Fennec dust forecast intercomparison over the Sahara in June 2011. *Atmos. Chem. Phys.*, **16**, 6977–6995, https://doi.org/10.5194/acp-16-6977-2016.

Crumeyrolle, S., and Coauthors, 2011: Transport of dust particles from the Bodélé region to the monsoon layer—AMMA case study of the 9–14 June 2006 period. *Atmos. Chem. Phys.*, **11**, 479–494, https://doi.org/10.5194/acp-11-479-2011.

Cuxart, J., P. Bougeault, and J.-L. Redelsperger, 2000: A turbulence scheme allowing for mesoscale and large-eddy simulations. *Quart. J. Roy. Meteor. Soc.*, **126**, 1–30, https://doi.org/10.1002/qj.49712656202.

Fink, A. H., and A. Reiner, 2003: Spatiotemporal variability of the relation between African Easterly Waves and West African Squall Lines in 1998 and 1999. *J. Geophys. Res.*, **108**, 4332, https://doi.org/10.1029/2002JD002816.

——, D. G. Vincent, and V. Ermert, 2006: Rainfall types in the West African Sudanian Zone during the summer monsoon 2002. *Mon. Wea. Rev.*, **134**, 2143–2164, https://doi.org/10.1175/MWR3182.1.

Flamant, C., C. Lavaysse, M. Todd, J.-P. Chaboureau, and J. Pelon, 2009: Multi-platform observations of a representative springtime case of Bodélé and Sudan dust emission, transport and scavenging over West Africa. *Quart. J. Roy. Meteor. Soc.*, **135**, 413–430, https://doi.org/10.1002/qj.376.

Fouquart, Y., and B. Bonnel, 1986: Computations of solar heating of the Earth's atmosphere: A new parametrization. *Beitr. Phys. Atmos.*, **53**, 35–62.

Futyan, J. M., and A. D. Del Genio, 2007: Deep convective system evolution over Africa and the tropical Atlantic. *J. Climate*, **20**, 5041–5060, https://doi.org/10.1175/JCLI4297.1.

Goyens, C., D. Lauwaet, M. Schröder, M. Demuzere, and N. P. M. Van Lipzig, 2012: Tracking mesoscale convective systems in the Sahel: Relation between cloud parameters and precipitation. *Int. J. Climatol.*, **32**, 1921–1934, https://doi.org/10.1002/joc.2407.

Grini, A., P. Tulet, and L. Gomes, 2006: Dusty weather forecasts using the Méso-NH mesoscale atmospheric model. *J. Geophys. Res.*, **111**, D19205, https://doi.org/10.1029/2005JD007007.

Guichard, F., and Coauthors, 2004: Modelling the diurnal cycle of deep precipitating convection over land with cloud-resolving models and single-column models. *Quart. J. Roy. Meteor. Soc.*, **130**, 3139–3172, https://doi.org/10.1256/qj.03.145.

Hanley, K. E., R. S. Plant, T. H. M. Stein, R. J. Hogan, J. C. Nicol, H. W. Lean, C. Halliwell, and P. A. Clark, 2015: Mixing-length controls on high-resolution simulations of convective storms. *Quart. J. Roy. Meteor. Soc.*, **141**, 272–284, https://doi.org/10.1002/qj.2356.

Huffman, G. J., and Coauthors, 2007: The TRMM Multisatellite Precipitation Analysis (TMPA): Quasi-global, multiyear, combined-sensor precipitation estimates at fine scales. *J. Hydrometeor.*, **8**, 38–55, https://doi.org/10.1175/JHM560.1.

Janiga, M. A., and C. D. Thorncroft, 2014: Convection over tropical Africa and the east Atlantic during the West African Monsoon: Regional and diurnal variability. *J. Climate*, **27**, 4159–4188, https://doi.org/10.1175/JCLI-D-13-00449.1.

Janowiak, J. E., R. J. Joyce, and Y. Yarosh, 2001: A real-time global half-hourly pixel resolution infrared dataset and its applications. *Bull. Amer. Meteor. Soc.*, **82**, 205–217, https://doi.org/10.1175/1520-0477(2001)082<0205:ARTGHH>2.3.CO;2.

Lafore, J. P., and Coauthors, 1998: The Méso-NH Atmospheric Simulation System. Part I: Adiabatic formulation and control simulations. *Ann. Geophys.*, **16**, 90–109, https://doi.org/10.1007/s00585-997-0090-6.

Laing, A. G., R. Carbone, V. Levizzani, and J. Tuttle, 2008: The propagation and diurnal cycles of deep convection in northern tropical Africa. *Quart. J. Roy. Meteor. Soc.*, **134**, 93–109, https://doi.org/10.1002/qj.194.

Lemaître, C., C. Flamant, J. Cuesta, J.-C. Raut, P. Chazette, P. Formenti, and J. Pelon, 2010: Radiative heating rates profiles associated with a springtime case of Bodélé and Sudan dust transport over West Africa. *Atmos. Chem. Phys.*, **10**, 8131–8150, https://doi.org/10.5194/acp-10-8131-2010.

Machado, L. A. T., and J.-P. Chaboureau, 2015: Effect of turbulence parameterization on assessment of cloud organization. *Mon. Wea. Rev.*, **143**, 3246–3262, https://doi.org/10.1175/MWR-D-14-00393.1.

——, W. B. Rossow, R. L. Guedes, and A. W. Walker, 1998: Life cycle variations of mesoscale convective systems over the Americas. *Mon. Wea. Rev.*, **126**, 1630–1654, https://doi.org/10.1175/1520-0493(1998)126<1630:LCVOMC>2.0.CO;2.

Masson, V., and Coauthors, 2013: The SURFEXv7.2 land and ocean surface platform for coupled or offline simulation of earth surface variables and fluxes. *Geosci. Model Dev.*, **6**, 929–960, https://doi.org/10.5194/gmd-6-929-2013.

Mathon, V., H. Laurent, and T. Lebel, 2002: Mesoscale convective system rainfall in the Sahel. *J. Appl. Meteor.*, **41**, 1081–1092, https://doi.org/10.1175/1520-0450(2002)041<1081:MCSRIT>2.0.CO;2.

Mlawer, E. J., S. J. Taubman, P. D. Brown, M. J. Iacono, and S. A. Clough, 1997: Radiative transfer for inhomogeneous atmospheres: RRTM, a validated correlated-k model for the longwave. *J. Geophys. Res.*, **102**, 16 663–16 682, https://doi.org/10.1029/97JD00237.

Pantillon, F., P. Mascart, J.-P. Chaboureau, C. Lac, J. Escobar, and J. Duron, 2011: Seamless MESO-NH modeling over very large grids. *C. R. Mec.*, **339**, 136–140, https://doi.org/10.1016/j.crme.2010.12.002.

Pergaud, J., V. Masson, S. Malardel, and F. Couvreux, 2009: A parameterization of dry thermals and shallow cumuli for mesoscale numerical weather prediction. *Bound.-Layer Meteor.*, **132**, 83–106, https://doi.org/10.1007/s10546-009-9388-0.

Pinty, J.-P., and P. Jabouille, 1998: A mixed-phase cloud parameterization for use in a mesoscale non-hydrostatic model: Simulations of a squall line and of orographic precipitation. *Conf. on Cloud Physics*, Everett, WA, Amer. Meteor. Soc., 217–220.

Saunders, R., M. Matricardi, P. Brunel, S. English, P. Bauer, U. O'Keeffe, P. Francis, and P. Rayer, 2005: RTTOV-8 science and validation report. Tech. Rep., NWP SAF Rep., 41 pp.

Segele, Z. T., and P. J. Lamb, 2005: Characterization and variability of Kiremt rainy season over Ethiopia. *Meteor. Atmos. Phys.*, **89**, 153–180, https://doi.org/10.1007/s00703-005-0127-x.

Skamarock, W. C., 2004: Evaluating mesoscale NWP models using kinetic energy spectra. *Mon. Wea. Rev.*, **132**, 3019–3032, https://doi.org/10.1175/MWR2830.1.

Söhne, N., J.-P. Chaboureau, and F. Guichard, 2008: Verification of cloud cover forecast with satellite observation over West Africa. *Mon. Wea. Rev.*, **136**, 4421–4434, https://doi.org/10.1175/2008MWR2432.1.

Tian, B., B. J. Soden, and X. Wu,2004: Diurnal cycle of convection, clouds, and water vapor in the tropical upper troposphere: Satellites versus a general circulation model. *J. Geophys. Res.*, **109**, D10101, https://doi.org/10.1029/2003JD004117.

Tompkins, A. M., C. Cardinali, J.-J. Morcrette, and M. Rodwell, 2005: Influence of aerosol climatology on forecasts of the African Easterly Jet. *Geophys. Res. Lett.*, **32**, L10801, https://doi.org/10.1029/2004GL022189.

WMO, 2014: WMO guide to meteorological instruments and methods of observation. Part I: Measurement of meteorological variables. Tech. Rep. WMO-8, 1177 pp., https://library.wmo.int/opac/doc_num.php?explnum_id=4147.

Zhang, G., K. H. Cook, and E. K. Vizy, 2016: The diurnal cycle of warm season rainfall over West Africa. Part I: Observational analysis. *J. Climate*, **29**, 8423–8437, https://doi.org/10.1175/JCLI-D-15-0874.1.

Chapter 4

Radiative Impact of Dust on Mesoscale Convective Systems and their Organization in Northern Africa

Contents

4.1 Introduction

The radiative effect of dust on precipitation and mesoscale convective systems (MCSs) during the dust episode of 9-14 June 2006 is analyzed in this chapter. To investigate how dust affects the distribution of precipitation among cloud categories in northern Africa, the same methodology for cloud identification used in chapter 3 is applied here to satellite observations and two convection-permitting simulations, one accounting for the dust-radiation interaction (DUST), the other not (NODUST). The DUST (NODUST) simulation was referred to as HiRes (HiNod) in chapters 2 and 3 (in chapter 2). The aim of this chapter is to determine the changes that dust radiatively induces on the northern African atmosphere, and to investigate the changes on the precipitation and the convective organization. Special attention is given to the long-lived MCSs (i.e., with BT lower than 230 K, an effective diameter larger than 120 km and a lifetime of at least 6 hours) because, as shown in chapter 3, they are the first contributors to precipitation, producing 55% of the total rainfall. The long-lived MCSs are investigated in the three continental sub-regions presented in chapter 3, Ethiopia (ETH), Central Africa (CAF) and southern West Africa (SWA).

An assessment of the simulated dust against satellite and ground observations shows that the simulation accounting for dust distributes dust correctly, with the greatest optical depths over the Sahara and northern parts of SWA, in a thick layer between 3 and 5-km altitude. There, a mid-level heating of 1.3 K in average is found due to the absorption of radiation in the shortwave by the dust. This warming modifies the meridional gradient of temperature and is at the origin of the acceleration of the African easterly jet (AEJ) by 1-2 m s^{-1} over SWA. Furthermore, a cooling of 0.3-0.9 K and a moistening of more than 1 g kg^{-1} are found in the lowest km of the atmosphere. This temperature decrease is due to two mechanisms: a reduction of the radiation intensity reaching the ground, and an enhancement of the monsoon flow in West Africa. The enhanced monsoon flow explains both the moistening in the near-surface and the reported northward migration of the Intertropical Discontinuity. The latter is accompanied by an increase in precipitation in regions further north in the simulation with dust compared to the simulation without dust.

The increase in the vertical gradient of the temperature leads to a stabilization of the lower atmosphere in the simulation with dust, which leads to a reduction of the number of long-lived MCSs over SWA. When accounting for dust, the number of long-lived MCSs is one third of the number without dust. As a consequence, the precipitation over SWA is largely diminished. The long-lived MCSs become, however, longer-lived, faster and more efficient in precipitation production in the simulation with dust because of two factors: on the one hand, a larger reservoir of convective available potential energy is found; on the other hand, the intensification of the AEJ induces a larger vertical low-level wind shear, a dynamical mechanism that favors the organization of convection.

These results are presented in the article reproduced in section 4.2. The article is published in *Monthly Weather Review*.

4.2 Article

Precipitation and Mesoscale Convective Systems: Radiative Impact of Dust over Northern Africa

IRENE REINARES MARTÍNEZ AND JEAN-PIERRE CHABOUREAU

Laboratoire d'Aérologie, Université de Toulouse, CNRS, UPS, Toulouse, France

(Manuscript received 20 March 2018, in final form 18 July 2018)

ABSTRACT

The radiative effect of dust on precipitation and mesoscale convective systems (MCSs) is examined during a case of dust emission and transport from 9 to 14 June 2006 over northern Africa. The same method to identify and track different cloud types is applied to satellite observations and two convection-permitting simulations (with grid mesh of 2.5 km), with and without the radiative effect of dust, performed with the MesoNH model. The MCSs produce most of the observed total precipitation (66%), and the long-lived systems (lasting 6 h or more) are responsible for 55% of the total. Both simulations reproduce the observed distribution of precipitation between the cloud categories but differ due to the radiative effects of dust. The overall impacts of dust are a warming of the midtroposphere; a cooling of the near surface, primarily in the western parts of northern Africa; and a decrease in precipitation due to a too-low number of long-lived MCSs. The drop in their number is due to the stabilization of the lower atmosphere, which inhibits the triggering of convection. The long-lived MCSs are a little longer lived, faster, and more efficient in rainfall production when accounting for the dust–radiation interaction. This higher degree of organization is due to the larger convective available potential energy and an intensified African easterly jet. The latter is, in turn, a response to the variation in the meridional gradient of the temperature induced by the dust.

1. Introduction

Dust aerosols are recognized as having an important radiative effect on the atmosphere, notably over northern Africa, which has the largest sources of dust in the world (Engelstaedter et al. 2006). Dust aerosols scatter and absorb solar radiation and absorb and re-emit terrestrial radiation; this is the direct effect. Aerosol absorption has been shown to heat the air (Lemaître et al. 2010) and cool the near surface by decreasing the solar radiation reaching the ground (Helmert et al. 2007). This leads to an increase in the low-level static stability (Tulet et al. 2008) and can modify the occurrence of cloud formation. These variations in temperature can, in turn, generate a dynamical response that brings the atmosphere to a new equilibrium, as well as changing the cloudiness and precipitation (the semidirect effect). Using the European Centre for Medium-Range Weather Forecasts (ECMWF) Integrated Forecast System (IFS) model, Tompkins et al. (2005) found an enhancement in the African easterly jet (AEJ; a midlevel thermal wind modulated by the meridional gradient of temperature between the Gulf of Guinea and the Sahara) at the 5-day range when using a monthly climatology for dust instead of an annual mean. In addition, Chaboureau et al. (2007) showed an improvement in cloud cover over West Africa when using a prognostic dust scheme rather than a climatology. This highlights the importance of the description of dust in numerical models to correctly represent the weather in Africa. Nevertheless, the radiative effects of dust on the processes controlling precipitation remain largely unknown.

During the summertime, convective systems account for most of the precipitation in northern Africa (Janiga and Thorncroft 2014). In particular, large convective storms that become organized, mesoscale convective systems (MCSs), have been shown to generate up to 90% of the total precipitation in the Sahel (Mathon et al. 2002). Reinares Martínez and Chaboureau (2018) studied a dust outbreak from 9 to 14 June 2006 over northern Africa, which was previously documented by Flamant et al. (2009). They focused on the characteristics of long-lived MCSs (i.e., with a lifetime of at least 6 h) and on the environmental conditions where they develop and found that the long-lived MCSs produce

---

Corresponding author: Dr. Irene Reinares Martínez, irene.reinares@aero.obs-mip.fr

DOI: 10.1175/MWR-D-18-0103.1

55% of the total precipitation. A convection-permitting simulation with a resolution of 2.5 km was able to capture the degree of organization of the long-lived MCSs better than a run performed at a 20-km resolution using a parameterization of the convection. Moreover, this organization was found to be highly controlled by the AEJ-induced low-level wind shear and to increase from east to west.

The aim of this paper is to examine the dynamical responses of the atmosphere to the radiative effect of dust and to analyze the changes induced in the precipitation. The radiative impact of dust on the organization of convection is also examined. This issue, to the best of the authors' knowledge, has not yet been addressed. To achieve this objective, we use the convection-permitting simulation described in Reinares Martínez and Chaboureau (2018) and a second convection-permitting simulation set up in the same manner, except with the radiative impact of the dust turned off. The simulation allowing the dust–radiation interaction includes schemes that account for the dust emission, transport, and deposition because simulating these processes is vital to represent the interaction of dust particles with radiation (Pérez et al. 2006; Chaboureau et al. 2007). During the period from 9 to 14 June 2006, dust was extensively emitted over northern Africa. The dust particles emitted from eastern sources in Chad and Sudan were then transported over West Africa (Flamant et al. 2009), where a large ensemble of airborne instruments allowed the analysis of the size distribution of the dust particles (Crumeyrolle et al. 2011) and of the radiative properties of the dust plumes, which were found to generate concomitant heating (Lemaître et al. 2010).

The remainder of the paper is organized as follows. The datasets and the method used to attribute rain to MCSs and to track them, which are described in detail in Reinares Martínez and Chaboureau (2018), are reviewed in section 2. The evaluation of the simulated dust, compared to the observations, is presented in section 3. The atmospheric responses to both the direct and semidirect dust radiative effects are discussed in section 4. In particular, it is shown that dust barely affects the relative contribution of different precipitating systems to the total rainfall over northern Africa. The impact on the MCSs and their precipitation production are analyzed in section 5. Finally, the conclusions are given in section 6.

2. Data and method

a. Model and observations

Two simulations, NODUST and DUST [the latter called HiRes in Reinares Martínez and Chaboureau (2018)], are performed with the anelastic, nonhydrostatic model MesoNH (Lafore et al. 1998; Lac et al. 2018) version 5–1-3. Both simulations are convection permitting with a 2.5-km horizontal grid spacing, 72 vertical levels up to a height of 30 km, and a vertical grid spacing between 60 and 600 m. The two simulations are run over a large domain of 3840 × 7680 km^2 (Fig. 1), which permits the representation of the dust emissions in Chad and Sudan and its transport (Flamant et al. 2009). The two simulations use approximately a third of a billion grid points. They are run from 0000 UTC 9 June to 0000 UTC 15 June 2006, with outputs every 3 h and initial and boundary conditions provided by the ECMWF operational analyses.

Both simulations share the same parameterizations, differing only in that DUST accounts for the radiative effect of dust. The surface fluxes are represented by the Surface Externalisée (SURFEX) scheme (Masson et al. 2013) in which natural land surfaces are handled by the Interaction between Soil, Biosphere, and Atmosphere (ISBA) scheme (Noilhan and Planton 1989). Both simulations use a 1.5-order closure scheme for the turbulence (Cuxart et al. 2000) and a parameterization of the dry thermals and shallow cumuli (Pergaud et al. 2009). In addition, they include a microphysical scheme for mixed-phase clouds (Pinty and Jabouille 1998), a subgrid statistical cloud scheme (Chaboureau and Bechtold 2005), the Rapid Radiative Transfer Model (Mlawer et al. 1997) for longwave radiation, and the two-stream scheme by Fouquart and Bonnel (1980) for shortwave radiation.

The dust prognostic scheme is described in Grini et al. (2006). It includes the Dust Entrainment and Deposition (DEAD) scheme (Zender et al. 2003), to which MesoNH provides the wind speed at a height of 10 m, the soil moisture, and the roughness length. Dust is mobilized following Marticorena and Bergametti (1995) via a combination of saltation and sandblasting processes, and the horizontal flux of the dust particles can be computed. The vertical flux of the dust aerosols that will be injected into the atmosphere is calculated as the ratio of the horizontal flux and a sandblasting efficiency coefficient, which depends on the clay content of the soil. Once in the atmosphere, the time and space evolution of the dust is simulated in the Organic and Inorganic Lognormal Aerosols Model (ORILAM) scheme (Tulet et al. 2005). ORILAM considers three dust modes with a lognormal size distribution. Initially, the size distributions have median diameters of 0.078, 0.64, and 5.0 μm and standard deviations of 1.75, 1.76, and 1.70 μm, respectively, as defined by Crumeyrolle et al. (2011). Finally, dust can undergo dry sedimentation and wet deposition to return to the surface. Regarding the

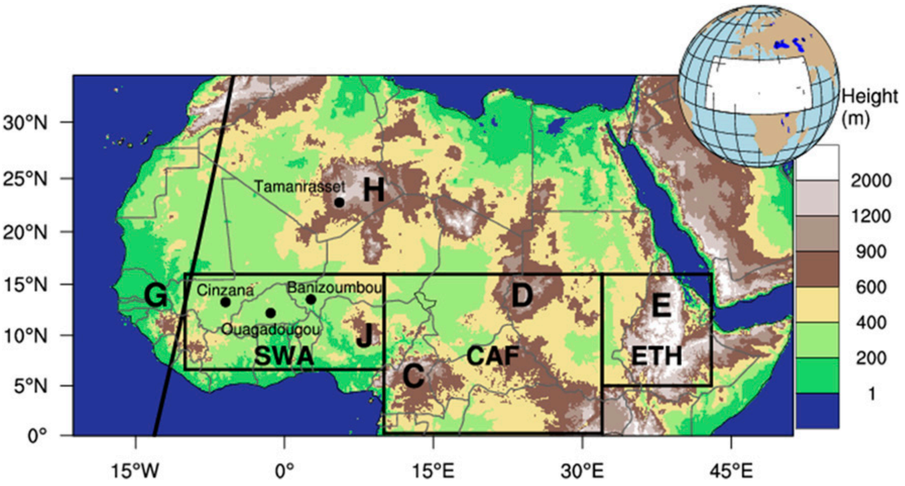

FIG. 1. Domain of simulation and analysis. In color is the altitude. Topographic features are the Guinea highlands (G), the Hoggar Mountains (H), the Jos Plateau (J), the Cameroon highlands (C), the Darfur Plateau (D), and the Ethiopian highlands (E). The black dots represent the location of the AERONET stations of Cinzana, Ouagadougou, Banizoumbou, and Tamanrasset analyzed in Fig. 2, and the black line represents the *CALIPSO* cross section of Fig. 4.

shortwave effect, the refractive indexes are 1.44800–0.00292*i* for wavelengths below 690 nm, 1.44023–0.00116*i* for wavelengths between 690 and 1190 nm, and 1.41163–0.00106*i* for wavelengths larger than 1190 nm. For the absorption and re-emission of longwave radiation by dust, the standard formulation taken from the ECMWF model is used (Tulet et al. 2008). This formulation consists of adding a fraction of the aerosol optical depth to the longwave optical depth for CO_2 and H_2O.

Two observation datasets are used to assess clouds and precipitation in the simulations: the Climate Prediction Center (CPC) globally merged 4-km-resolution brightness temperature (BT; Janowiak et al. 2001), merged using all available geostationary satellites, and the Tropical Rainfall Measuring Mission (TRMM) 3B42 version 7 3-hourly rainfall (Huffman et al. 2007), available in 0.25° spatial resolution. Cloud systems are defined in terms of BT at 10.8 μm (see section 2b), and the 3-hourly accumulated precipitation is associated with the cloud systems. From the model outputs, synthetic BTs corresponding to the Meteosat Second Generation (MSG) observations are computed offline using the Radiative Transfer for TIROS Operational Vertical Sounder (RTTOV) code version 8.7 (Saunders et al. 2005), following the method developed by Chaboureau et al. (2008). The gridded BT data ease the comparison with the model outputs, while the temporal sampling of the TRMM 3B42 product is convenient for the analysis of the diurnal cycle of precipitation, a feature that results in the TRMM 3B42 product being widely employed (e.g., Janiga and Thorncroft 2014; Zhang et al. 2016).

For the dust assessment, the aerosol optical depth (AOD) is provided on a 1° × 1° regular latitude–longitude grid by Deep Blue collection version 6 from retrievals of the Moderate Resolution Imaging Spectroradiometer (MODIS; Hsu et al. 2004) on board the *Aqua* spacecraft. *Aqua* passes from south to north across the equator at approximately 1330 LT. The AOD is based on observations in the visible and ultraviolet spectra. The Deep Blue algorithm is convenient because it estimates the AOD over bright surfaces, such as the Sahara Desert, where dust emissions and concentrations are large.

The dust evaluation also takes advantage of the Aerosol Robotic Network (AERONET) sun photometers (Holben et al. 1998) at stations in Cinzana, Ouagadougou, Banizoumbou, and Tamanrasset. The sun photometers provide the aerosol properties with a time resolution of 15 min during the daytime. Here, we use the Ångström coefficient obtained from the 440- and 870-nm wavelengths and the AOD product at 440 nm, a wavelength that lies within one of the three spectral windows (the one centered at 532 nm) associated with the refractive indexes considered in DUST. The use of both MODIS Deep Blue and AERONET is convenient, because MODIS provides the regional distribution of the AOD in northern Africa, and the AERONET high-frequency local measurements allow the temporal characterization of the AOD. Note, however, that both products account for the AOD due to all types of aerosols, whereas the AOD computed in MesoNH is exclusively due to dust.

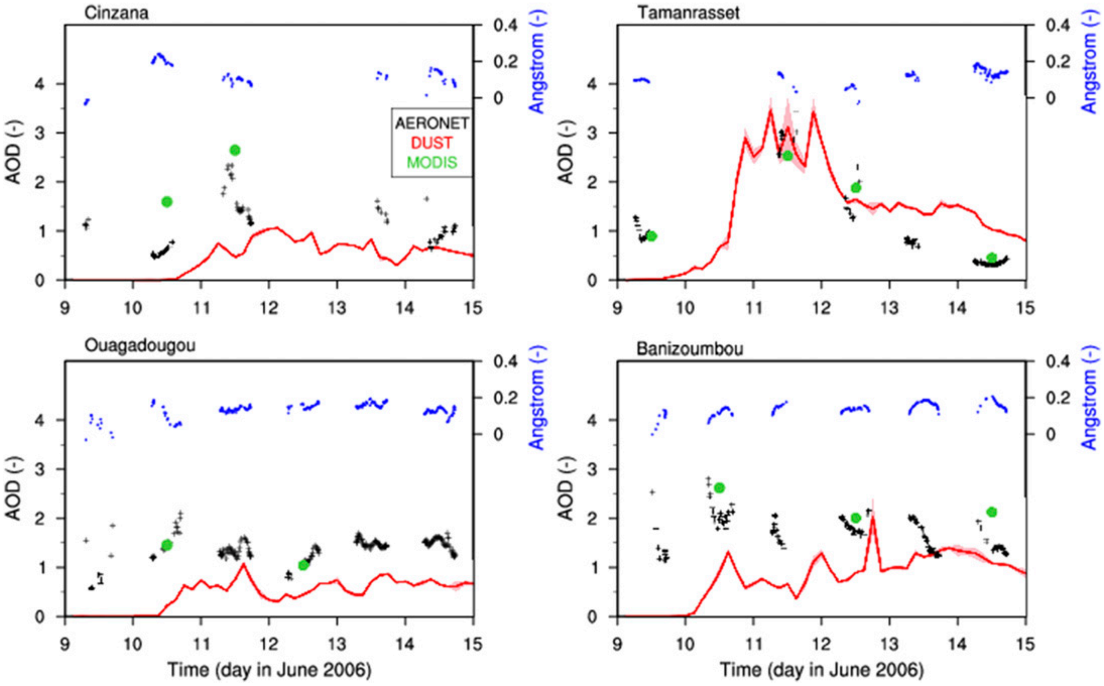

FIG. 2. Temporal evolution of the (left axis) AOD at 440 nm measured at the AERONET stations of Cinzana, Ouagadougou, Banizoumbou, and Tamanrasset (black crosses), measured by MODIS (green dots), and computed from the DUST simulation over a square of $0.3° \times 0.3°$ centered on the stations (red lines). The red-shaded contours correspond to the standard deviation of the simulated AOD values inside the squares. The Ångström coefficients (blue dots) are obtained from the 440- and 870-nm wavelengths at the sun photometers. The locations of the four stations are shown in Fig. 1.

This difference in aerosol type does not affect the conclusion because, as will be shown in Fig. 2, the Ångström coefficient values are small. This indicates a large particle size, and therefore that mineral dust was the predominant aerosol present over West Africa during the 9–14 June 2006 period.

To further assess the vertical distribution of dust, the backscatter coefficient at 532 nm from CALIOP on board *CALIPSO* (Winker et al. 2009) is employed. The CALIOP lidar provides observations during both the day and night. It has a very high sampling resolution, 30 and 335 m in the vertical and horizontal directions, respectively, but a poor temporal sampling of the same areas, with a 16-day repeat cycle due to its narrow swath. The CALIOP-derived product used here is only available after 13 June 2006. The simulated backscatter coefficients to be directly compared to the observed signals are computed in DUST with a lidar simulator integrated in the model. The latter computes the total backscatter coefficient from Rayleigh and Mie scattering, taking into account all the scattering particles predicted in the model, including dust, and following the assumptions made about their particle distribution and optical properties (Chaboureau et al. 2011).

b. Tracking of MCSs

The methodology used to attribute precipitation to cloud systems and to track MCSs is detailed in Reinares Martínez and Chaboureau (2018) and is briefly reviewed here. Two cloud categories are established: deep convective clouds (DCCs) with BT less than 230 K and cirrus anvil clouds (CACs) with BT ranging between 230 and 260 K, to which the 3-hourly accumulated precipitation is attributed. For the observed clouds, the precipitation is taken from TRMM. In the BT distribution for DUST and NODUST, high (low) values of BT are more frequent (infrequent) than in the observations; therefore, the BT thresholds are adapted to the simulations such that each cloud category is equally represented over the 6-day period for the three datasets. Therefore, for both DUST and NODUST, the thresholds become 243 and 266 K.

The DCC and CAC grid points sharing a common face are then aggregated into clusters. For each DCC cluster, vertical profiles of the thermodynamic variables are computed in the volume obtained when vertically projecting the envelope of the cluster. The variables are computed both at the time of detection and 6 h before at the same location to examine the characteristics of these DCCs and of the environment, respectively. For the observed DCC clusters, these profiles are extracted from the analyses and forecasts of the ECMWF, both with 6-h resolution, starting at 0000 and 0300 UTC, respectively.

The DCCs are then tracked through time using geographical overlapping, with a surface overlapping ratio of 20%. The tracking is done only on DCC clusters with an effective diameter (the diameter of a circle with the same area as the cluster) larger than 120 km to ensure realistic trajectories despite the 3-h temporal lag between consecutive images. These tracked DCCs are called MCSs, and the others are called small DCCs. Finally, the MCSs are divided into long-lived MCSs (i.e., those that last at least 6 h) and short-lived MCSs (i.e., those that last less than 6 h). As in Reinares Martínez and Chaboureau (2018), three subregions covering the continental rainband are considered [Fig. 1; southern West Africa (SWA), central Africa (CAF), and Ethiopia (ETH)], with the aim of examining how dust radiatively impacts precipitation in each subregion.

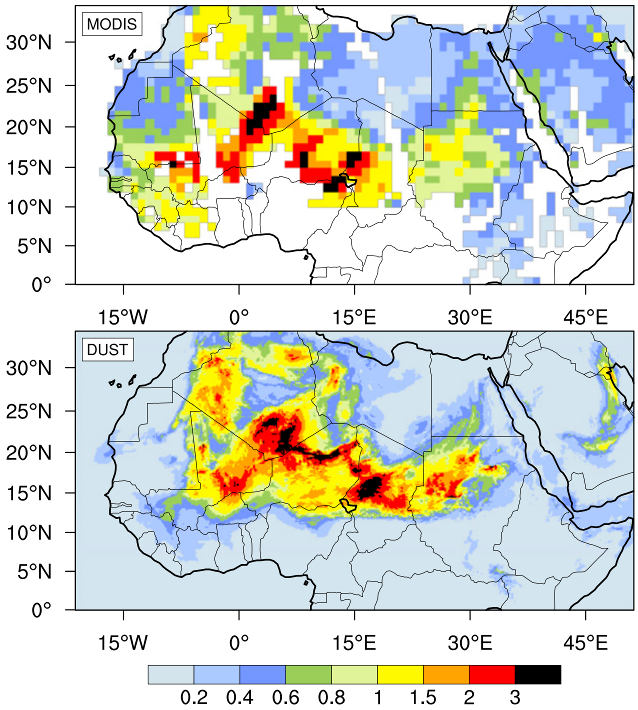

FIG. 3. AOD on 11 Jun 2006 for MODIS crossing the equator at 1330 UTC and for DUST at 1200 UTC. White areas indicate that no data are available.

3. Assessment of dust

a. *Time evolution at the AERONET stations*

The time series of the simulated AODs and those measured at 440 nm by AERONET from 9 to 14 June over four stations are shown in Fig. 2, together with the corresponding MODIS values and the 440–870-nm Ångström coefficient from AERONET. The stations at Cinzana, Ouagadougou, and Banizoumbou are located in SWA, while the station at Tamanrasset is located in the Sahara (their locations are depicted in Fig. 1). The Ångström coefficient defines the spectral dependence of the AOD and provides information on the size of the particles that attenuate the radiation. The larger the Ångström coefficient, the smaller the particles. The Ångström coefficient has values below 0.25 at Cinzana and Banizoumbou and values below 0.2 at Ouagadougou and Tamanrasset during the entire studied period. This corresponds well to the values below 0.4 measured on 13 June 2006 along 2°E from 10° to 13°N between the stations of Ouagadougou and Banizoumbou (Crumeyrolle et al. 2011). In general, pure large dust has Ångström coefficient values of less than 0.4. Therefore, we can conclude that the values of AOD measured during this period are predominantly due to dust.

Among the AERONET stations, Cinzana records the lowest mean AOD value, approximately 1.11, due to its southwesternmost location, which places it the farthest from the dust-source regions. At Ouagadougou and Tamanrasset, the mean AOD values are very similar (1.30 and 1.31, respectively); however, while Ouagadougou has a rather flat series of values, a strong peak with a value larger than 3 is observed at Tamanrasset on 11 June. Note that an AOD of 3 indicates that the intensity of the radiation arriving at the sun photometer is only 5% of the incoming solar radiation at 440 nm. Banizoumbou records the largest mean AOD value of 1.67; this station benefits from the transport pattern of dust from eastern sources. Using back trajectories, Flamant et al. (2009) showed that the AOD measured at Banizoumbou is due to dust that was emitted in Bodélé 2–3 days before, this source being active from 9 to 11 June. The AOD values for MODIS, when available, are largely consistent with those measured at the AERONET stations. The existing discrepancies may arise from the direct comparison of the coarse resolution (1° × 1°) of the MODIS product to the local characteristics of the sun photometer retrievals. The AOD values are generally underestimated by the model at the southern stations (Cinzana, Ouagadougou, and Banizoumbou). However, at Tamanrasset, the observed intense AOD peak is very well captured by DUST with values of approximately 3. On 13 and 14 June, the simulated AOD values are overestimated. This is due to an extensive convective cold pool that developed at the border between southern Algeria and Mali in DUST (not shown).

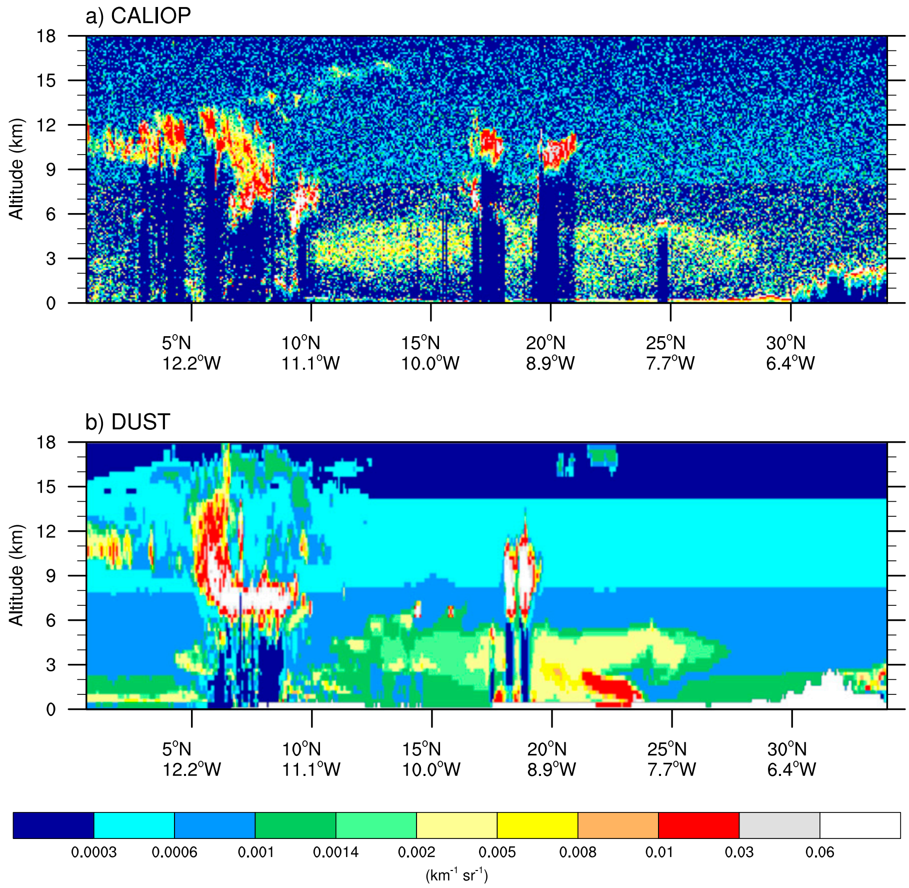

FIG. 4. Vertical cross section of the total backscatter coefficient at 532 nm on 14 Jun 2006 from (a) CALIOP at approximately 0200 UTC and (b) DUST at 0000 UTC. Its location is shown in Fig. 1.

b. Spatial distribution of dust

The horizontal distribution of AOD is shown for MODIS and DUST on 11 June 2006 (Fig. 3), when the AOD had its largest values over West Africa. East of 15°E, the observed values of AOD larger than 1 are explained by the emissions over the eastern sources described by Flamant et al. (2009). They suggested that the emitted dust, mobilized by the Harmattan, reaches higher altitudes when passing above the monsoon flow at the ITD, being then transported within the AEJ over West Africa. West of 15°E, dust is redistributed into the Saharan air layer (SAL) or sub-Saharan regions. The pattern of AOD values larger than 3 over southern Algeria corresponds to the AOD peak at Tamanrasset (Fig. 2). This peak and the pattern of the large AOD values (e.g., larger than 2) is explained by the arrival of the southerly sector of an African easterly wave that perturbed the mean flow of the AEJ (not shown) and transported the dust from the mean axis of the AEJ farther north, up to 25°N. Retrievals of AOD are lacking near the Guinean coast due to the persistence of monsoonal clouds there. Both SWA and CAF have values of AOD larger than 2 north of 12°N. In ETH, the AOD values are negligible because the emissions of the previous days occurred downstream of the AEJ. In the DUST simulation, the observed distribution and values of AOD are generally well reproduced, both over the source regions and over West Africa. In the simulation, the AOD also reaches values larger than 2 in SWA and CAF; however, in SWA, the AOD is underestimated over the Ivory Coast and southern Mali. Indeed, the simulated AOD is lower than the observed values in the continental regions west of 10°W.

Figure 4 shows the vertical cross section of the total backscatter coefficient on 14 June 2006 retrieved by CALIOP at approximately 0200 UTC and obtained for DUST at 0000 UTC (only two CALIOP nighttime cross sections are available over West Africa during the studied period). The radiation at 532 nm strongly interacts with large particles such as clouds and dust via Mie scattering. In the absence of large particles, Rayleigh scattering is dominant throughout the atmosphere and becomes larger with decreasing altitude as

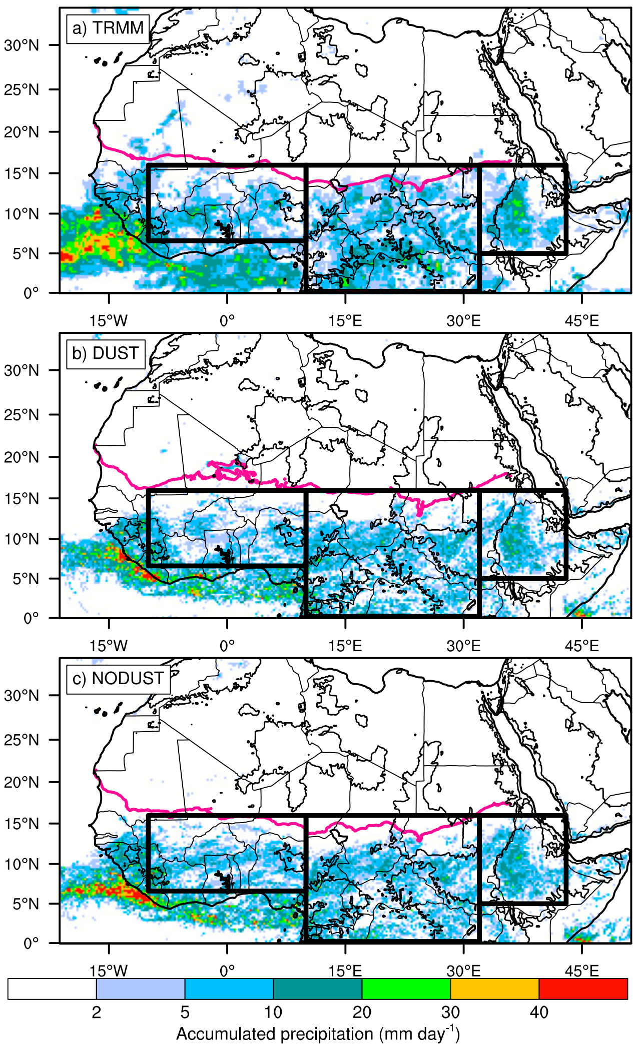

FIG. 5. Accumulated precipitation between 9 and 14 Jun 2006 for (a) TRMM, (b) DUST, and (c) NODUST. The pink line represents the mean position of the ITD, defined following Chaboureau et al. (2016). The solid black lines represent the orography at an altitude of 600 m, and the black boxes delimit the three subregions.

the concentration of air molecules increases. For CALIOP, backscatter coefficient values larger than $10^{-2}\,\mathrm{km}^{-1}\,\mathrm{sr}^{-1}$ correspond to high-level clouds south of 10°N and near 15° and 20°N. Between 25° and 30°N, these large values may be related to dust emissions. A dust plume, characterized by backscatter coefficient values between 10^{-3} and $10^{-2}\,\mathrm{km}^{-1}\,\mathrm{sr}^{-1}$, is located between 10° and 28°N above the residual boundary layer and extends up to 6 km, to the altitude of the SAL. High clouds south of 10°N are well located in DUST and span the same range of altitudes as observed. DUST reproduces the vertical extent and meridional location of the dust plume well.

To assess the dust, the simulated optical depth and backscatter coefficient were compared to the AERONET measurements and MODIS retrievals and the CALIOP observations, respectively. Good agreement is found for the regional distribution of the dust and its vertical stratification, and the DUST simulation is able to capture the entire range of the observed AOD values. Therefore, the DUST simulation is sufficiently realistic to address the radiative effects of dust on the atmosphere.

4. Impact of dust on the atmosphere

a. Distribution of precipitation

The accumulated precipitation is shown in Fig. 5 for the TRMM observations and the two simulations. The mean position of the intertropical discontinuity (ITD) is superimposed. It is defined as the continental zone where the water vapor mixing ratio at the surface is equal to $10\,\mathrm{g\,kg}^{-1}$ (taken from the ECMWF analysis) that corresponds to 14°C dewpoint temperature, following Chaboureau et al. (2016). Precipitation is observed from the eastern Atlantic to the Ethiopian highlands south of 15°N. Over the ocean, the highest precipitation values are located offshore the coasts of Guinea and Sierra Leone. Over the continent, precipitation primarily lies within the subregions of SWA, CAF, and ETH. In these subregions, the highest precipitation values are observed to the western side of the Jos Plateau and over the mountain-devoid areas of Burkina Faso and the Ivory Coast, in the foothills of the Darfur Plateau and Cameroon Mountains, and over the Ethiopian highlands, respectively. In the ECMWF analysis, the ITD is located at around 15°N from the western coast to Sudan and reaches farther north in SWA than in CAF.

Both DUST and NODUST reproduce the observed distribution of precipitation. There are, however, several differences from the observations, especially over the coastal regions and the eastern Atlantic, where the meridional extent of the precipitation is reduced in the simulations. Over land, the precipitation has slightly lower values than those observed over the Darfur Plateau and the Cameroon Mountains. In terms of continental precipitation, the two simulations differ the most over SWA, where DUST produces less precipitation than NODUST. The position of the ITD varies between the two simulations over SWA and CAF. There, it reaches higher latitudes for DUST, suggesting differences in the regional circulations between the simulations.

The partition of the total precipitation into different cloud categories (Fig. 6) is performed by associating the 3-hourly accumulated precipitation, with the clusters corresponding to each cloud category. The long-lived MCSs are the primary precipitation producers, being

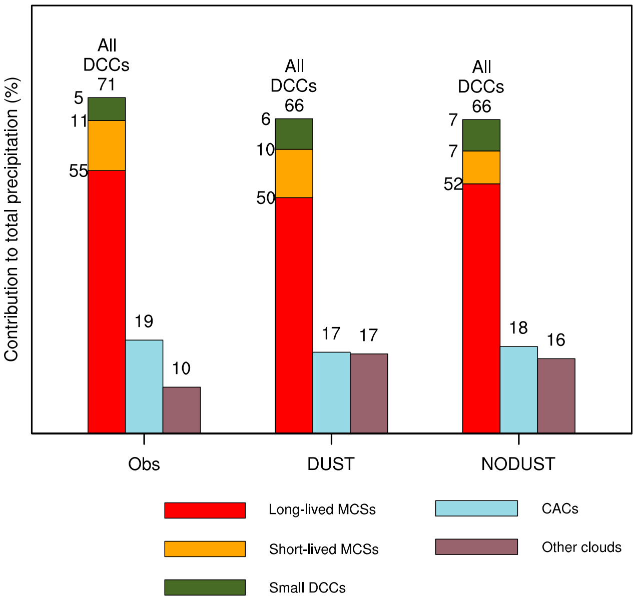

FIG. 6. Contribution of all the DCCs (long-lived and short-lived MCSs and small DCCs), CACs, and clouds other than DCCs or CACs to the total precipitation over the simulation domain between 9 and 14 Jun 2006 for the observations and the simulations.

responsible for 55% of the observed total precipitation. This contribution, as well as those from short-lived MCSs (11%) and small DCCs (5%), is part of the precipitation due to all DCCs (71%). The rest (29%) is due to clouds other than DCCs. DUST and NODUST reproduce this distribution well, especially for the major precipitation producers, with 50% and 52% of precipitation due to long-lived MCSs, respectively, and 66% due to all DCCs for both simulations. Overall, the relative contribution of different cloud types to precipitation is impacted little by the dust–radiation interaction. We further investigate how the atmosphere is modified and the implications for the net rainfall production by the long-lived MCSs, which explain the largest part of precipitation.

b. *Temperature and modulation of the AEJ and the monsoon flow*

The vertical structure of the temperature is expected to vary under the effect of dust, primarily due to the latter's vertical layering and radiative properties that lead to an attenuation of the incoming radiation. The AEJ is a thermal wind [i.e., its (zonal) wind speed changes with altitude proportionally to the temperature change with latitude]; therefore, the AEJ should also be impacted by the radiative effect of dust. To analyze the modulation of the AEJ with dust, we examine the mean values of the temperature and wind speed for DUST and NODUST. In addition, we examine these quantities from the ECMWF analyses to compare to the simulated variables in terms of their magnitude, although we assume that errors can be associated to the analysis, partly due to the scarcity of observations in the region. In Fig. 7, the left panel shows the wind speed at 600 hPa, the level where the speed of the AEJ is maximum. The AEJ is located near 12°N and corresponds to wind speeds larger than 10 m $\mathrm{s^{-1}}$ extending from ETH to SWA. In the ECMWF analyses, the AEJ core has speeds larger than 16 m $\mathrm{s^{-1}}$ and extends meridionally from 8° to 14°N and zonally from 15°W to 15°E. In the two simulations, the meridional extent of the AEJ is well captured; however, its zonal extent is slightly reduced, compared to that in the ECMWF analyses. The AEJ core is the least intense for NODUST, especially over SWA. The right panel in Fig. 7 shows the vertical structure of the potential temperature and the wind speed across latitude, both averaged between 10°W and 10°E, corresponding to the limits of SWA, where the AOD and the speed of the AEJ are the largest. In the ECMWF analyses, the potential temperature has a pronounced gradient at the surface that increases from 298 K at the equator in the Gulf of Guinea to 314 K between 20° and 25°N in the Sahara. The high surface temperature and associated sensible fluxes over the Sahara generate strong vertical mixing, resulting in a thick Saharan boundary layer characterized by a low vertical gradient of the potential temperature. This gradient is much larger over the Gulf of Guinea. As a consequence, from the surface to approximately 4-km altitude, the potential temperature increases with latitude and decreases with latitude above. This leads to an increase in the wind speed with height until an altitude of 4 km, where the AEJ reaches its maximum speed, and then a decrease beyond that. Near 4-km altitude and 12°N, the AEJ has a speed of 17 m $\mathrm{s^{-1}}$. In the simulations, the potential temperature between the altitudes of 3 and 5 km and north of 10°N differs with respect to the ECMWF analyses. In DUST (NODUST), the atmosphere is warmer (cooler) there. Accordingly, the strength and altitude of the AEJ also differ. The overall effect is an AEJ that is enhanced and slightly higher in altitude (~ 500 m) in DUST and an AEJ that is lessened (1–2 m $\mathrm{s^{-1}}$) and lower in altitude (~ 100 m) in NODUST with respect to the ECMWF analyses.

The radiative impact of dust on the temperature and wind speed is further investigated over SWA. The vertical cross section of the difference in the temperature and wind speed between DUST and NODUST is shown in Fig. 8. The difference in the water vapor mixing ratio, as well as the dust extinction for DUST, is also shown. At the top of the dense dust plume (at an altitude of 5 km), the extinction coefficient is 0.06 $\mathrm{km^{-1}}$, which

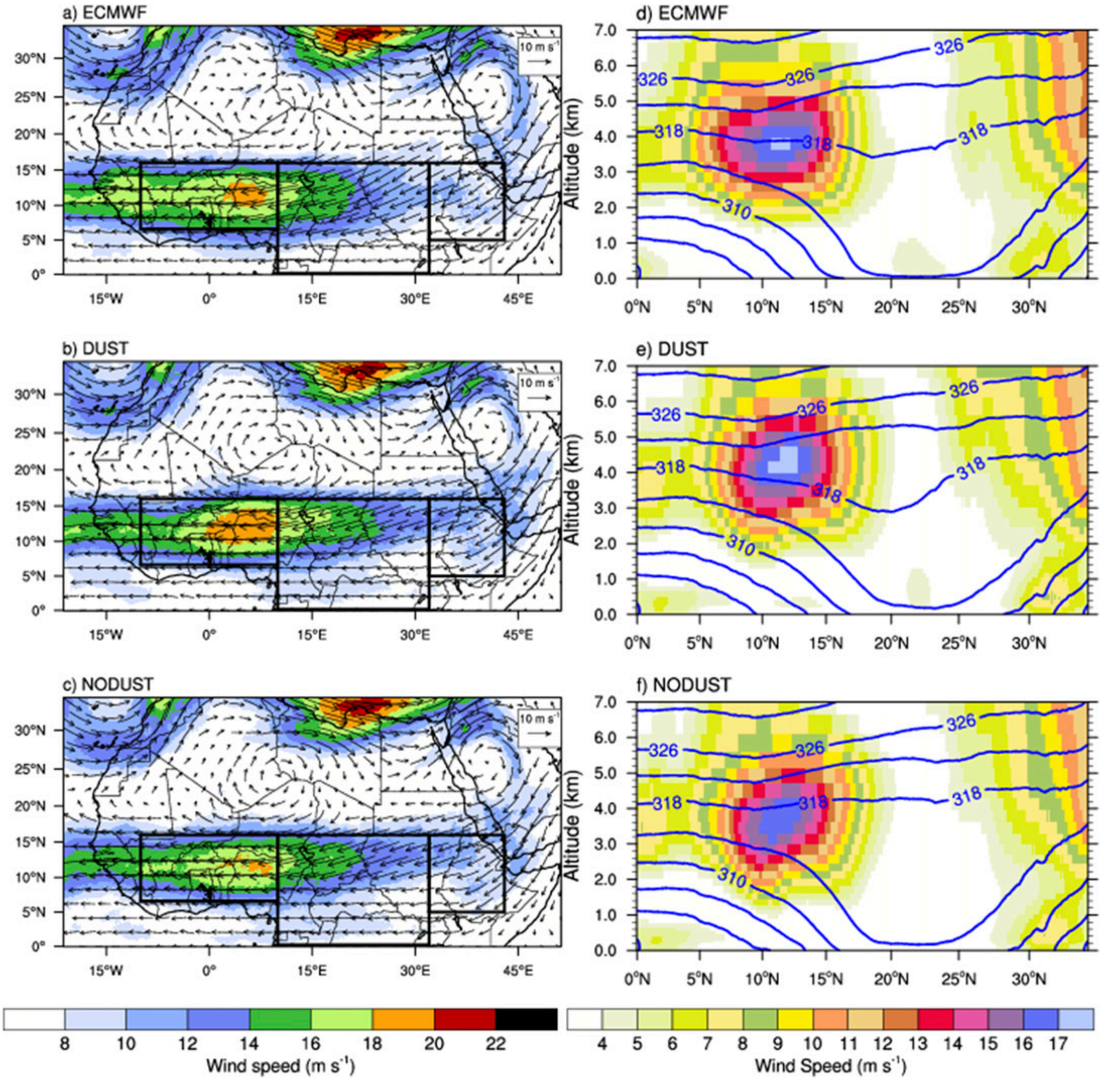

FIG. 7. (left) Wind speed at 600 hPa for (a) ECMWF, (b) DUST, and (c) NODUST. (right) Potential temperature (blue lines every 4 K) and wind speed (colors) averaged between 10°W and 10°E for (d) ECMWF, (e) DUST, and (f) NODUST. The fields are averaged over the period of 9–14 Jun 2006.

quickly drops to near zero at higher levels in the absence of dust. The obtained value of 0.06 km^{-1}, averaged zonally and in time in DUST, is consistent with the value of 0.05 km^{-1} derived from airborne lidar measurements at the top of the dust layer on 13 and 14 June 2006 (Lemaître et al. 2010). A net increase of more than 1.3 K during the 6-day period is found for DUST at altitudes of 3–5 km. This increase is consistent with the average warming of 1.5–4 K found by Lemaître et al. (2010). These values are larger because they are estimated during the daytime, when the shortwave absorption by dust and the consequent increase in the temperature occur. The decrease in potential temperature by 0.3–0.9 K north of 12°N for DUST with respect to NODUST may be explained through two mechanisms: first, a reduction in the intensity of the radiation arriving at the near surface because of the dust absorption aloft; and second, an enhanced cold monsoon flow, in agreement with the mean position of the ITD, which is displaced northward in DUST with respect to NODUST, as seen from Fig. 5. Midlevel warming and surface cooling are also found over CAF and ETH but with much lower temperature variations (not shown).

The change in the horizontal and vertical gradients of the potential temperature impacts the wind speed considerably. The increase in the wind speed when accounting for dust is as large as 2 $\mathrm{m\,s^{-1}}$ at an altitude of 5 km between 9° and 15°N, corresponding to the modulation of the AEJ. A moistening occurs in DUST below the warmed midlevel layer, with an increase in the water vapor mixing ratio of more than 1 $\mathrm{g\,kg^{-1}}$ in the lowest 2 km, concomitant with the decrease in potential temperature.

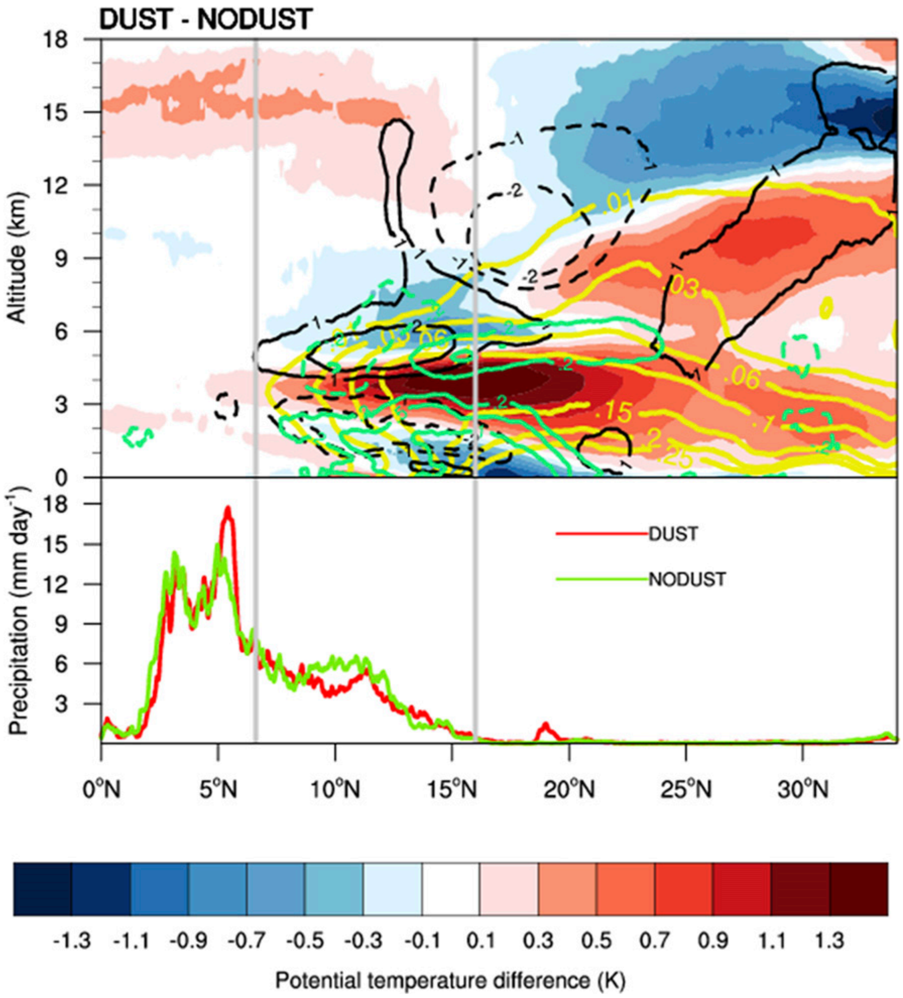

FIG. 8. (top) Altitude–latitude cross section of the 6-day mean difference in θ (K), wind speed (m s^{-1}; black isocontours), and water vapor mixing ratio (g kg^{-1}; blue–green isocontours) between DUST and NODUST. The yellow isocontours represent the mean dust extinction (km^{-1}) coefficient in DUST and correspond to values of 0.01, 0.03, 0.06, 0.1, 0.15, 0.2, and 0.25. All the variables are averaged between 10°W and 10°E, the longitudinal limits of SWA. The gray lines depict the meridional limits of SWA. (bottom) The 6-day mean precipitation between 10°W and 10°E.

Finally, precipitation in DUST diminishes with respect to NODUST near 10°N in SWA, but slightly increases near 20°N, as also seen in Fig. 5.

The relationship between the cooling of the low atmosphere and the monsoon flow is further analyzed. The temporal evolution of the potential temperature at the surface, precipitation, and mean position of the ITD for DUST and NODUST over SWA is shown in Fig. 9. The AOD is also presented for DUST. Both the potential temperature and the ITD experience a strong diurnal variation, as the monsoon flow intensifies during the night and morning hours, penetrating farther north, when turbulent fluxes in the boundary layer are much reduced. For example, on 9 June, potential temperature at 15°N decreases from 304 to 300 K from 0600 to 1200 UTC in both DUST and NODUST, and the ITD reaches its northernmost diurnal position slightly before 1200 UTC. The latter retreats southward from 1200 to 1800 UTC, accompanied by an increase in temperature. These diurnal variations appear for both simulations during the whole period. They are, however, less pronounced for DUST after 11 June. From that day onward, the ITD shows a northward migration from around 15°N on 9/10 June to 19°N by 15 June, whereas the ITD remains at 15°N for NODUST during the 6-day period. For DUST, this northward march is time related with the increase in AOD over West Africa, and particularly over the northern parts of SWA, where AOD reaches values above 1 from 11 June onward. Differences in potential temperature between DUST and NODUST

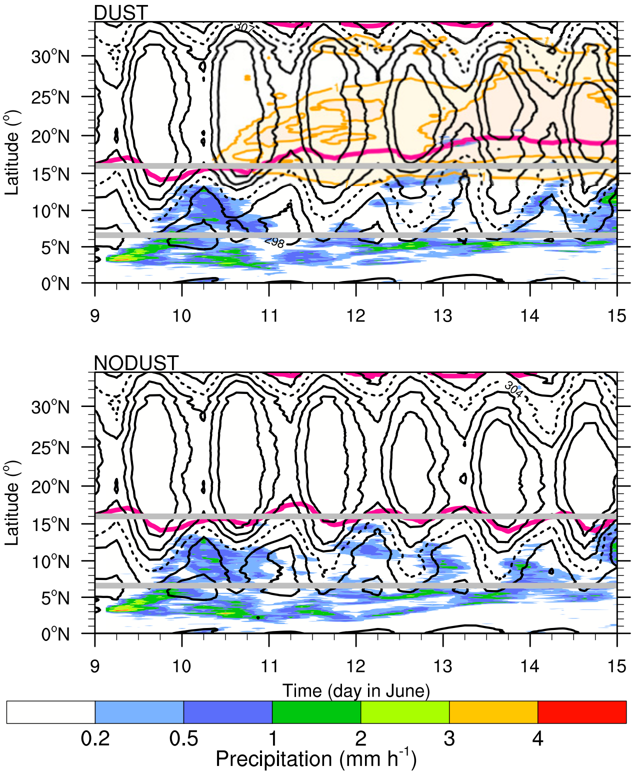

FIG. 9. Latitude–time diagrams for (top) DUST and (bottom) NODUST of the position of the ITD (pink), the total precipitation (shaded colors), the potential temperature at the surface (black lines), and the AOD (orange lines and shades; only for DUST). The values of the isotherms are 298, 301, 304 (dashed), 307, 310, and 313 K, and the isocontours of AOD are 1.0 and 1.5. All the variables are averaged between 10°W and 10°E, the longitudinal limits of SWA. The gray lines depict the meridional limits of SWA.

occur, with the greatest values on 13 and 14 June. North of 12°N, there is cooling for DUST. For example, at 0600 UTC 13 June, the potential temperature for DUST at 15°N is 301 K, whereas for NODUST, it is 303 K. Over the Sahara, between 20° and 25°N, cooling is also evident. These 2 days correspond with the ITD reaching 19°N, its northernmost position, when the AOD is larger than 1.5 for DUST. As a consequence, the monsoon flow plays an important role in the near-surface cooling under the radiative effect of dust and in transporting moisture farther north for DUST. This increased moisture explains precipitation appearing farther inland for DUST than for NODUST. The precipitation pattern near 20°N between 0000 and 0600 UTC for DUST is produced by a long-lived MCS (not shown) and may further favor the displacement of the ITD through its convective cold pool; this type of convection–ITD interaction has been previously reported (Flamant et al. 2007).

In summary, the temperature variations in the presence of dust, which are the largest over SWA, lead to an enhancement of the AEJ and monsoon flow and to the stabilization of the low atmosphere. As shown below, the latter changes the nature of the convective activity and ultimately explains the reported decrease in precipitation.

c. *CAPE and CIN*

Convective available potential energy (CAPE) and convective inhibition (CIN) are two variables commonly used to characterize the conditions that are favorable for moist convection. We analyze the most unstable CAPE and its associated CIN because these variables respond to changes in the vertical profiles of the atmosphere. For the three subregions, the bidimensional histograms of the individual values of CAPE and CIN are shown for the two simulations in Fig. 10. First, large regional differences in the shapes of the distributions are found between ETH and the other two subregions, regardless of the simulation. The values of CAPE are much lower in ETH (below 1000 J kg^{-1}) than in SWA or CAF (between 1000 and 2000 J kg^{-1}). Second, differences between DUST and NODUST are found primarily for SWA and CAF. In SWA, there are fewer grid points with values of CAPE lower than 600 J kg^{-1} for DUST than for NODUST; however, larger values between 1000 and 2000 J kg^{-1} occur more frequently. The larger values of CAPE occur for the entire range of CIN values, from 0 to 15 J kg^{-1}. To have access to CAPE, an air parcel must have a vertical wind speed greater than 1.4 m s^{-1} below the level of free convection to overcome a CIN of 1 J kg^{-1}. Thus, values of CIN greater than 1 J kg^{-1} lead to an inhibition of convection, because updrafts do not generally have vertical wind speeds large enough in the lower levels of the atmosphere to overcome such values of CIN. Therefore, the lower part of the joint distribution is more representative of convection. The number of grid points with a CIN lower than 1 J kg^{-1} and a CAPE lower than 1000 J kg^{-1} represents 6% of the total in DUST and 8% of the total in NODUST. This means that the triggering of weak convection is expected to occur more frequently for NODUST than for DUST. Conversely, 17% of the grid points for DUST and 14% of the grid points for NODUST have CIN values lower than 1 J kg^{-1} and CAPE values between 1000 and 2000 J kg^{-1}. This argument holds for both SWA and CAF, where convection will likely be more intense for DUST than for NODUST. Grid points with values of CIN likely to permit convection have higher values of CAPE.

5. Impact of dust on long-lived MCSs

a. *Precipitation and propagation*

The impact of dust on the precipitation produced by long-lived MCSs is investigated because they contribute

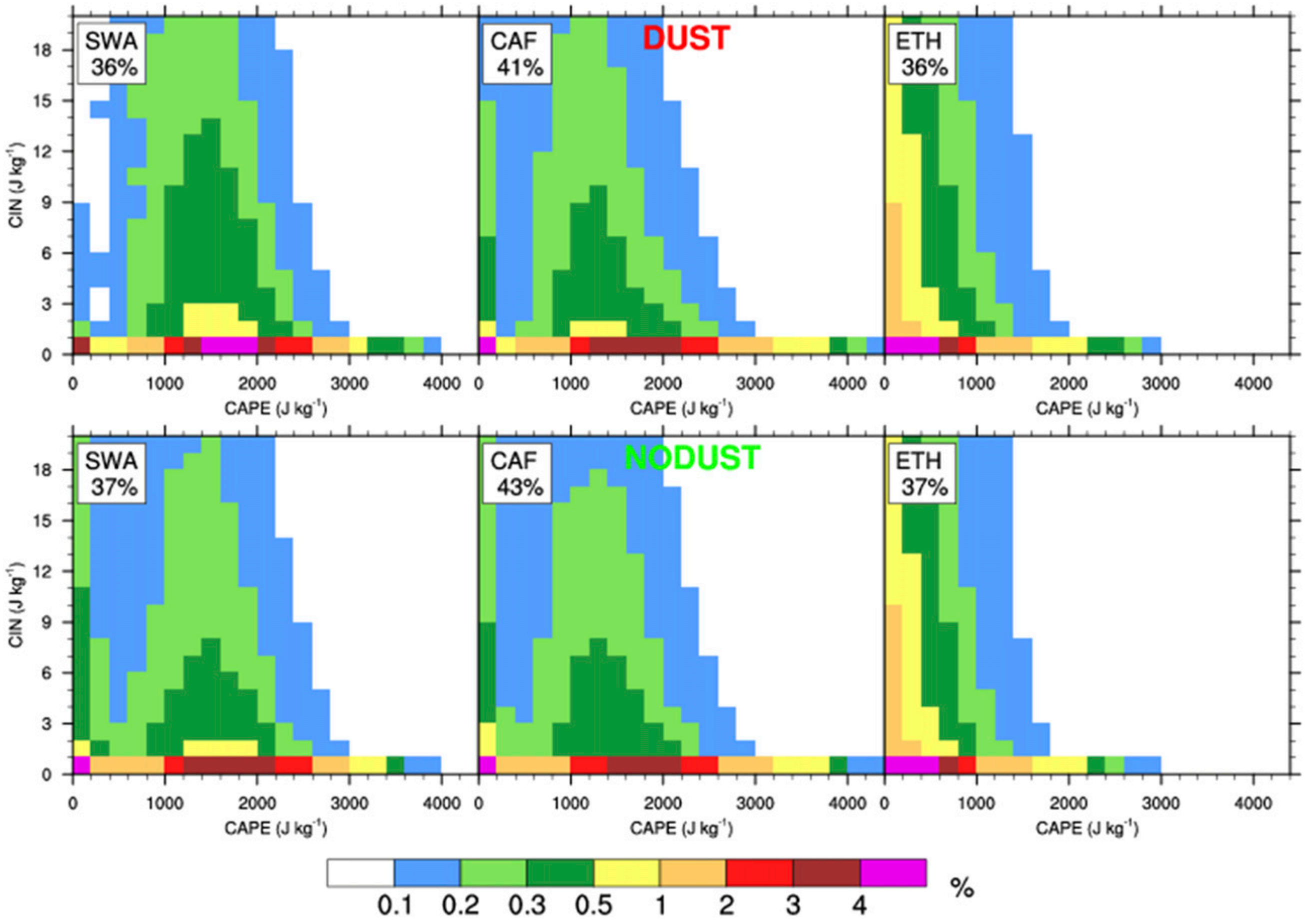

FIG. 10. Bidimensional histograms of CAPE and CIN for (top) DUST and (bottom) NODUST and for (left) SWA, (middle) CAF, and (right) ETH. The grid points with CAPE or CIN equal to 0 J kg^{-1} and those with CIN larger than 20 J kg^{-1} were discarded. The number in the label indicates the percentage of the grid points remaining.

to more than half of the total accumulated rainfall. The difference in precipitation between DUST and NODUST is shown in Fig. 11. The insert represents the difference in the total precipitation and in the precipitation due to long-lived MCSs for each subregion. Overall, DUST produces 10% less precipitation than NODUST. Changes in precipitation over the eastern Atlantic suggest a northward shift of the intertropical convergence zone, which is consistent with the northward displacement of the monsoon over land. Continental precipitation accounts for 39% of the 10% drop in DUST. SWA is the subregion contributing the most to this precipitation decrease over land. This is explained by the long-lived MCSs. Indeed, in SWA, the negative values of the rain difference appear spatially as elongated strips, corresponding to southwestward-propagating long-lived MCSs, which is consistent with the trajectories shown in Fig. 12 below. Over CAF and ETH, the negative values are distributed in a more fragmented manner, and the decrease in the rainfall is due to precipitating systems other than long-lived MCSs. The latter produce nearly the same amount of precipitation in DUST and NODUST over CAF and ETH.

These long-lived MCSs propagate westward in both the observations and the simulations (Fig. 12). Over the continent, they tend to be detected for the first time over the Ethiopian highlands in ETH, in the fringes of the Darfur Plateau and Cameroon highlands in CAF, and near the Jos Plateau and Guinea highlands in SWA. In SWA, several trajectories of long-lived MCSs also start over the plains west of the Jos Plateau, especially for NODUST, which generally has a much larger number of long-lived MCSs (101) than those observed (62) or simulated by DUST (84). The difference in the number of long-lived MCSs between DUST and NODUST is more pronounced over SWA and is related to the stabilization of the low-level atmosphere in DUST as a consequence of the midlevel warming and near-surface cooling when accounting for dust.

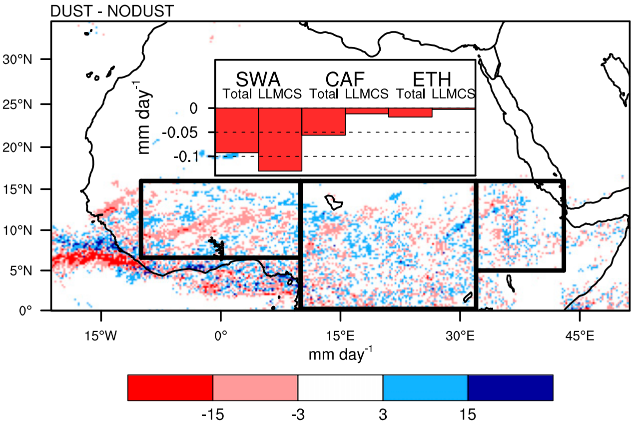

FIG. 11. Difference in the accumulated precipitation between DUST and NODUST. The inset shows the difference in the total precipitation and the precipitation due to long-lived MCSs over SWA, CAF, and ETH.

The number, size, and propagation characteristics of the observed and simulated long-lived MCSs are further investigated for the three subregions (Fig. 13). Each long-lived MCS is assigned to the subregion where it spends most of its lifetime, and the mean zonal speed of each long-lived MCS is calculated from the locations of its center of mass at its first and last detections. The observed long-lived MCSs increase their effective diameters, lifetimes, precipitation intensities, and zonal speeds from east to west. They are the most organized and fastest over SWA. There, they have a mean diameter of 600 km, a lifetime of approximately 20 h, and a precipitation rate of more than 1000 mm h^{-1}. Finally, their zonal propagation speed is 18 m s^{-1}.

For DUST and NODUST, these characteristics are poorly represented over SWA. The most pronounced differences with respect to the observations over SWA are the effective diameter and lifetime of the long-lived MCSs, which are half the observed values. Moreover, the long-lived MCSs are too slow, and the precipitation production is less than half the observed values. As a result, the increase in the degree of organization of the long-lived MCSs from ETH to SWA is not fully represented by DUST.

For NODUST, long-lived MCSs over SWA are slower (by 3 m s^{-1}), shorter lived (by 2 h), and less efficient in precipitation production (by 50 mm h^{-1}) than for DUST. The most striking result is the number of long-lived MCSs, which is much larger (3 times more). This explains why, for DUST, precipitation is generally suppressed over SWA, as shown in Fig. 11. For DUST, the less-frequent triggering of convection over SWA may lead to an excess of CAPE, compared to NODUST. This larger stock of potential energy could allow long-lived MCSs to be more organized (larger, longer lived, and individually more precipitating) in DUST than in NODUST. The significantly reduced number of long-lived MCSs drives the total precipitation drop in DUST.

b. *Environmental conditions*

The environmental characteristics of the long-lived MCSs 6 h before their detection are shown in Fig. 14 for the ECMWF analyses and the 3-h forecasts and for the two simulations over the three subregions. These characteristics are examined to understand the drivers of the regional differences in the long-lived MCSs for each dataset and how they are linked to the differences in precipitation production between DUST and NODUST.

For the observed long-lived MCSs, moisture taken from the ECMWF analysis and forecasts is greatest close to the surface and decreases quickly with height in all subregions. At the surface, the water vapor mixing ratio is the largest over SWA (16 g kg^{-1}), compared to CAF (15.5 g kg^{-1}) and ETH (14 g kg^{-1}). The vertical gradient of the equivalent temperature θ_e is the most pronounced over SWA as well, with a variation of approximately 24 K from the surface (353 K) to an altitude of approximately 4 km (329 K), indicating that the conditional instability is the largest there. This is consistent with the long-lived MCSs being more organized and more highly precipitating over SWA than over CAF or ETH.

The speed of the AEJ, whose core is located near an altitude of 4 km, increases from east to west, from ETH (8 m s^{-1}) to SWA (16 m s^{-1}), in agreement with the westward enhancement of the propagation speed of the long-lived MCSs (Fig. 13). Therefore, the vertical wind shear that is established due to the AEJ and the low-level south–southwesterly monsoon flow also strengthens over SWA, which helps the long-lived MCSs become more organized there, compared to CAF or ETH.

Both DUST and NODUST simulate the westward increase in the near-surface moisture, the vertical gradient of θ_e, and the speed of the AEJ (and associated low-level wind shear) well. The profiles of the water vapor mixing ratio and θ_e over CAF and ETH are nearly identical for the two simulations. Over SWA, both the water vapor mixing ratio and θ_e are larger for DUST than for NODUST up to an altitude of 4 km. For example, at a height of 2 km, DUST is 1 g kg^{-1} wetter and 3 K warmer. The presence of dust acts to stabilize the lower atmosphere in DUST. In turn, this more stable atmosphere acts to block the entrainment of the surrounding dry air (Parker 2002). The 1-K difference in θ_e near the surface is consistent with the tendency of DUST to have higher values of CAPE, compared to NODUST. Over SWA, the profiles of the wind speed show an AEJ that is located ~500 m higher for DUST than for NODUST, which is consistent with

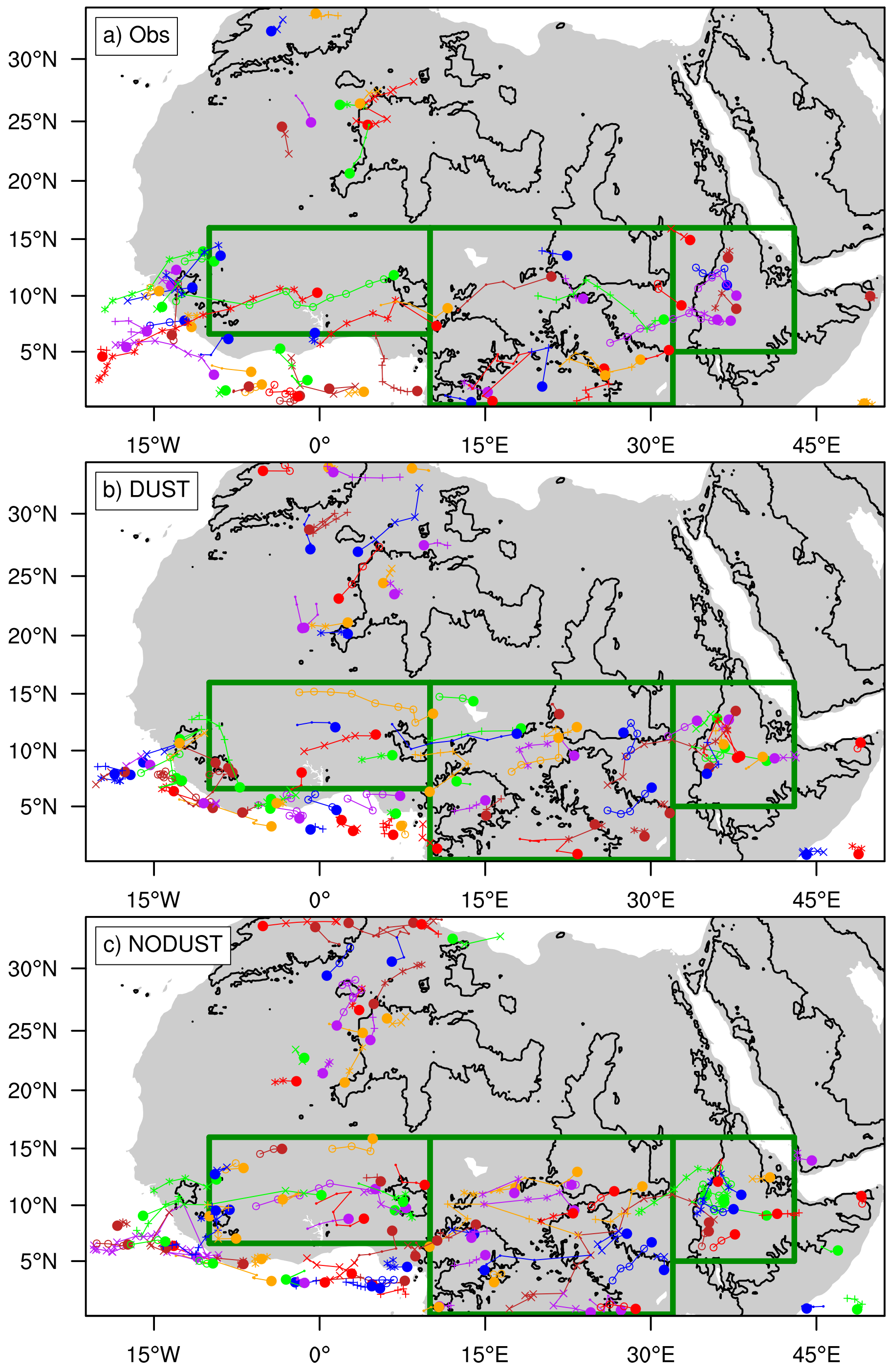

FIG. 12. Trajectories of long-lived MCSs (lifetime of 6 h or more) for (a) the observations, (b) DUST, and (c) NODUST. The dots represent the first detection of each long-lived MCS. The solid black lines represent the orography at an altitude of 600 m.

Fig. 7, and an enhanced monsoon flow, in agreement with Figs. 8 and 9.

c. *Properties of the long-lived MCSs*

The profiles of different properties related to the convective activity inside the long-lived MCSs are investigated at the time of detection (Fig. 15). For both simulations, liquid hydrometeors are present up to the freezing level, at approximately 3–4 km, with a drastic reduction at higher altitudes. A small amount of supercooled water is present up to 7 km, before the cloud droplets freeze completely. The solid hydrometeor content

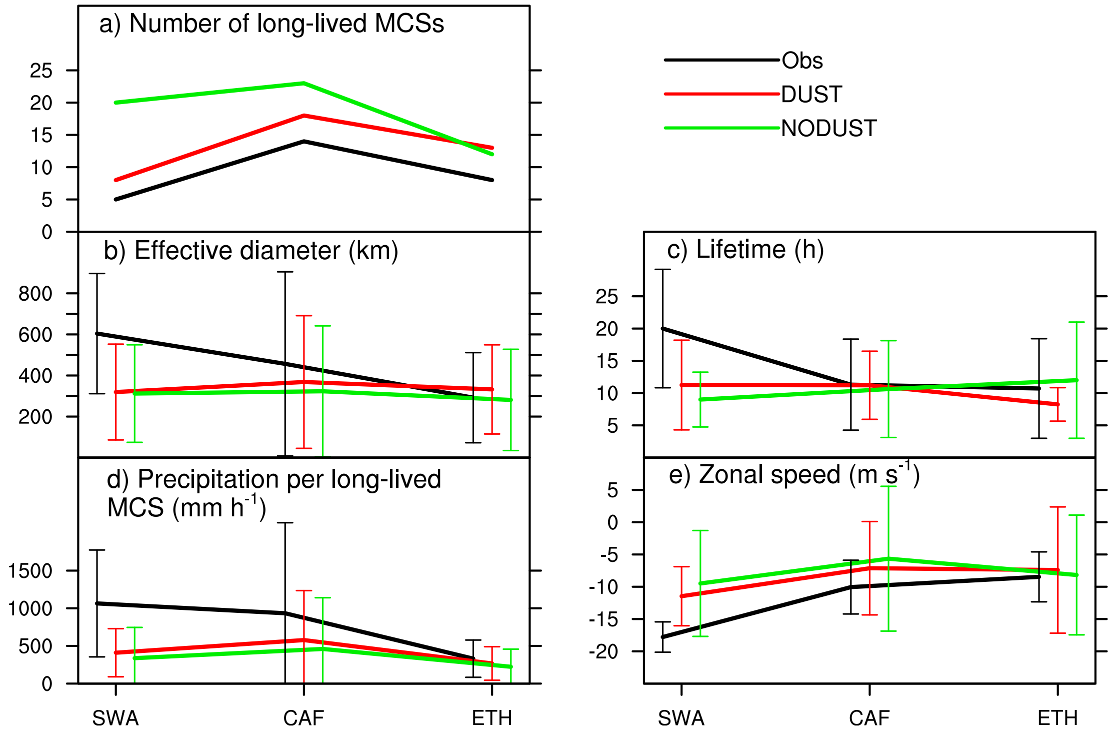

FIG. 13. Characteristics of long-lived MCSs by subregion (SWA, CAF, and ETH) for the observations and the simulations: (a) number of long-lived MCSs, (b) effective diameter, (c) lifetime, (d) precipitation per long-lived MCS, and (e) zonal speed. (b)–(e) Solid lines represent the mean values, and the error bars represent the standard deviation.

increases above the freezing level and reaches a maximum at approximately 9 km. The 99th percentile of the upward speed has its largest values between 6 and 9 km. The freezing of the liquid particles and deposition of water vapor releases large amounts of latent heat. This renders the air parcels more buoyant, which, in turn, increases their upward velocities inside the updrafts. In the near surface, the drop in θ_e between the time of the detection of the long-lived MCSs and 6 h before their occurrence is usually a signature of cold pools because the convective downdrafts generated by the evaporative cooling of raindrops transport dry and cold air down to the surface.

Some regional differences in the profiles are evident. Over SWA and CAF, both the hydrometeor loading and the upward velocities are reported to be larger than those over ETH because there is more convective instability (consistent with the distributions of CAPE in Fig. 10). This has an impact on the vertical development of the long-lived MCSs as well. Over SWA and CAF, the freezing level and maximum upward speeds are 1 km higher than those over ETH. In addition, the hydrometeor content extends to higher altitudes, up to 17 km. For both simulations, θ_e decreases near the surface in the 6 h prior to convection in all subregions. This decrease becomes more pronounced from ETH to SWA, from approximately 4 to 9 K, indicating that the most intense cold pools occur in SWA.

The profiles also vary between DUST and NODUST. The velocity of the updrafts inside the long-lived MCSs, as well as the hydrometeor content, is larger for DUST in the three subregions. One explanation is that the stabilization of the atmosphere (Fig. 8) results in a larger convective instability for DUST. One consequence of such a stabilization for DUST could be less-diluted updrafts. In terms of the drop in θ_e, DUST and NODUST differ the most over SWA (1 K over the lowest 3 km). This is consistent with the enhanced convection and propagation speeds of the long-lived MCSs there.

6. Conclusions

The radiative impact of dust on precipitation and MCSs over northern Africa is addressed for the period from 9 to 14 June 2006 with the use of two convection-permitting simulations, one accounting for the radiative effect of dust and the other neglecting this effect. The simulations are evaluated in terms of cloud category and precipitation using satellite observations. To analyze the radiative impact of dust, precipitation is attributed to

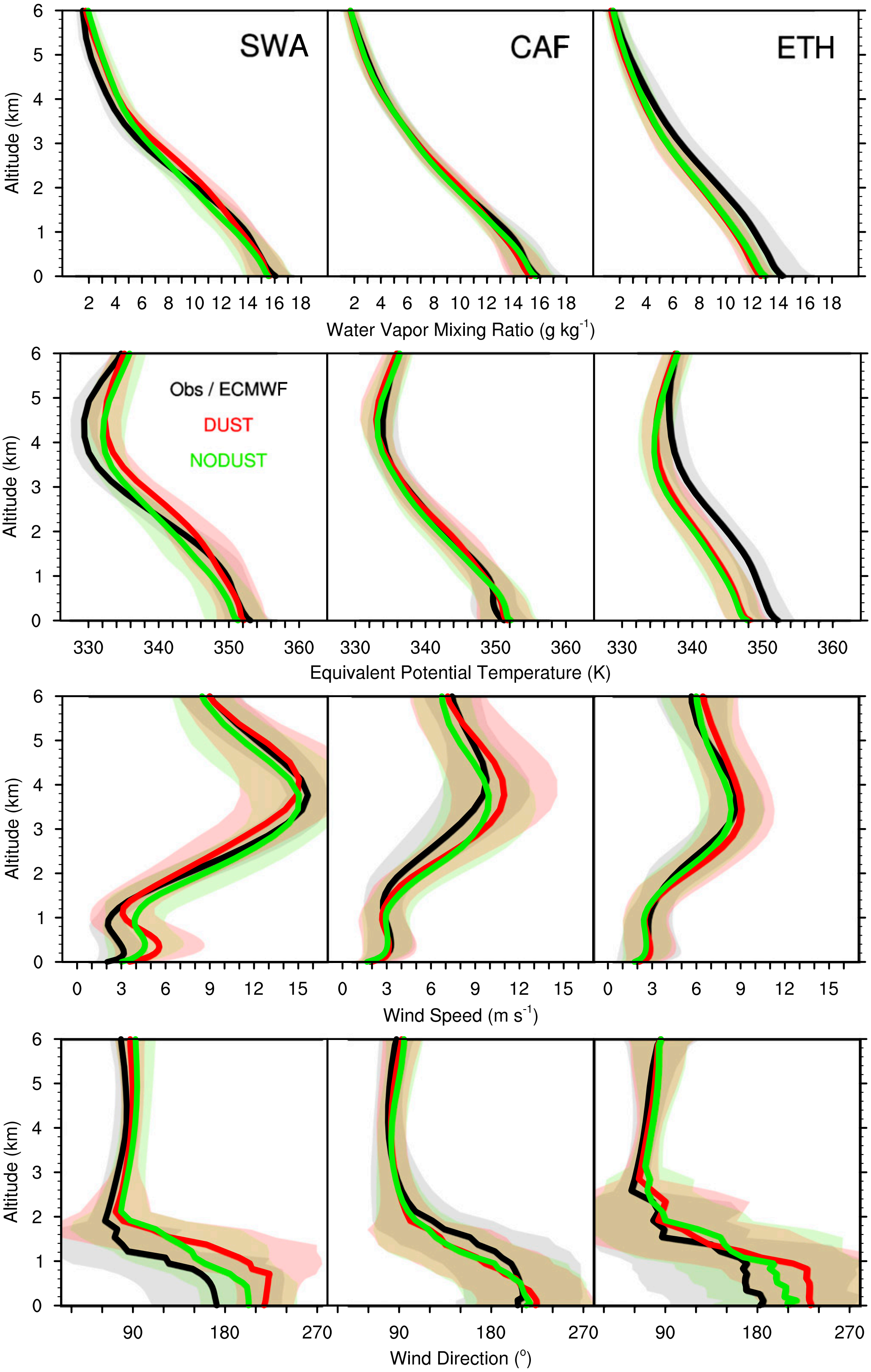

FIG. 14. Mean vertical profiles (from top to bottom) of the water vapor mixing ratio, equivalent potential temperature, wind speed, and wind direction for long-lived MCSs for each subregion: (left) SWA, (middle) CAF, and (right) ETH. The profiles are computed 6 h before the long-lived MCS detection. The shaded contours represent the standard deviation.

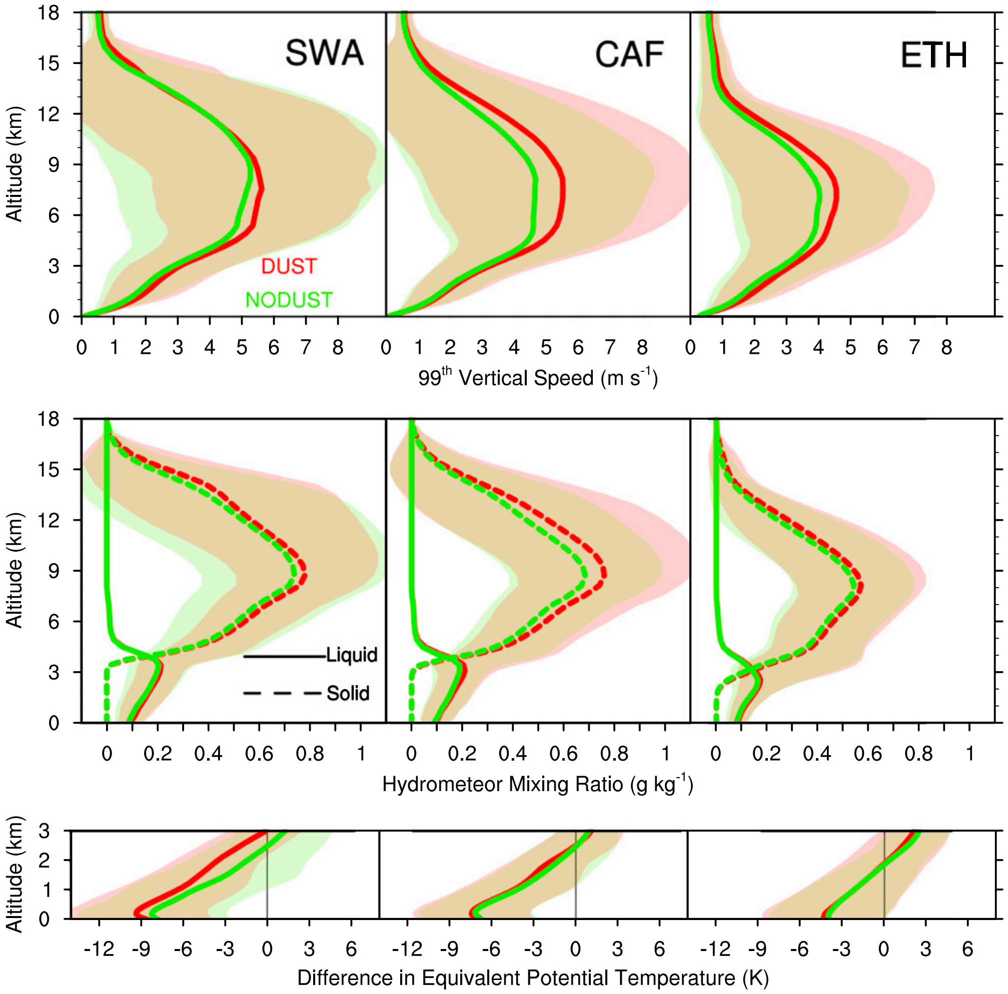

FIG. 15. Mean vertical profiles (from top to bottom) of the 99th percentile of the vertical wind speed, the mean hydrometeor mixing ratio (liquid and solid) for long-lived MCSs at the time of detection, and the difference in the mean equivalent temperature inside the long-lived MCS and at the same location 6 h before for (left) SWA, (middle) CAF, and (right) ETH. The shaded contours represent the standard deviation.

different cloud categories such as MCSs, which are then tracked and examined over the three continental subregions of southern West Africa, central Africa, and Ethiopia. This method is applied in the same manner to the two simulations and to the satellite observations. Both simulations show a realistic spatial distribution of precipitation when compared to the observations and capture the observed distribution of precipitation between the different cloud categories. The most organized and propagative MCSs account for the majority of the precipitation (approximately half of the total precipitation). The contribution to the precipitation of the other cloud types does not vary between the simulations.

An assessment of the simulations against the satellite and AERONET measurements shows that the simulation with dust–radiation interaction simulates the horizontal distribution and the vertical stratification of dust well and that the values of AOD are well represented and only slightly underestimated at the stations with the southwestern-most locations. This makes us confident that we can investigate the dust effects on the atmosphere based on a comparison of simulations with and without dust. A mean warming of 1.3 K is observed for the dust simulation between altitudes of 3 and 5 km, where the dust loads are at their maximum. These results are consistent with those obtained by Lemaître et al. (2010). A near-surface cooling is linked with the northern displacement of the intertropical discontinuity in the presence of dust, leading to an increase of moisture over land. Over the ocean, the intertropical convergence zone is shifted northward, modifying the distribution of precipitation. The perturbation of the temperature field and its meridional gradient is at the origin of the reported AEJ intensification of 1–2 $\mathrm{m\,s^{-1}}$ over southern West Africa. There, the midlevel warming and surface cooling are the most pronounced of the three subregions.

In tropical northern Africa, where strong sensible heat fluxes render the first layers of the atmosphere convectively unstable, the thermodynamics at low levels is pivotal for the triggering of convection. In the simulation with dust, the increase in the vertical gradient of the temperature leads to the stabilization of the lower atmosphere, as found by Tulet et al. (2008). Consequently, the triggering of long-lived MCSs (with lifetimes of at least 6 h) is reduced over southern West Africa. Their number decreases to one-third of the population that is simulated in the absence of dust–radiation interaction; therefore, the precipitation due to long-lived MCSs is greatly diminished, driving an overall drop in the total precipitation in that subregion.

When taking into account the radiative effects of dust, the long-lived MCSs are found to last a little longer, to be more efficient in terms of precipitation production, and to be more propagative. In other words, they are slightly more organized. Two factors play a role in helping the long-lived MCSs become more organized in the dust simulation. First, the acceleration of the AEJ drives an increase in the associated vertical low-level wind shear, a fundamental dynamical feature needed to maintain the MCSs (Laing et al. 2008; Reinares Martínez and Chaboureau 2018). Second, the simulation accounting for the radiative effect of dust was diagnosed as having a reservoir of CAPE greater than that of the simulation neglecting the radiative effect of dust; this energy was stored as a result of the inhibition of convective triggering. This energy is released when a long-lived MCS develops, leading to more intense convective activity, consistent with the increased degree of organization of the systems, and confirmed by the presence of faster updrafts and larger hydrometeor loadings within the clouds.

The results found here are sensitive to the description of dust in the model. Several uncertainties arise from emission, transport, and deposition, which affect the spatial distribution and lifetime of the dust particles. The results are also dependent on the optical properties of dust. Accurately constraining these processes in the model would lead to more realistic radiative dust effects. The microphysical dust–cloud interaction (the indirect effect of dust) is beyond the scope of this study but needs to be addressed. Dust particles are efficient ice nuclei, providing a substrate for ice initiation, which may drive changes in precipitation. Finally, the analysis performed here is restricted to a single 6-day period with large concentrations of dust. It would be worthwhile to repeat this analysis for other dusty cases. Extending this analysis to longer periods may also allow the conclusions found in this article to be generalized.

Acknowledgments. The research leading to these results has received funding from the European Union 7th Framework Program (FP7/2007-2013) under Grant Agreement 603502 (EU Project DACCIWA: Dynamics–aerosol–chemistry–cloud interactions in West Africa). Computer resources were allocated by GENCI through Project 90569. We thank the anonymous reviewers for their comments, which helped to improve the overall quality of the paper.

REFERENCES

Chaboureau, J.-P., and P. Bechtold, 2005: Statistical representation of clouds in a regional model and the impact on the diurnal cycle of convection during Tropical Convection, Cirrus and Nitrogen Oxides (TROCCINOX). *J. Geophys. Res.*, **110**, D17103, https://doi.org/10.1029/2004JD005645.

——, P. Tulet, and C. Mari, 2007: Diurnal cycle of dust and cirrus over West Africa as seen from Meteosat Second Generation satellite and a regional forecast model. *Geophys. Res. Lett.*, **34**, L02822, https://doi.org/10.1029/2006GL027771.

——, and Coauthors, 2008: A midlatitude precipitating cloud database validated with satellite observations. *J. Appl. Meteor. Climatol.*, **47**, 1337–1353, https://doi.org/10.1175/2007JAMC1731.1.

——, and Coauthors, 2011: Long-range transport of Saharan dust and its radiative impact on precipitation forecast: A case study during the Convective and Orographically-induced Precipitation Study (COPS). *Quart. J. Roy. Meteor. Soc.*, **137**, 236–251, https://doi.org/10.1002/qj.719.

——, and Coauthors, 2016: Fennec dust forecast intercomparison over the Sahara in June 2011. *Atmos. Chem. Phys.*, **16**, 6977–6995, https://doi.org/10.5194/acp-16-6977-2016.

Crumeyrolle, S., and Coauthors, 2011: Transport of dust particles from the Bodélé region to the monsoon layer—AMMA case study of the 9–14 June 2006 period. *Atmos. Chem. Phys.*, **11**, 479–494, https://doi.org/10.5194/acp-11-479-2011.

Cuxart, J., P. Bougeault, and J.-L. Redelsperger, 2000: A turbulence scheme allowing for mesoscale and large-eddy simulations. *Quart. J. Roy. Meteor. Soc.*, **126**, 1–30, https://doi.org/10.1002/qj.49712656202.

Engelstaedter, S., I. Tegen, and R. Washington, 2006: North African dust emissions and transport. *Earth-Sci. Rev.*, **79**, 73–100, https://doi.org/10.1016/j.earscirev.2006.06.004.

Flamant, C., J.-P. Chaboureau, D. J. Parker, C. M. Taylor, J.-P. Cammas, O. Bock, F. Timouk, and J. Pelon, 2007: Airborne observations of the impact of a convective system on the planetary boundary layer thermodynamics and aerosol distribution in the inter-tropical discontinuity region of the West African Monsoon. *Quart. J. Roy. Meteor. Soc.*, **133**, 1175–1189, https://doi.org/10.1002/qj.97.

——, C. Lavaysse, M. Todd, J.-P. Chaboureau, and J. Pelon, 2009: Multi-platform observations of a springtime case of Bodélé and Sudan dust emission, transport and scavenging over West Africa. *Quart. J. Roy. Meteor. Soc.*, **135**, 413–430, https://doi.org/10.1002/qj.376.

Fouquart, Y., and B. Bonnel, 1980: Computations of solar heating of the Earth's atmosphere—A new parametrization. *Beitr. Phys. Atmos.*, **53**, 35–62.

Grini, A., P. Tulet, and L. Gomes, 2006: Dusty weather forecasts using the MesoNH mesoscale atmospheric model. *J. Geophys. Res.*, **111**, D19205, https://doi.org/10.1029/2005JD007007.

Helmert, J., B. Heinold, I. Tegen, O. Hellmuth, and M. Wendisch, 2007: On the direct and semidirect effects of Saharan dust over Europe: A modeling study. *J. Geophys. Res.*, **112**, D13208, https://doi.org/10.1029/2006JD007444.

Holben, B. N., and Coauthors, 1998: AERONET—A federated instrument network and data archive for aerosol characterization. *Remote Sens. Environ.*, **66**, 1–16, https://doi.org/10.1016/S0034-4257(98)00031-5.

Hsu, N. C., S.-C. Tsay, M. D. King, and J. R. Herman, 2004: Aerosol properties over bright-reflecting source regions. *IEEE Trans. Geosci. Remote Sens.*, **42**, 557–569, https://doi.org/10.1109/TGRS.2004.824067.

Huffman, G. J., and Coauthors, 2007: The TRMM Multisatellite Precipitation Analysis (TMPA): Quasi-global, multiyear, combined-sensor precipitation estimates at fine scales. *J. Hydrometeor.*, **8** (1), 38–55, https://doi.org/10.1175/JHM560.1.

Janiga, M. A., and C. D. Thorncroft, 2014: Convection over tropical Africa and the East Atlantic during the West African Monsoon: Regional and diurnal variability. *J. Climate*, **27**, 4159–4188, https://doi.org/10.1175/JCLI-D-13-00449.1.

Janowiak, J. E., R. J. Joyce, and Y. Yarosh, 2001: A real-time global half-hourly pixel-resolution infrared dataset and its applications. *Bull. Amer. Meteor. Soc.*, **82**, 205–218, https://doi.org/10.1175/1520-0477(2001)082<0205:ARTGHH>2.3.CO;2.

Lac, C., and Coauthors, 2018: Overview of the Meso-NH model version 5.4 and its applications. *Geosci. Model Dev.*, **11**, 1929–1969, https://doi.org/10.5194/gmd-11-1929-2018.

Lafore, J. P., and Coauthors, 1998: The Meso-NH Atmospheric Simulation System. Part I: Adiabatic formulation and control simulations. *Ann. Geophys.*, **16**, 90–109, https://doi.org/10.1007/s00585-997-0090-6.

Laing, A. G., R. Carbone, V. Levizzani, and J. Tuttle, 2008: The propagation and diurnal cycles of deep convection in northern tropical Africa. *Quart. J. Roy. Meteor. Soc.*, **134**, 93–109, https://doi.org/10.1002/qj.194.

Lemaître, C., C. Flamant, J. Cuesta, J.-C. Raut, P. Chazette, P. Formenti, and J. Pelon, 2010: Radiative heating rates profiles associated with a springtime case of Bodélé and Sudan dust transport over West Africa. *Atmos. Chem. Phys.*, **10**, 8131–8150, https://doi.org/10.5194/acp-10-8131-2010.

Marticorena, B., and G. Bergametti, 1995: Modeling the atmospheric dust cycle: 1. Design of a soil-derived dust emission scheme. *J. Geophys. Res.*, **100**, 16 415–16 430, https://doi.org/10.1029/95JD00690.

Masson, V., and Coauthors, 2013: The SURFEXv7.2 land and ocean surface platform for coupled or offline simulation of Earth surface variables and fluxes. *Geosci. Model Dev.*, **6**, 929–960, https://doi.org/10.5194/gmd-6-929-2013.

Mathon, V., H. Laurent, and T. Lebel, 2002: Mesoscale convective system rainfall in the Sahel. *J. Appl. Meteor.*, **41**, 1081–1092, https://doi.org/10.1175/1520-0450(2002)041<1081:MCSRIT>2.0.CO;2.

Mlawer, E. J., S. J. Taubman, P. D. Brown, M. J. Iacono, and S. A. Clough, 1997: Radiative transfer for inhomogeneous atmospheres: RRTM, a validated correlated-k model for the longwave. *J. Geophys. Res.*, **102**, 16 663–16 682, https://doi.org/10.1029/97JD00237.

Noilhan, J., and S. Planton, 1989: A simple parameterization of land surface processes for meteorological models. *Mon. Wea. Rev.*, **117**, 536–549, https://doi.org/10.1175/1520-0493(1989)117<0536:ASPOLS>2.0.CO;2.

Parker, D. J., 2002: The response of CAPE and CIN to tropospheric thermal variations. *Quart. J. Roy. Meteor. Soc.*, **128**, 119–130, https://doi.org/10.1256/00359000260498815.

Pérez, C., S. Nickovic, G. Pejanovic, J. M. Baldasano, and E. Özsoy, 2006: Interactive dust-radiation modeling: A step to improve weather forecasts. *J. Geophys. Res.*, **111**, D16206, https://doi.org/10.1029/2005JD006717.

Pergaud, J., V. Masson, S. Malardel, and F. Couvreux, 2009: A parameterization of dry thermals and shallow cumuli for mesoscale numerical weather prediction. *Bound.-Layer Meteor.*, **132**, 83–106, https://doi.org/10.1007/s10546-009-9388-0.

Pinty, J.-P., and P. Jabouille, 1998: A mixed-phase cloud parameterization for use in a mesoscale non-hydrostatic model: Simulations of a squall line and of orographic precipitations. *Conf. on Cloud Physics*, Everett, WA, Amer. Meteor. Soc., 217–220.

Reinares Martínez, I., and J.-P. Chaboureau, 2018: Precipitation and mesoscale convective systems: Explicit versus parameterized convection over northern Africa. *Mon. Wea. Rev.*, **146**, 797–812, https://doi.org/10.1175/MWR-D-17-0202.1.

Saunders, R., M. Matricardi, P. Brunel, S. English, P. Bauer, U. O'Keeffe, P. Francis, and P. Rayer, 2005: RTTOV-8—Science and validation report. NWP SAF Tech. Rep., 41 pp., https://nwpsaf.eu/oldsite/deliverables/rtm/rttov8_svr.pdf.

Tompkins, A. M., C. Cardinali, J.-J. Morcrette, and M. Rodwell, 2005: Influence of aerosol climatology on forecasts of the African Easterly Jet. *Geophys. Res. Lett.*, **32**, L10801, https://doi.org/10.1029/2004GL022189.

Tulet, P., V. Crassier, F. Cousin, K. Suhre, and R. Rosset, 2005: ORILAM, a three-moment lognormal aerosol scheme for mesoscale atmospheric model: Online coupling into the Meso-NH-C model and validation on the Escompte campaign. *J. Geophys. Res.*, **110**, D18201, https://doi.org/10.1029/2004JD005716.

——, M. Mallet, V. Pont, J. Pelon, and A. Boone, 2008: The 7–13 March 2006 dust storm over West Africa: Generation, transport, and vertical stratification. *J. Geophys. Res.*, **113**, D00C08, https://doi.org/10.1029/2008JD009871.

Winker, D. M., M. A. Vaughan, A. Omar, Y. Hu, K. A. Powell, Z. Liu, W. H. Hunt, and S. A. Young, 2009: Overview of the CALIPSO mission and CALIOP data processing algorithms. *J. Atmos. Oceanic Technol.*, **26**, 2310–2323, https://doi.org/10.1175/2009JTECHA1281.1.

Zender, C. S., H. Bian, and D. Newman, 2003: Mineral Dust Entrainment and Deposition (DEAD) model: Description and 1990s dust climatology. *J. Geophys. Res.*, **108**, 4416, https://doi.org/10.1029/2002JD002775.

Zhang, G., K. H. Cook, and E. K. Vizy, 2016: The diurnal cycle of warm season rainfall over West Africa. Part I: Observational analysis. *J. Climate*, **29**, 8423–8437, https://doi.org/10.1175/JCLI-D-15-0874.1.

Conclusions and perspectives

During the monsoon season, precipitation in northern Africa arises from multiple precipitating systems, mainly of convective type. The convective systems producing rainfall can be rather isolated or organized into large cloud structures of size of 100 to 1000 km and lifetimes of several hours or days, named mesoscale convective systems (MCSs). MCSs are widely recognized as the major producers of precipitation in northern Africa. They are difficult to forecast because of the wide range of spatiotemporal scales of the processes involved. The internal processes within MCSs, such as updrafts and associated upward speeds, are difficult to observe and to measure, respectively. Thus, their simulation remains a challenge for numerical atmospheric models. The case study of 9-14 June 2006 examined here is a well-documented episode of dust emission and transport, and MCSs propagation in West Africa (Flamant et al., 2009). It was chosen to investigate the mechanisms controlling precipitation in northern Africa. Specifically, the underlying processes leading to the organization of MCSs have been addressed. On the one hand, the impact of the resolution and the representation of convection in Méso-NH on the characteristics of the MCSs is examined. On the other hand, the radiative effect of dust on the MCSs is explored.

To analyze the degree of MCSs organization, the properties of the MCSs such as their size, lifetime, propagation speed and the modulation of those characteristics by the environment have been analyzed, with the use of satellite observations and simulations. Three simulations were run with the Méso-NH model, two at a resolution of 2.5 km where convection is explicitly allowed and one at a resolution of 20 km with parameterized convection. Among the two convection-permitting simulations, one considers the radiative effect of dust, the other neglects it. A common clustering method is applied to the observational data set and the simulations, such that precipitating clouds are identified in terms of their brightness temperature (BT). The MCSs are defined as large deep convective clouds, and tracked individually. The long-lived MCSs, those that live at least 6 hours, are examined in detail in 3 sub-regions: the southern West Africa (SWA), Central Africa (CAF) and Ethiopia (ETH).

The observed precipitation is mainly located in a zonal band from 0 to 15°N. More than two thirds of the total precipitation are attributed to deep convective clouds. Among them, MCSs produce 66% of precipitation and the long-lived ones 55% of precipitation. So the long-lived MCSs are the greatest precipitation producers. They mainly dictate the diurnal cycle of precipitation that peaks at 2100 LST. The long-lived MCSs in SWA propagate southwestward. They show larger effective diameter (600 km), lifetime (20 h) and zonal propagation speed (18 m s^{-1}) than in CAF or ETH, thus showing the highest degree of organization. The environmental conditions drive the properties of the long-lived MCSs. The African Easterly Jet (AEJ) increases from ETH to SWA (from 8 to 16 m s^{-1}), strengthening the vertical wind shear. The conditional instability is the largest in SWA, also. Both the wind shear and conditional instability are some important factors that favor the organization of convection.

The convection-permitting simulation accounting for the radiative effect of dust captures the zonal distribution of precipitation correctly. The observed partition of precipitation is well reproduced, with 50% of precipitation due to long-lived MCSs. The latter contribute the most to the diurnal cycle of precipitation, well in phase with the observations. However, the long-lived MCSs show a deficit in precipitation in SWA. Despite the westward increase of both the AEJ speed and the conditional instability in the convection-permitting simulation, the long-lived MCSs are less organized in SWA than what the observations show. Smaller effective diameter (300 km), lifetime (11 h) and westward speed (12 m s^{-1}) are reported there when compared to the observations. The propagation of long-lived MCSs in SWA also presents a drawback. Their average direction presents a slightly northward component, rather than southward as observed. In the simulation with parameterized convection, the clouds contributing the most to precipitation are not classified as deep convective. The diurnal cycle of precipitation is mostly driven by those clouds and precedes the observed peak by 6 h (the maximum is at 1500 LST). In summary, the variability of precipitation and the partition of precipitation among cloud types are represented more realistically in the convection-permitting simulation than in the one with parameterized convection.

Dust outbreaks were reported in the Bodélé Depression in Chad and in Sudan during the 9-14 June 2006. The convection-permitting run with dust effect simulates those emissions at the right locations. The dust is mobilized by the Harmattan and is later transported over northern Africa. Measured and simulated optical depths in Tamanrasset attain values of 3. The atmosphere is found to be sensitive to the radiative effect of dust. The dust optical depth is the largest over SWA and the Sahara further north, between 10°W and 10°E, modifying the temperature of the atmosphere there. A heating of up to 1.3 K appears at 3 to

5-km altitude around 15°N, slightly north of the AEJ, and a cooling below, close to the surface. A warming occurs also over the Sahara, at altitudes between 1 and 5 km, but of smaller amplitude. This may correspond to dust load embedded in the Saharan Air Layer (SAL). The vertical stratification of dust changes the vertical gradient of temperature. The speed and location of the AEJ is found to vary, in turn, following the temperature changes to attain a new thermal wind equilibium. This results in an average intensification of the AEJ by 1 to 2 m s^{-1} in SWA.

Precipitation is overall reduced by 10% when considering the radiative effect of dust. Over the continent, the difference in rainfall is found mostly in SWA, and particularly from long-lived MCSs. These MCSs, in the dust simulation, last in average 2 hours longer and are 3 m s^{-1} faster than in the dust-free simulation. This finding is associated to a larger AEJ-induced shear. Moreover, the long-lived MCSs are more efficient in precipitation production, yielding in average 50 mm h^{-1} more rain rate per system. Thus, the factor driving the difference in precipitation due to long-lived MCSs is their number (8 for the dust simulation compared to 20 for the dust-free simulation). This reduced number can be explained through the vertical change in temperature induced by dust that renders the low-level atmosphere more stable preventing the triggering of convection. The inhibition of convection acts, consequently, enhancing the convective available potential energy (CAPE) in the free troposphere, such that the CAPE is overall larger in SWA. This enhanced CAPE can then be utilized by the long-lived MCSs that become more organized than in the dust-free simulation. In other words, the radiative dust effect favors a population of long-lived MCSs, less numerous but such that they last longer and precipitate more.

The contribution to precipitation of MCSs, which are responsible for 66% in the observations, is reproduced in a realistic manner by the Méso-NH convection-permitting simulations. The part of precipitation due to MCSs is 60% for the simulation with dust and 59% for the one without dust. The simulation with parameterized convection presents important biases in capturing the contribution of MCSs to rainfall (36%). Resolving explicitly the humidity transport within the updrafts for the hydrometeors formation is primordial. The two convection-permitting simulations converge in terms of MCSs contribution to precipitation. Besides, the dust radiative effect is found to play a role in the formation of more vigorous long-lived MCSs, with greater precipitation rates, hydrometeor loadings and vertical upward speeds in SWA. Thus, the convection-permitting simulation taking into account the radiative effect of dust is the most performant in capturing the observed characteristics of precipitation during the period of 9-14 June 2006.

The cloud organization is however poorly captured by the convection-permitting simulations in SWA. It arises from the interaction of atmospheric phenomena across a large range of scales. For instance, MCSs and African Easterly Waves (AEWs) are known to interact, mutually reinforcing each other and growing as they propagate westward. Furthermore, it is known that the environmental conditions in the northerly and trough sectors of the AEWs are beneficial for the MCS development. The location of the MCSs with respect to the AEWs with which they propagate remains to be explored in this case study. Here, the direction of propagation of the long-lived MCSs has erroneously a small northward component in SWA. A deeper understanding of the interaction of convection with the large-scale circulations is a pathway to the development of numerical models capable to reproduce the African weather more realistically. Furthermore, the conditions employed to initialize the simulation can lead to errors in the large-scale meteorological fields. Repeating this study over a different period would be instructive to distinguish the relative importance of the biases introduced by the model from the role of the environment on the accurate representation of the precipitating systems.

The turbulent eddies inside MCSs, of length scales $\sim$1 km and smaller, are not explicitely represented in the convection-permitting simulations. Most of the kinetic energy contained in those subgrid eddies remains unresolved, and they are parameterized by a turbulence scheme. Here, we employed a turbulence scheme in 1D, i.e., that accounts for the vertical transport of the eddies only (which is usually suitable for CPM simulations). These sub-kilometer eddies play an important role in the mixing betwen the cloud and the environment, which can, in turn, modify the entrainment of surrounding air into the cloud. Machado and Chaboureau (2015) found a significant impact of the mixing length of the turbulence scheme on the number, the size and the depth of the deep convective cloud population during a field campaign in Brazil. The sensitivity of the cloud organization, not fully captured in this study, to the mixing length could be worthwhile to be examined.

The representativity of the results obtained for a sole case study is yet to be confirmed. The tracking method implemented here can be applied on other dusty periods, or a whole monsoon season. In a longer perspective, the analysis carried out here can be done on the 17-year TRMM available data, to build a monthly climatology of the organization of MCSs. This will filter out the inter-annual variability of the convective activity.

Regarding the dust effect on precipitation, only the radiative effect was considered here. A follow-up path would be to investigate the dust indirect effect on precipitation. Dust can act as ice crystal precursor. Through the increase of the ice embryos population, the availability of water vapor or supercooled water to make grow those crystals into precipitating hydrometeors decreases. Thus, the indirect effect of dust on cloud microphysics is generally thought to be detrimental for precipitation. The LIMA (Liquid Ice Multiple Aerosols, Vié et al., 2016) scheme, that accounts for the aerosols-cloud interactions, could be utilized in future Méso-NH simulations for an insight on the role of dust on the cloud microphysics and the resulting precipitation.

In the framework of the DACCIWA (Dynamics-aerosol-chemistry-cloud interaction in West Africa) project, simulations will be run over the southern West Africa to investigate the processes leading to precipitation for case studies from the summer field campaign of 2016. These simulations will benefit from the observations gathered during the campaign for evaluation. Particularly, the shallow-to-deep convection transition, one relevant subject of the project, will be explored. Large-Eddy Simulations (LES) can be performed nowadays over relatively large domains and are promising to disentangle the processes underlying the vertical development of convection (Khairoutdinov and Randall, 2006; Dauhut et al., 2016). The Méso-NH model can be run in such LES mode, with a horizontal resolution of $\sim$100 m. This high resolution allows one to represent well the turbulent transport within the convective boundary layer, as the largest and most energetic eddies are not subgrid. The representation of both the surface processes and the cold pool outflows that shove near-surface air possibly triggering new shallow clouds is important to simulate the development of deep convective clouds (Khairoutdinov and Randall, 2006; Couvreux et al., 2012). The method used in this work for the cloud identification as distinct objects could be adapted to the study of shallow-to-deep convection transition. Different BT thresholds could be established, each for a different stage of vertical development of the clouds, as if the clouds were scanned vertically in time. Statistics on the size of the clouds or the time needed for the shallow-to-deep transition could be computed.

Conclusions et perspectives (en français)

Pendant la saison de la mousson, les précipitations en Afrique septentrionale proviennent de systèmes précipitants multiples, principalement de type convectif. Les systèmes convectifs produisant des précipitations peuvent être plutôt isolés ou organisés en grandes structures nuageuses de taille de 100 à 1000 km et des durées de vie de plusieurs heures ou jours, appelés systèmes convectifs de mésoéchelle (MCS, de l'anglais *Mesoscale Convective System*). Les MCS sont largement reconnus comme les principaux producteurs de précipitations en Afrique septentrionale. Ils sont difficiles à prévoir en raison de la vaste gamme d'échelles spatio-temporelles des processus impliqués. Les processus internes au sein des MCS, tels que les courants ascendants et les vitesses associées, sont difficiles à observer et à mesurer, respectivement. Ainsi, leur simulation reste un défi pour les modèles numériques atmosphériques. L'étude de cas du 9 au 14 juin 2006 examinée ici est un épisode bien documenté d'émission et de transport de poussières, et de propagation des MCS en Afrique de l'Ouest (Flamant et al., 2009). Il a été choisi pour étudier les mécanismes de contrôle des précipitations en Afrique septentrionale. Plus précisément, les processus sous-jacents menant à l'organisation des MCS ont été abordés. D'une part, l'impact de la résolution et de la représentation de la convection dans Méso-NH sur les caractéristiques des MCS est examiné. D'autre part, l'effet radiatif des poussières sur les MCS est exploré.

Pour analyser le degré d'organisation des MCS, les propriétés des MCS telles que leur taille, leur durée de vie, leur vitesse de propagation et la modulation de leurs caractéristiques par l'environnement ont été analysées en utilisant des observations satellitaires et des simulations. Trois simulations ont été lancées avec le modèle Méso-NH, deux à une résolution de 2,5 km où la convection est explicitement représentée et une à une résolution de 20 km pour laquelle la convection est paramétrée. Parmi les deux simulations réalisées avec le modèle permettant la convection (CPM, de l'anglais *Convection-Permitting Model*)), l'une considère l'effet radiatif des poussières, l'autre le néglige. Une méthode de regroupement commune est appliquée à la fois aux observations et aux simulations, de sorte que les nuages précipitants sont identifiés en fonction de leur température de brillance (BT, de l'anglais *Brightness Temperature*). Les MCS sont définis comme de grands nuages convectifs profonds et sont suivis individuellement. Les MCS à longue durée de vie, ceux qui vivent au moins 6 heures, sont examinés en détail dans 3 sous-régions : l'Afrique de l'Ouest méridionale (SWA, de l'anglais *Southern West Africa*), l'Afrique centrale (CAF, de l'anglais *Central Africa*) et l'Éthiopie (ETH, de l'anglais *Ethiopia*).

Les précipitations observées se situent principalement dans une bande zonale entre 0° et 15°N. Plus des deux tiers des précipitations totales sont attribués aux nuages convectifs profonds. Parmi eux, les MCS produisent 66% de précipitations et les MCS à longue durée de vie 55%. Ainsi, les MCS à longue durée de vie sont les plus grands producteurs de précipitations. Ils dictent principalement le cycle diurne des précipitations qui atteint un sommet à 2100 heure locale. Les MCS à longue durée de vie dans SWA se propagent vers le sud-ouest. Ils présentent un diamètre effectif (600 km), une durée de vie (20 h) et une vitesse zonale de propagation (18 m s^{-1}) plus grands que dans CAF ou ETH, montrant ainsi le plus haut degré d'organisation. Les conditions environnementales pilotent les propriétés des MCS à longue durée de vie. Le jet d'est africain (AEJ, de l'anglais *African Easterly Jet*) augmente d'ETH à SWA (de 8 à 16 m s^{-1}), ce qui renforce le cisaillement vertical du vent. L'instabilité conditionnelle est également la plus importante dans SWA. Le cisaillement du vent et l'instabilité conditionnelle sont des facteurs importants qui favorisent l'organisation de la convection.

La simulation CPM prenant en compte l'effet radiatif des poussières reproduit correctement la répartition zonale des précipitations. La répartition observée des précipitations est bien reproduite, avec 50% de précipitation due à des MCS à longue durée de vie. Ces derniers contribuent le plus au cycle diurne des précipitations, bien synchronisés avec les observations. Cependant, les MCS à longue durée de vie montrent un déficit de précipitations dans SWA. Malgré l'augmentation vers l'ouest de la vitesse de l'AEJ et de l'instabilité conditionnelle dans la simulation CPM, les MCS à longue durée de vie sont moins organisés dans SWA que ce que montrent les observations. Un diamètre effectif (300 km), une durée de vie (11 h) et une vitesse vers l'ouest (12 m s^{-1}) sont trouvés là-bas, plus petits que ceux observés. La propagation des MCS à longue durée de vie dans SWA présente également un défaut. Leur direction moyenne présente une composante légèrement vers le nord, plutôt que vers le sud, comme cela a été observé. Dans la simulation avec convection paramétrée, les nuages qui contribuent le plus aux précipitations ne sont pas classés comme convectifs profonds. Le cycle diurne des précipitations est principalement influencé par ces nuages et précède le pic observé de 6 h (le maximum est à 1500 heure locale). En résumé, la variabilité des précipitations et la répartition des précipitations entre types de nuages sont représentées de manière plus réaliste dans la simulation avec convection permise que dans celle avec convection paramétrée.

Des épisodes de poussières ont été signalées dans la dépression de Bodélé au Tchad et au Soudan entre les 9 et 14 juin 2006. La simulation CPM avec effet de poussières simule ces émissions au bon endroit. Les poussières sont mobilisées par l'Harmattan et ensuite transportées en Afrique septentrionale. Les profondeurs optiques mesurées et simulées à Tamanrasset atteignent des valeurs de 3. L'atmosphère se révèle être sensible à l'effet radiatif des poussières. La profondeur optique de la poussière est la plus grande dans SWA et le Sahara plus au nord, entre 10°W et 10°E, ce qui modifie la température de l'atmosphère. Un chauffage jusqu'à 1,3 K apparaît à une altitude de 3 à 5 km autour de 15°N, légèrement au nord de l'AEJ, et un refroidissement en-dessous, près de la surface. Un réchauffement se produit également sur le Sahara, à des altitudes comprises entre 1 et 5 km, mais de plus petite amplitude. Cela peut correspondre à la charge en poussières intégrée dans la couche d'air saharienne (SAL). La stratification verticale de la poussière change le gradient vertical de température. La vitesse et l'emplacement de l'AEJ se révèlent varier, à leur tour, suite aux changements de température pour atteindre un nouvel équilibre du vent thermique. Il en résulte une intensification moyenne de l'AEJ de 1 à 2 m s^{-1} dans SWA.

Les précipitations sont globalement réduites de 10% en considérant l'effet radiatifs des poussières. Sur le continent, la différence de précipitations se retrouve principalement dans SWA, et en particulier dans les MCS à longue durée de vie. Ces MCS, dans la simulation CPM avec poussières, durent en moyenne 2 heures de plus et sont 3 m s^{-1} plus rapides que dans la simulation CPM sans poussières. Ce résultat est associé à un plus grand cisaillement induit par l'AEJ. En outre, les MCS à longue durée de vie sont plus efficaces dans la production des précipitations, ce qui donne en moyenne 50 mm h^{-1} de plus en taux de pluie par système. Ainsi, le facteur qui entraîne la différence en précipitation due aux MCS à longue durée de vie est leur nombre (8 pour la simulation avec poussières par rapport à 20 pour la simulation sans poussières). Ce nombre réduit s'explique par la variation verticale de la température induite par les poussières qui rend l'atmosphère à bas niveau plus stable empêchant le déclenchement de la convection. L'inhibition de la convection agit, par conséquent, en augmentant l'énergie potentielle convective disponible (CAPE, de l'anglais *Convective Available Potential Energy*) dans la troposphère libre, de sorte que la CAPE soit globalement plus grande dans SWA. Cette CAPE augmentée peut ensuite être utilisée par les MCS à longue durée de vie qui deviennent plus organisés que dans la simulation sans poussière. En d'autres termes, l'effet radiatif des poussières favorise une population de MCS à longue durée de vie, moins nombreux mais qui durent plus longtemps et précipitent davantage.

La contribution à la précipitation des MCS (66% dans les observations) est reproduite de manière réaliste par les simulations CPM de Méso-NH. La partie des précipitations due aux MCS est de 60% pour la simulation avec poussière et de 59% pour celle sans poussière. La simulation avec convection paramétrée présente des biais importants pour reproduire la contribution des MCS aux précipitations (36%). Résoudre explicitement le transport de l'humidité dans les courants ascendants pour la formation des hydromètres est primordial. Les deux simulations CPM convergent en termes de contribution des MCS aux précipitations. En outre, l'effet radiatif de la poussière joue un rôle dans la formation de MCS à longue durée de vie plus vigoureux, avec des taux de précipitations, des contenus en hydrométéores et des vitesses verticales ascendantes plus élevés dans SWA. Ainsi, la simulation CPM prenant en compte l'effet radiatif des poussières est la plus performante pour reproduire les caractéristiques observées des précipitations pendant la période du 9 au 14 juin 2006.

L'organisation des nuages est toutefois mal reproduite par les simulations CPM dans SWA. Cela résulte de l'interaction de phénomènes atmosphériques dans une large gamme d'échelles. Par exemple, les MCS et les ondes d'est africaines (AEW, de l'anglais *African Easterly Waves*) sont connues pour interagir, se renforcer mutuellement et s'accroître lorsqu'ils se propagent vers l'ouest. En outre, on sait que les conditions environnementales dans le secteur nord et celui du thalweg des AEW sont bénéfiques pour le développement des MCS. L'emplacement des MCS par rapport aux AEW avec lesquels ils propagent reste à explorer dans ce cas d'étude. Ici, la direction de propagation des MCS à longue durée de vie a de manière incorrecte une petite composante vers le nord dans SWA. Une compréhension plus profonde de l'interaction de la convection avec les circulations de grande échelle est une perspective pour développer de modèles numériques capables de reproduire le climat africain de manière plus réaliste. En outre, les conditions employées pour initialiser la simulation peuvent entraîner des erreurs dans les champs météorologiques de grande échelle. Répéter cette étude sur une période différente serait instructif afin de distinguer l'importance relative des biais introduits par le modèle et ceux venant de l'environnement sur la représentation exacte des systèmes de précipitation.

Les tourbillons turbulents à l'intérieur des MCS, aux longueurs d'échelles de $\sim$1 km et plus petites, ne sont pas explicitement représentés dans les simulations CPM. La majeure partie de l'énergie cinétique contenue dans ces tourbillons d'échelle sous-maille reste non résolue. Ils sont donc paramétrés par un schéma de turbulence. Ici, nous avons utilisé un schéma de turbulence en 1D, c'est-à-dire qu'il prend en compte uniquement le transport vertical des tourbillons (ce qui convient habituellement aux simulations CPM). Ces tourbillons d'échelle sous-kilomètrique jouent un rôle important dans le mélange entre le nuage et l'environnement, qui peut, à son tour, modifier l'entraînement de l'air environnant dans le nuage. Machado and Chaboureau (2015) ont trouvé un impact significatif de la longueur de mélange du schéma de turbulence sur le nombre, la taille et la profondeur de la population de nuages convectifs profonds lors d'une campagne de terrain au Brésil. La sensibilité de l'organisation nuageuse (non entièrement reproduite ici) à la longueur de mélange pourrait valoir la peine d'être examinée.

La représentativité des résultats obtenus pour une seule étude de cas doit encore être confirmée. La méthode de suivi implémentée ici peut être appliquée sur d'autres périodes poussiéreuses, ou toute une saison de mousson. Dans une perspective plus longue, l'analyse effectuée ici pourrait être effectuée sur les 17 ans de données TRMM disponibles afin de construire une climatologie mensuelle de l'organisation des MCS. Cela éliminera la variabilité interannuelle de l'activité convective.

En ce qui concerne l'effet des poussières sur les précipitations, seul l'effet radiatif a été considéré ici. Une perspective serait d'étudier l'effet indirect des poussières sur les précipitations. La poussière peut agir comme précurseur de cristaux de glace. Grâce à l'augmentation de la population d'embryons de glace, la disponibilité de vapeur d'eau ou d'eau surfondue pour faire croître ces cristaux ce qui diminueraient les hydrométeores précipitants. Ainsi, l'effet indirect des poussières sur la microphysique des nuages est généralement considéré comme nuisible aux précipitations. Le schéma LIMA (*Liquid Ice Multiple Aerosols*, Vié et al., 2016), qui prend en compte les interactions aérosols-nuages, pourrait être utilisé dans de futures simulations Méso-NH pour avoir une idée du rôle de la poussière sur la microphysique des nuages et des précipitations.

Dans le cadre du projet DACCIWA (*Dynamics-Aerosol-Chemistry-Cloud Interaction in West Africa*), des simulations seront réalisées sur le sud de l'Afrique de l'Ouest pour étudier les processus conduisant aux précipitations pour des études de cas de la campagne de terrain de l'été 2016. Ces simulations bénéficieront des observations recueillies lors de la campagne pour leur évaluation. En particulier, la transition de convection peu profonde à profonde, un sujet pertinent du projet, sera explorée. Les simulations aux grandes échelles (LES, de l'anglais *large-eddy simulations*) peuvent être effectuées de nos jours sur des domaines relativement importants, ce qui est très prometteur pour démêler les processus qui sous-tendent le développement vertical de la convection (Khairoutdinov and Randall, 2006; Dauhut et al., 2016). Le modèle Méso-NH peut être lancé dans ce mode LES, avec une résolution horizontale de ~100 m. Cette fine résolution permet de bien représenter le transport turbulent dans la couche limite convective, car les tourbillons les plus grands et les plus énergétiques ne sont alors plus d'échelle sous-maille. La représentation à la fois des processus de surface et des poches froides qui poussent l'air proche de la surface, déclenchant éventuellement de nouveaux nuages peu profonds, est importante pour simuler le développement de nuages convectifs profonds (Khairoutdinov and Randall, 2006; Couvreux et al., 2012). La méthode utilisée ici pour l'identification des nuages en tant qu'objets distincts pourra être adaptée à l'étude de la transition de convection peu profonde à profonde. Différents seuils en BT pourraient être établis, chacun pour une étape différente du développement vertical des nuages, comme si les nuages étaient sondés verticalement dans le temps. Des statistiques sur la taille des nuages ou le temps nécessaire à la transition peu profonde à profonde pourraient être calculées.

Bibliography

Arkin, P. A., and B. N. Meisner, 1987: The Relationship between Large-Scale Convective Rainfall and Cold Cloud over the Western Hemisphere during 1982-84. *Monthly Weather Review*, **115 (1)**, 51–74.

Bangalath, H. K., and G. Stenchikov, 2015: Role of dust direct radiative effect on the tropical rain belt over Middle East and North Africa: A high-resolution AGCM study. *Journal of Geophysical Research: Atmospheres*, **120 (10)**, 2015JD023 122.

Bayo Omotosho, J., 1985: The separate contributions of line squalls, thunderstorms and the monsoon to the total rainfall in Nigeria. *Journal of Climatology*, **5 (5)**, 543–552.

Bechtold, P., E. Bazile, F. Guichard, P. Mascart, and E. Richard, 2001: A mass-flux convection scheme for regional and global models. *Quarterly Journal of the Royal Meteorological Society*, **127 (573)**, 869–886.

Bou Karam, D., C. Flamant, P. Knippertz, O. Reitebuch, J. Pelon, M. Chong, and A. Dabas, 2008: Dust emissions over the Sahel associated with the West African monsoon intertropical discontinuity region: A representative case-study. *Quarterly Journal of the Royal Meteorological Society*, **134 (632)**, 621–634.

Bou Karam, D., C. Flamant, P. Tulet, M. C. Todd, J. Pelon, and E. Williams, 2009: Dry cyclogenesis and dust mobilization in the intertropical discontinuity of the West African Monsoon: A case study. *Journal of Geophysical Research: Atmospheres*, **114 (D5)**, D05 115.

Chaboureau, J.-P., and P. Bechtold, 2005: Statistical representation of clouds in a regional model and the impact on the diurnal cycle of convection during Tropical Convection, Cirrus and Nitrogen Oxides (TROCCINOX). *J. Geophys. Res.*, **110**, D17 103.

Chaboureau, J.-P., P. Tulet, and C. Mari, 2007: Diurnal cycle of dust and cirrus over West Africa as seen from Meteosat Second Generation satellite and a regional forecast model. *Geophysical Research Letters*, **34 (2)**.

Chaboureau, J.-P., and Coauthors, 2011: Long-range transport of Saharan dust and its radiative impact on precipitation forecast: a case study during the Convective and Orographically-induced Precipitation Study (COPS). *Quarterly Journal of the Royal Meteorological Society*, **137 (S1)**, 236–251.

Chaboureau, J.-P., and Coauthors, 2016: Fennec dust forecast intercomparison over the Sahara in June 2011. *Atmos. Chem. Phys.*, **16**, 6977–6995.

CLIVAR, 2015: Special Issue on Monsoons: advancing understanding of monsoon variability and improving prediction. *Exchanges 19*.

Collier, J. C., and K. P. Bowman, 2004: Diurnal cycle of tropical precipitation in a general circulation model. *Journal of Geophysical Research: Atmospheres*, **109 (D17)**, D17 105.

Couvreux, F., F. Guichard, O. Bock, B. Campistron, J.-P. Lafore, and J.-L. Redelsperger, 2010: Synoptic variability of the monsoon flux over West Africa prior to the onset. *Quarterly Journal of the Royal Meteorological Society*, **136 (S1)**, 159–173.

Couvreux, F., C. Rio, F. Guichard, M. Lothon, G. Canut, D. Bouniol, and A. Gounou, 2012: Initiation of daytime local convection in a semi-arid region analysed with high-resolution simulations and AMMA observations. *Quarterly Journal of the Royal Meteorological Society*, **138 (662)**, 56–71.

Crumeyrolle, S., and Coauthors, 2011: Transport of dust particles from the Bodélé region to the monsoon layer – AMMA case study of the 9–14 June 2006 period. *Atmos. Chem. Phys.*, **11 (2)**, 479–494.

Cuesta, J., C. Lavaysse, C. Flamant, M. Mimouni, and P. Knippertz, 2010: Northward bursts of the West African monsoon leading to rainfall over the Hoggar Massif, Algeria. *Quarterly Journal of the Royal Meteorological Society*, **136 (S1)**, 174–189.

Cuesta, J., J. H. Marsham, D. J. Parker, and C. Flamant, 2009: Dynamical mechanisms controlling the vertical redistribution of dust and the thermodynamic structure of the West Saharan atmospheric boundary layer during summer. *Atmospheric Science Letters*, **10 (1)**, 34–42.

Cuxart, J., P. Bougeault, and J.-L. Redelsperger, 2000: A turbulence scheme allowing for mesoscale and large-eddy simulations. *Quarterly Journal of the Royal Meteorological Society*, **126 (562)**, 1–30.

Dauhut, T., J.-P. Chaboureau, J. Escobar, and P. Mascart, 2016: Giga-LES of Hector the Convector and Its Two Tallest Updrafts up to the Stratosphere. *Journal of the Atmospheric Sciences*, **73 (12)**, 5041–5060.

Diongue, A., J.-P. Lafore, J.-L. Redelsperger, and R. Roca, 2002: Numerical study of a Sahelian synoptic weather system: Initiation and mature stages of convection and its interactions with the large-scale dynamics. *Quarterly Journal of the Royal Meteorological Society*, **128 (584)**, 1899–1927.

Duvel, J. P., 1989: Convection over Tropical Africa and the Atlantic Ocean during Northern Summer. Part I: Interannual and Diurnal Variations. *Monthly Weather Review*, **117 (12)**, 2782–2799.

Engelstaedter, S., I. Tegen, and R. Washington, 2006: North African dust emissions and transport. *Earth-Science Reviews*, **79 (1)**, 73–100.

Engelstaedter, S., and R. Washington, 2007: Atmospheric controls on the annual cycle of North African dust. *Journal of Geophysical Research: Atmospheres*, **112 (D3)**, D03 103.

Fink, A. H., and A. Reiner, 2003: Spatiotemporal variability of the relation between African Easterly Waves and West African Squall Lines in 1998 and 1999. *Journal of Geophysical Research: Atmospheres*, **108 (D11)**, 4332.

Fink, A. H., D. G. Vincent, and V. Ermert, 2006: Rainfall Types in the West African Sudanian Zone during the Summer Monsoon 2002. *Monthly Weather Review*, **134 (8)**, 2143–2164.

Fiolleau, T., and R. Roca, 2013: An Algorithm for the Detection and Tracking of Tropical Mesoscale Convective Systems Using Infrared Images From Geostationary Satellite. *IEEE Transactions on Geoscience and Remote Sensing*, **51 (7)**, 4302–4315.

Flamant, C., J.-P. Chaboureau, D. J. Parker, C. M. Taylor, J.-P. Cammas, O. Bock, F. Timouk, and J. Pelon, 2007: Airborne observations of the impact of a convective system on the planetary boundary layer thermodynamics and aerosol distribution in the inter-tropical discontinuity region of the West African Monsoon. *Quarterly Journal of the Royal Meteorological Society*, **133 (626)**, 1175–1189.

Flamant, C., C. Lavaysse, M. Todd, J.-P. Chaboureau, and J. Pelon, 2009: Multi-platform observations of a representative springtime case of Bodélé and Sudan dust emission, transport and scavenging over West Africa. *Quart. J. Roy. Meteor. Soc.*, **135**, 413–430.

Fouquart, Y., and B. Bonnel, 1986: Computations of solar heating of the Earth's atmosphere: A new parametrization. *Beitr. Phys. Atmos.*, **53**, 35–62.

Grini, A., P. Tulet, and L. Gomes, 2006: Dusty weather forecasts using the MesoNH mesoscale atmospheric model. *Journal of Geophysical Research*, **111 (D19)**.

Heinold, B., I. Tegen, K. Schepanski, and O. Hellmuth, 2008: Dust radiative feedback on Saharan boundary layer dynamics and dust mobilization. *Geophysical Research Letters*, **35 (20)**, L20 817.

Helmert, J., B. Heinold, I. Tegen, O. Hellmuth, and M. Wendisch, 2007: On the direct and semidirect effects of Saharan dust over Europe: A modeling study. *Journal of Geophysical Research: Atmospheres*, **112 (D13)**, D13 208.

Holben, B. N., and Coauthors, 1998: AERONET—A Federated Instrument Network and Data Archive for Aerosol Characterization. *Remote Sensing of Environment*, **66 (1)**, 1–16.

Holloway, C. E., S. J. Woolnough, and G. M. S. Lister, 2012: Precipitation distributions for explicit versus parametrized convection in a large-domain high-resolution tropical case study. *Quarterly Journal of the Royal Meteorological Society*, **138 (668)**, 1692–1708.

Houze, R. A., 1977: Structure and Dynamics of a Tropical Squall–Line System. *Monthly Weather Review*, **105 (12)**, 1540–1567.

Houze, R. A., 1994: *Cloud dynamics*, Vol. 53.

Houze, R. A., M. I. Biggerstaff, S. A. Rutledge, and B. F. Smull, 1989: Interpretation of Doppler Weather Radar Displays of Midlatitude Mesoscale Convective Systems. *Bulletin of the American Meteorological Society*, **70 (6)**, 608–619.

Hsu, N. C., S.-C. Tsay, M. D. King, and J. R. Herman, 2004: Aerosol properties over bright-reflecting source regions. *IEEE Transactions on Geoscience and Remote Sensing*, **42 (3)**, 557–569.

Huffman, G. J., and Coauthors, 2007: The TRMM Multisatellite Precipitation Analysis (TMPA): Quasi-Global, Multiyear, Combined-Sensor Precipitation Estimates at Fine Scales. *Journal of Hydrometeorology*, **8 (1)**, 38–55.

Janicot, S., and Coauthors, 2008: Large-scale overview of the summer monsoon over West Africa during the AMMA field experiment in 2006. *Annales Geophysicae*, **26 (9)**, 2569–2595.

Janiga, M. A., and C. D. Thorncroft, 2014: Convection over Tropical Africa and the East Atlantic during the West African Monsoon: Regional and Diurnal Variability. *Journal of Climate*, **27 (11)**, 4159–4188.

Janiga, M. A., and C. D. Thorncroft, 2016: The Influence of African Easterly Waves on Convection over Tropical Africa and the East Atlantic. *Monthly Weather Review*, **144 (1)**, 171–192.

Janowiak, J. E., R. J. Joyce, and Y. Yarosh, 2001: A real-time global half-hourly pixel resolution infrared dataset and its applications. *Bulletin of the American Meteorological Society*, **82**, 205–217.

Johnson, R. H., T. M. Rickenbach, S. A. Rutledge, P. E. Ciesielski, and W. H. Schubert, 1999: Trimodal Characteristics of Tropical Convection. *Journal of Climate*, **12 (8)**, 2397–2418.

Kain, J. S., and J. M. Fritsch, 1989: A One-Dimensional Entraining/Detraining Plume Model and Its Application in Convective Parameterization. *Journal of the Atmospheric Sciences*, **47 (23)**, 2784–2802.

Khairoutdinov, M., and D. Randall, 2006: High-Resolution Simulation of Shallow-to-Deep Convection Transition over Land. *Journal of the Atmospheric Sciences*, **63 (12)**, 3421–3436.

Knippertz, P., C. Deutscher, K. Kandler, T. Müller, O. Schulz, and L. Schütz, 2007: Dust mobilization due to density currents in the Atlas region: Observations from the Saharan Mineral Dust Experiment 2006 field campaign. *Journal of Geophysical Research: Atmospheres*, **112 (D21)**, D21 109.

Knippertz, P., and M. C. Todd, 2012: Mineral dust aerosols over the Sahara: Meteorological controls on emission and transport and implications for modeling. *Reviews of Geophysics*, **50 (1)**, RG1007.

Kocha, C., P. Tulet, J.-P. Lafore, and C. Flamant, 2013: The importance of the diurnal cycle of Aerosol Optical Depth in West Africa: diurnal cycle of AOD in West Africa. *Geophysical Research Letters*, **40 (4)**, 785–790.

Korecha, D., and A. G. Barnston, 2007: Predictability of June–September Rainfall in Ethiopia. *Monthly Weather Review*, **135 (2)**, 628–650.

Lafore, J. P., and Coauthors, 1998: The Meso-NH Atmospheric Simulation System. Part I: adiabatic formulation and control simulations. *Annales Geophysicae*, **16 (1)**, 90–109.

Laing, A. G., R. Carbone, V. Levizzani, and J. Tuttle, 2008: The propagation and diurnal cycles of deep convection in northern tropical Africa. *Quarterly Journal of the Royal Meteorological Society*, **134 (630)**, 93–109.

Laing, A. G., S. B. Trier, and C. A. Davis, 2012: Numerical Simulation of Episodes of Organized Convection in Tropical Northern Africa. *Monthly Weather Review*, **140 (9)**, 2874–2886.

Lau, K. M., K. M. Kim, Y. C. Sud, and G. K. Walker, 2009: A GCM study of the response of the atmospheric water cycle of West Africa and the Atlantic to Saharan dust radiative forcing. *Ann. Geophys.*, **27 (10)**, 4023–4037.

Laurent, H., 2005: Simulation des émissions d'aérosols désertiques à l'échelle continentale : Analyse climatologique des émissions du nord-est de l'Asie et du nord de l'Afrique. Ph.D. thesis.

Lavaysse, C., J.-P. Chaboureau, and C. Flamant, 2011: Dust impact on the West African heat low in summertime. *Quarterly Journal of the Royal Meteorological Society*, **137 (658)**, 1227–1240.

Le Barbé, L., T. Lebel, and D. Tapsoba, 2002: Rainfall Variability in West Africa during the Years 1950–90. *Journal of Climate*, **15 (2)**, 187–202.

Lebel, T., and Coauthors, 2010: The AMMA field campaigns: multiscale and multidisciplinary observations in the West African region. *Quarterly Journal of the Royal Meteorological Society*, **136 (S1)**, 8–33.

Lemaître, C., C. Flamant, J. Cuesta, J.-C. Raut, P. Chazette, P. Formenti, and J. Pelon, 2010: Radiative heating rates profiles associated with a springtime case of Bodélé and Sudan dust transport over West Africa. *Atmospheric Chemistry and Physics*, **10 (17)**, 8131–8150.

Liu, X.-D., S. Osher, and T. Chan, 1994: Weighted Essentially Non-oscillatory Schemes. *Journal of Computational Physics*, **115 (1)**, 200–212.

Lohmann, U., and J. Feichter, 2005: Global indirect aerosol effects: a review. *Atmos. Chem. Phys.*, **5 (3)**, 715–737.

Machado, L. A. T., and J.-P. Chaboureau, 2015: Effect of Turbulence Parameterization on Assessment of Cloud Organization. *Monthly Weather Review*, **143 (8)**, 3246–3262.

Machado, L. A. T., W. B. Rossow, R. L. Guedes, and A. W. Walker, 1998: Life Cycle Variations of Mesoscale Convective Systems over the Americas. *Monthly Weather Review*, **126 (6)**, 1630–1654.

Maddox, R. A., 1980: Mesoscale Convective Complexes. *Bulletin of the American Meteorological Society*, **61 (11)**, 1374–1387.

Mahowald, N., S. Albani, J. F. Kok, S. Engelstaeder, R. Scanza, D. S. Ward, and M. G. Flanner, 2014: The size distribution of desert dust aerosols and its impact on the Earth system. *Aeolian Research*, **15**, 53–71.

Marsham, J. H., N. S. Dixon, L. Garcia-Carreras, G. M. S. Lister, D. J. Parker, P. Knippertz, and C. E. Birch, 2013: The role of moist convection in the West African monsoon system: Insights from continental-scale convection-permitting simulations: CONVECTION IN THE WEST AFRICAN MONSOON. *Geophysical Research Letters*, **40 (9)**, 1843–1849.

Marsham, J. H., D. J. Parker, C. M. Grams, C. M. Taylor, and J. M. Haywood, 2008: Uplift of Saharan dust south of the intertropical discontinuity. *Journal of Geophysical Research: Atmospheres*, **113 (D21)**, D21 102.

Marticorena, B., and G. Bergametti, 1995: Modeling the atmospheric dust cycle: 1. Design of a soil-derived dust emission scheme. *Journal of Geophysical Research*, **100 (D8)**, 16 415.

Masson, V., J.-L. Champeaux, F. Chauvin, C. Meriguet, and R. Lacaze, 2003: A Global Database of Land Surface Parameters at 1-km Resolution in Meteorological and Climate Models. *Journal of Climate*, **16 (9)**, 1261–1282.

Masson, V., and Coauthors, 2013: The SURFEXv7.2 land and ocean surface platform for coupled or offline simulation of earth surface variables and fluxes. *Geosci. Model Dev.*, **6**, 929–960.

Mathon, V., H. Laurent, and T. Lebel, 2002: Mesoscale Convective System Rainfall in the Sahel. *Journal of Applied Meteorology*, **41 (11)**, 1081–1092.

Mekonnen, A., and W. B. Rossow, 2011: The Interaction Between Deep Convection and Easterly Waves over Tropical North Africa: A Weather State Perspective. *Journal of Climate*, **24 (16)**, 4276–4294.

Mekonnen, A., C. D. Thorncroft, and A. R. Aiyyer, 2006: Analysis of Convection and Its Association with African Easterly Waves. *Journal of Climate*, **19 (20)**, 5405–5421.

Mlawer, E. J., S. J. Taubman, P. D. Brown, M. J. Iacono, and S. A. Clough, 1997: Radiative transfer for inhomogeneous atmospheres: RRTM, a validated correlated-k model for the longwave. *Journal of Geophysical Research: Atmospheres*, **102 (D14)**, 16 663–16 682.

Nguyen, H., C. D. Thorncroft, and C. Zhang, 2011: Guinean coastal rainfall of the West African Monsoon. *Quarterly Journal of the Royal Meteorological Society*, **137 (660)**, 1828–1840.

Noilhan, J., and S. Planton, 1989: A Simple Parameterization of Land Surface Processes for Meteorological Models. *Monthly Weather Review*, **117 (3)**, 536–549.

Pantillon, F., P. Knippertz, J. H. Marsham, and C. E. Birch, 2015: A Parameterization of Convective Dust Storms for Models with Mass-Flux Convection Schemes. *Journal of the Atmospheric Sciences*, **72 (6)**, 2545–2561.

Parker, D. J., 2002: The response of CAPE and CIN to tropospheric thermal variations. *Quarterly Journal of the Royal Meteorological Society*, **128 (579)**, 119–130.

Pergaud, J., V. Masson, S. Malardel, and F. Couvreux, 2009: A parameterization of dry thermals and shallow cumuli for mesoscale numerical weather prediction. *Bound. Layer. Meteor.*, **132**, 83–106.

Petzold, A., and Coauthors, 2009: Saharan dust absorption and refractive index from aircraft-based observations during SAMUM 2006. *Tellus B*, **61 (1)**, 118–130.

Pinty, J.-P., and P. Jabouille, 1998: A mixed-phase cloud parameterization for use in a mesoscale non-hydrostatic model: simulations of a squall line and of orographic precipitations. *Conf. on cloud physics, Everett, WA, Amer. Meteor. Soc.*, 217–220.

Pytharoulis, I., and C. Thorncroft, 1999: The Low-Level Structure of African Easterly Waves in 1995. *Monthly Weather Review*, **127 (10)**, 2266–2280.

Redelsperger, J.-L., C. D. Thorncroft, A. Diedhiou, T. Lebel, D. J. Parker, and J. Polcher, 2006: African Monsoon Multidisciplinary Analysis: An International Research Project and Field Campaign. *Bulletin of the American Meteorological Society*, **87 (12)**, 1739–1746.

Reed, R. J., D. C. Norquist, and E. E. Recker, 1977: The Structure and Properties of African Wave Disturbances as Observed During Phase III of GATE. *Monthly Weather Review*, **105 (3)**, 317–333.

Rosenfeld, D., Y. Rudich, and R. Lahav, 2001: Desert dust suppressing precipitation: A possible desertification feedback loop. 5975–5980 pp.

Sassen, K., P. J. DeMott, J. M. Prospero, and M. R. Poellot, 2003: Saharan dust storms and indirect aerosol effects on clouds: CRYSTAL-FACE results. *Geophysical Research Letters*, **30 (12)**, 1633.

Sato, T., H. Miura, M. Satoh, Y. N. Takayabu, and Y. Wang, 2009: Diurnal Cycle of Precipitation in the Tropics Simulated in a Global Cloud-Resolving Model. *Journal of Climate*, **22 (18)**, 4809–4826.

Saunders, R., M. Matricardi, P. Brunel, S. English, P. Bauer, U. O'Keeffe, P. Francis, and P. Rayer, 2005: RTTOV-8 Science and validation report. Tech. rep., NWP SAF Rep., 41 pp.

Schepanski, K., I. Tegen, and A. Macke, 2009: Saharan dust transport and deposition towards the tropical northern Atlantic. *Atmos. Chem. Phys.*, **9 (4)**, 1173–1189.

Schepanski, K., I. Tegen, and A. Macke, 2012: Comparison of satellite based observations of Saharan dust source areas. *Remote Sensing of Environment*, **123**, 90–97.

Segele, Z. T., and P. J. Lamb, 2005: Characterization and variability of Kiremt rainy season over Ethiopia. *Meteorology and Atmospheric Physics*, **89 (1-4)**, 153–180.

Shao, Y., 2008: *Physics and Modelling Wind Erosion*, Vol. 23.

Solmon, F., M. Mallet, N. Elguindi, F. Giorgi, A. Zakey, and A. Konaré, 2008: Dust aerosol impact on regional precipitation over western Africa, mechanisms and sensitivity to absorption properties. *Geophysical Research Letters*, **35 (24)**, L24 705.

Stanelle, T., B. Vogel, H. Vogel, D. Bäumer, and C. Kottmeier, 2010: Feedback between dust particles and atmospheric processes over West Africa during dust episodes in March 2006 and June 2007. *Atmos. Chem. Phys.*, **10 (22)**, 10 771–10 788.

Sultan, B., and S. Janicot, 2000: Abrupt shift of the ITCZ over West Africa and intra-seasonal variability. *Geophysical Research Letters*, **27 (20)**, 3353–3356.

Sultan, B., and S. Janicot, 2003: The West African Monsoon Dynamics. Part II: The “Preonset” and “Onset” of the Summer Monsoon. *Journal of Climate*, **16 (21)**, 3407–3427.

Sutton, L. J., 1925: Haboobs. *Quarterly Journal of the Royal Meteorological Society*, **51 (213)**, 25–30.

Söhne, N., J.-P. Chaboureau, and F. Guichard, 2008: Verification of cloud cover forecast with satellite observation over West Africa. *Mon. Wea. Rev.*, **136**, 4421–4434.

Todd, M. C., R. Washington, J. V. Martins, O. Dubovik, G. Lizcano, S. M’Bainayel, and S. Engelstaedter, 2007: Mineral dust emission from the Bodélé Depression, northern Chad, during BoDEx 2005. *Journal of Geophysical Research: Atmospheres*, **112 (D6)**, D06 207.

Tompkins, A. M., 2001: Organization of Tropical Convection in Low Vertical Wind Shears: The Role of Cold Pools. *Journal of the Atmospheric Sciences*, **58 (13)**, 1650–1672.

Tompkins, A. M., C. Cardinali, J.-J. Morcrette, and M. Rodwell, 2005: Influence of aerosol climatology on forecasts of the African Easterly Jet. *Geophysical Research Letters*, **32 (10)**.

Tulet, P., V. Crassier, F. Cousin, K. Suhre, and R. Rosset, 2005: ORILAM, a three-moment lognormal aerosol scheme for mesoscale atmospheric model: Online coupling into the Meso-NH-C model and validation on the Escompte campaign. *Journal of Geophysical Research: Atmospheres*, **110 (D18)**, D18 201.

Tulet, P., M. Mallet, V. Pont, J. Pelon, and A. Boone, 2008: The 7–13 March 2006 dust storm over West Africa: Generation, transport, and vertical stratification. *Journal of Geophysical Research: Atmospheres*, **113 (D23)**, D00C08.

Vié, B., J.-P. Pinty, S. Berthet, and M. Leriche, 2016: LIMA (v1.0): A quasi two-moment microphysical scheme driven by a multimodal population of cloud condensation and ice freezing nuclei. *Geosci. Model Dev.*, **9 (2)**, 567–586.

Wang, P. K., 2003: Moisture plumes above thunderstorm anvils and their contributions to cross-tropopause transport of water vapor in midlatitudes. *Journal of Geophysical Research: Atmospheres*, **108 (D6)**, 4194.

Washington, R., M. C. Todd, S. Engelstaedter, S. Mbainayel, and F. Mitchell, 2006: Dust and the low-level circulation over the Bodélé Depression, Chad: Observations from BoDEx 2005. *Journal of Geophysical Research: Atmospheres*, **111 (D3)**, D03 201.

Winker, D. M., M. A. Vaughan, A. Omar, Y. Hu, K. A. Powell, Z. Liu, W. H. Hunt, and S. A. Young, 2009: Overview of the CALIPSO Mission and CALIOP Data Processing Algorithms. *Journal of Atmospheric and Oceanic Technology*, **26 (11)**, 2310–2323.

WMO, 2014: Guide to meteorological instruments and methods of observation. part I. Measurement of meteorological variables. Tech. rep., WMO- No. 8.

Yoshioka, M., N. M. Mahowald, A. J. Conley, W. D. Collins, D. W. Fillmore, C. S. Zender, and D. B. Coleman, 2007: Impact of Desert Dust Radiative Forcing on Sahel Precipitation: Relative Importance of Dust Compared to Sea Surface Temperature Variations, Vegetation Changes, and Greenhouse Gas Warming. *Journal of Climate*, **20 (8)**, 1445–1467.

Zender, C. S., H. Bian, and D. Newman, 2003: Mineral Dust Entrainment and Deposition (DEAD) model: Description and 1990s dust climatology. *Journal of Geophysical Research: Atmospheres*, **108 (D14)**, 4416.

Zhang, G., K. H. Cook, and E. K. Vizy, 2016: The Diurnal Cycle of Warm Season Rainfall over West Africa. Part I: Observational Analysis. *Journal of Climate*, **29 (23)**, 8423–8437.

Zhao, C., X. Liu, L. Ruby Leung, and S. Hagos, 2011: Radiative impact of mineral dust on monsoon precipitation variability over West Africa. *Atmos. Chem. Phys.*, **11 (5)**, 1879–1893.

Zipser, E. J., 1977: Mesoscale and Convective–Scale Downdrafts as Distinct Components of Squall-Line Structure. *Monthly Weather Review*, **105 (12)**, 1568–1589.